CFD Investigation of Aerodynamic Drag Reduction for a Fully Loaded Timber Truck

Master Thesis in collaboration with the ETTaero2 project

Álvaro Fernández del Río

LINKÖPINGS UNIVERSITET

Linköpings universitet
Institutionen för ekonomisk och industriell utveckling
Examensarbete 2018|LIU-IEI-TEK-A-18/03233-SE

Linköpings universitet
Institutionen för ekonomisk och industriell utveckling
Ämnesområdet Mekanisk värmeteori och strömningslära
Examensarbete 2018|LIU-IEI-TEK-A-18/03233-SE

CFD Investigation of Aerodynamic Drag Reduction for a Fully Loaded Timber Truck

Master Thesis in collaboration with the ETTaero2 project

Álvaro Fernández del Río

Academic supervisor: Petter Ekman

Examiner: Matts Karlsson

Linköping universitet
SE-581 83 Linköping, Sverige
013-28 10 00, www.liu.se

Abstract

Current rise of fuel price, together with more restrictive environmental regulation made the efficiency of trucks an interesting matter for the goods transportation industry, including the timber transportation studied on this report. One aspect that could enhance the efficiency of the vehicles is their aerodynamics.

New concepts have been studied on this report to improve the aerodynamic performance of a timber truck on its fully loaded configuration. Moreover, the shape of a loaded timber truck is not necessarily constant among different trips, hence a drag sensitivity study on different loading configurations was carried out.

First, a study on a simplified model of a tractor-trailer combination, the Allan body, was done to ensure that the CFD methodology used was appropriate. This analysis concluded that a hexahedral mesh with $y^+ \approx 30$ and the Realizable $k - \varepsilon$ with Enhanced Wall Treatment turbulence model was a good approach for the needed simulations.

On the baseline fully loaded timber truck, a simplified model of the stacks in which the flow through the logs was removed was studied. This showed a great influence on drag values, up to a 14% difference, and therefore the more realistic model was used for the rest of the studies. Starting from a flow field analysis which revealed that the cab, the gap region and the wheels were the major contributors to the total drag of the vehicle.

Several aerodynamic concepts were tested on the trailer geometry, obtaining the best results when modifying the flow on the gap with a gap spoiler, 31.6% drag reduction, which also affected the flow on the leeward side of the cabin, a very sensitive region throughout the whole study. Finally, some of the best performing concepts were combined together achieving a total drag reduction of 47.6% in the best combination.

Regarding the method development part of the thesis, a study on the simulation speed consisting of using the URANS model, with big enough time steps sizes, to converge to a steady state solution was carried out. This approach with different settings was tested in three models, showing a big influence by the geometry of the model and the quality of the mesh. From the results it could be concluded that using high values of under relaxation factors and Courant number on the Pressure Based Couple solver can speed up the convergence to the steady state solution when using a correct size of the time step, for the cases tested a value of 2.5 times the characteristic time of the problem worked well. However, larger oscillation on the solution were found when decreasing the time step to values closer to the characteristic time.

Acknowledgements

I would first like to thank Professor Matts Karlsson and PhD Student Petter Ekman for the opportunity to do this MSc Thesis work, and for their continuous help and suggestions during these months.

Acknowledgment goes also to the Division of Applied Thermodynamics and Fluid Mechanics and the National Supercomputer Center at Linköping University for all the resources used during this work.

Finally, but most important; a huge thanks to Raffaele and Xabier for all the good moments despite the hard work, would not have been the same to do this alone.

Linköping, June 2018

Álvaro Fernández del Río.

Nomenclature

Abbreviations and Acronyms

Abbreviation	Meaning
AR	Aspect Ratio
BOI	Body of influence
CAD	Computer Aided Design
CFD	Computational fluid dynamics
ETTaero2	En Trave Till, aerodynamik, projekt 2
EUR	Explicit under relaxation factor
EWT	Enhanced Wall Treatment
FMG	Full Multigrid
GGNB	Green-Gauss Node Based
GTS	Ground Transportation System
LiU	Linköping University
PBC	Pressure Based Coupled
RANS	Reynolds Averaged Navier-Stokes
RKE	Realizable $k - \varepsilon$
SST	Shear-Stress Transport
URANS	Unsteady Reynolds Averaged Navier-Stokes
UR	Implicit under relaxation factor

Latin Symbols

Symbol	Description	Units
a	speed of sound	$[m/s]$
b	Height of model	$[m]$
C_D	Drag coefficient	$[-]$
C_f	Friction coefficient	$[-]$
C_L	Lift coefficient	$[-]$
D	Drag force	$[N]$
g	Gap distance	$[m]$
k	Turbulent kinetic energy	$\left[m^2/s^2\right]$
L	Lift force	$[N]$
l	length of model	$[m]$
M	Mach number	$[-]$
p	Pressure	$[Pa]$
q	Dynamic pressure	$[Pa]$
Re	Reynolds number	$[-]$
S	Area	$\left[m^2\right]$
t	Time	$[s]$
u, v , w	Velocity components	$[m/s]$

Symbol	Description	Units
u_τ	Friction velocity	$[m/s]$
u^+	Dimensionless velocity	$[-]$
y^+	Dimensionless wall distant	$[-]$

Greek Symbols

Symbol	Description	Units
α_t	Time scale factor	$[-]$
ε	Rate of viscous dissipation	$\left[m^2/s^3\right]$
μ	Dynamics viscosity	$\left[kgm^{-1}s^{-1}\right]$
μ_t	Turbulent or eddy viscosity	$\left[kgm^{-1}s^{-1}\right]$
ν	Kinematic viscosity	$\left[m^2s^{-1}\right]$
ρ	Density	$\left[kg/m^3\right]$
τ	Shear stress	$[Pa]$
ω	Specific dissipation rate	$\left[s^{-1}\right]$

Subscripts and superscripts

Abbreviation	Meaning
∞	Freestream conditions
c	Characteristic value
crit	Critical conditions
ref	Reference value

Contents

1 Introduction

1.1 Background

Transportation by trucks is the most important mean of transport of goods in the European Union, and the number of trucks has been continuously increasing in the last years [1]. This situation, together with the rise of fuel price and the more restrictive environmental policies, has increased the interest on improving the efficiency of these type of vehicles.

Aerodynamics of the truck is one of the most important aspects to consider in order to improve the efficiency, since a 35% of the total resistance is generated by the aerodynamic drag at normal operation speeds of 80 km/h [2]. However, the different manufactures involved in the full vehicle, for cabs and trailers, and the higher interest of reducing the engine emissions have caused a lack of attention to the full vehicle aerodynamics improvement.

A special case of goods transport, in which this work will focus, is the transport of timber. The operating conditions of timber trucks constrain the possible design modifications that can be implemented to increase their aerodynamic efficiency. Two main characteristics distinguish these vehicles from other transport trucks; the fact that they travel empty half of the time, not just in weight but also in volume, and that the load is not always box-shaped as in a normal trailer truck, the different stacks configurations reshape the exterior of the vehicle influencing on its aerodynamic performance; moreover, flow through the stacks is possible in this case and could also influence the performance. This force, in some extent, all the possible geometry modifications to work both with the unloaded and loaded truck and to not disturb the loading process.

For a loaded timber truck between a 20 to 30% of the fuel consumption comes from aerodynamic drag [3] and, from previous studies on trucks aerodynamics [4], it is considered that a percentage reduction in drag can reduce the fuel consumption by half of that percentage.

In Sweden there are around 2000 operational timber trucks for a total transportation of 6 Billion ton-km with an average fuel consumption of 0.025 liters of Diesel per ton-km, between 30 and 50% higher than normal trailer trucks configurations [5]. One of the approaches to reduce the global consumption of timber trucks is creating a larger truck, up to 74 ton instead of the 60 ton truck currently used. If designed properly, this modification can lead to a higher increase in loading capacity than in fuel consumption per truck, therefore the needed number of timber trucks could be reduced and the total fuel consumption of timber transportation decreased.

The particular fuel consumption of a timber truck can be reduced with the implementation of geometrical modification both in the cabin and the trailer, however it has to be taken into account that these modification must work for the complete journey

of a timber truck, that is loaded and unloaded configuration. Previous wind tunnel studies and road tests results presented in [3] comparing different aerodynamic add-ons (deflectors, gap-seals and skirts) and loading configurations (short-wood, saw logs and tree-length stacks) for timber trucks showed possible drag reductions and fuel savings. The results showed that the short-wood stacks have the largest potential for percentage reduction in drag, up to a 19% when using deflector, gap-seal and skirts together; however, the baseline drag coefficient is significantly higher with respect to the tree-length and saw logs stacks. A reduction of 17 and 10% was found for the saw logs and the tree-length, respectively, when using deflectors and skirts together. The gap-seal did not show any improvement in cross-wind conditions in this study for the tree-length configuration, but it was effective for the short-wood stacks, which is more sensitive to yaw angles variations. The deflector showed the best overall performance for all the stacks configurations. However, it has to be noted that this device is only effective for a loaded truck and not for the unloaded part of the trip, whereas the trailer skirts reduce the drag on both states without affecting the loading process.

More recent wind tunnel studies, including the larger 74 ton 1-3-2-3 axle configuration, presented in [6] compare different aerodynamic improvements for both the unloaded and loaded trucks. The study of the unloaded truck, on a 60 ton model, reveled the importance of the stakes shape since the wind average drag coefficient increases with respect to the baseline fully loaded truck when the stakes are placed in their normal position. Removing the stakes or folding them on the base on the trailer result in a decrease of wind averaged drag, 28% and 21% respectively with respect to the baseline case. Two more aerodynamically shaped stakes were tested yielding a significant decrease on drag for the unloaded truck, approximately a 7%, and also a smaller influence of the yaw angle. Regarding the loaded truck, two aerodynamic kits were tested on a 74 ton model with the objective of removing the gap between the cab and the trailer. Filling this gap completely could decrease the drag to levels of the less capacity 60 ton truck, but the installation of this device is more difficult due to the operating conditions and the traffic legislation. However, a modification of the cab and the addition of a boat tail also result in drag reduction with respect to the baseline model, up to a 12% in wind averaged drag. These results together indicate that modifications of the stakes for the unloaded truck and in the gap for the loaded truck could result in an overall decrease of drag in the trip, however modifications have to be studied together for optimization and to not disturb the loading process of the timber truck.

1.2 Aim

This thesis work involves two main tasks and objectives; a methodology development consisting on an approach to improve the CFD simulation speed, and the study of different aerodynamics concepts to enhance the performance of the loaded timber truck, that is, reducing its aerodynamic drag and therefore its fuel consumption.

A simplified geometric model of a tractor-trailer configuration, the Allan Body [7], is used as a first step for testing of different meshing approaches and turbulence

models.

Regarding the methodology development, different approaches are used to increase the simulation speed; that includes increasing the under-relaxation factors in some stages in order to obtain a faster convergence to a steady-state solution, and solver methods used currently in other industries, such as Formula 1. The Allan Body is again used as a testing model, since the simulations require less computational power than the needed for the larger meshes used for the full scale timber truck, to confirm that the adjustments in the solver lead to the desired result when compared with the existing experimental data in [7]. These settings are then to be applied to the timber truck model and the impact on the solution is assessed by comparison with the results obtained with the original solver setup.

The aerodynamic development for the loaded truck is carried out in several steps, starting from a study of the baseline model to find where the aerodynamic performance can be improved. Several aerodynamic concepts and their possible installation are then studied in the timber truck model. Collaboration with the concept generation process for the unloaded timber truck is needed during this phase of the work since it is best if the devices work in both configurations, and the aerodynamic performance should be optimized for the complete trip due to the truck driving in each condition half of the time. These concepts are studied for different yaw angle to obtain the wind average drag coefficient and have a more realistic view of the operating conditions. Moreover, the loaded truck does not necessarily travel fully loaded, in terms of volume, all the time and the position of the load can vary, hence this is also considered for the implementation of the devices.

2 Theory

This section introduces a brief description of aerodynamics and its influence on heavy trucks performance. The main governing equations of fluid dynamics are explained and their implementation for being solved using CFD described.

2.1 Fundamentals of Aerodynamics

2.1.1 Forces and coefficients

Aerodynamics is the field of fluid dynamics dedicated to the study of the motion of air and the forces and resulting movements created on objects on it. The primary objective of aerodynamics is to study these resulting loads and momentums acting on a body; these loads are created by pressure forces acting in the normal direction of the surface, and friction forces acting as tangential stresses on the surface. The integration of these forces over the total surface of the body give the resultant force and momentum load; the force is usually divided in components with respect to the direction of the freestream velocity, named lift (L) in the perpendicular direction of that velocity and drag (D) in the same direction of it.

For a meaningful comparison between different cases, the forces are expressed as non-dimensional coefficients based on the dynamic pressure of the freestream flow of each case and the reference area (S_{ref}) of each model, (2.1), (2.2), where ρ is the density, u the velocity and the subscript ∞ indicates freestream conditions.

$$C_L = \frac{L}{\frac{1}{2}\,\rho_\infty u_\infty^2 S_{ref}} \tag{2.1}$$

$$C_D = \frac{D}{\frac{1}{2}\,\rho_\infty u_\infty^2 S_{ref}} \tag{2.2}$$

2.1.2 Similarity

One of the most important aspects to consider on aerodynamics studies is the dynamic similarity conditions of the analysis, that is, to be able to compare the values of the coefficients obtained from different experiments, for example wind tunnel scaled tests, full-scale experimental values or computational simulations results; some conditions have to be fulfilled together by the geometry of the model and the flow conditions. Firstly, geometry similarity is achieved by having linearly scaled geometries in all the experiments. Regarding the flow conditions similarity, it is defined using mainly two non-dimmensional values, Reynolds and Mach number.

The Reynolds number is of great importance in all the fields of fluid dynamics and it is defined as the ratio between the inertial forces and the viscous forces (2.3), indicating if the viscous effects are important for the problem or if the case can be considered inviscid (high values of Re), neglecting the effects of viscosity. For viscous problems, the value of the Reynolds number may indicate if it is laminar ($Re<Re_{crit}$) or turbulent and where the regime transition occurs.

$$Re = \frac{inertial forces}{viscous forces} \tag{2.3}$$

From a dimensional analysis of the momentum equation [8], the Reynolds number can be expressed in terms of flow variables as shown in (2.4), where L is the characteristic length of the geometric model and μ is the molecular viscosity of the fluid.

$$Re = \frac{\rho\ u\ L}{\mu} \tag{2.4}$$

The other flow similarity parameter is the Mach number (2.5), defined as the ratio of the freesream velocity to the speed of sound at the same freestream conditions, a_∞. High values of Mach number indicate that compressibility effects are present in the flow, meaning that changes in velocity will cause changes in the density. Flows with Mach below 0.3 may be considered as incompressible.

$$M_\infty = \frac{u_\infty}{a_\infty} \tag{2.5}$$

Hence, two studies can be considered dynamically similar when the geometries are linearly scaled, and both flows have the same Reynolds and Mach number; in cases of incompresible flows as the one of this thesis it must be checked that the velocity needed for scaled test does not make the flow enter the compressible regime. Inflow conditions, such as turbulence level introduced on the flow, must also be taken into account for a meaningful comparison of results.

2.1.3 Near wall region.

Forces acting on the surfaces of the body, pressure and viscous, are the main responsible of the resulting loads; hence a good understanding of the near wall region is needed to properly calculate these forces. This divides the flow in two different zones; a thin region adjacent to the surface, called boundary layer, where the viscosity effects have a great influence on the flow behavior, and the bulk flow far enough form the surface to be considered essentially inviscid.

The flow in the boundary layer is characterized by a large value of the velocity gradient in the perpendicular direction, starting form the zero value at the surface and increasing to a value close to the freestream velocity, Fig. 2.1, the point where the velocity reaches 99% of the value of the freestream is considered the end of the boundary and its distance to the wall is the boundary layer thickness at that location.

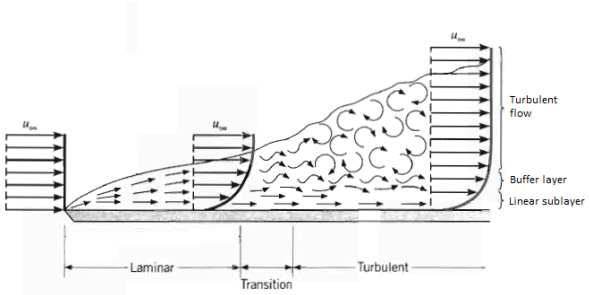

Figure 2.1: Example of a boundary layer development on a flat plate, modified from the original on [9].

This large velocity gradient makes the shear stresses, τ as in (2.6), important in the boundary layer and therefore the viscosity effects are considered; whereas the small changes of velocity outside the boundary layer allows to neglect the viscosity effects on the bulk flow, since the shear stresses would be really small in this case.

$$\tau = \mu \left(\frac{\partial u}{\partial y} \right) \tag{2.6}$$

The boundary layer starts to develop on a stagnation point of the surface and its thickness increases along the surfaces, Fig. 2.1; the boundary layer is laminar at the beginning, unless turbulent conditions are introduced in the inflow; but can become turbulent, or separate from the laminar state, depending on several flow characteristics; such as pressure gradient, surface roughness, curvature and temperature, compressibility effects, suction or blowing on the surface or the level of turbulence in the freestream flow.

Comparing the two types of boundary layer it can be said that the laminar boundary layer is thinner and has lower mass transfer than the turbulent, the velocity gradients near the wall and the skin friction have larger values when the boundary layer has changed to turbulent. These differences are caused by the form the local exchange of momentum is done in the perpendicular direction to the surface; in laminar boundary layers this occurs at a microscopic scaled, meaning that the changes only affect the adjacent layers of the fluid. On the other hand, in turbulent boundary layer the macroscopic exchange of momentum makes the particles move farther inside the boundary layer creating larger velocity gradients and shear stresses on the wall, equation (2.6).

The starting laminar boundary layer confront disturbances as it develops over the surface, depending on the strength of those disturbances the flow can damp them and remain laminar, or they can increase making the flow turbulent. The location of the transition point is directly influence by the local Reynolds number; however, the transition does not occur immediately after surpassing the critical value of the Reynolds number, it is a process starting with unstable flow that will promote the creation of eddies leading to a final fully turbulent flow, Fig. 2.1.

The turbulent boundary layer is also divided in different sublayers, important for the near wall region modeling approach explained on Sec. 2.3. For the study of this

region, variables based on the local perpendicular distance to the wall are defined, equations (2.7) and (2.8) where u_τ is the friction velocity and ν is the kinematic viscosity of the fluid.

$$y^+ = \frac{u_\tau y}{\nu} \tag{2.7}$$

$$u^+ = \frac{u}{u_\tau} \tag{2.8}$$

The flow on direct contact with the surface is stagnated, therefore the motions of the turbulent eddies very close to the wall must also be stopped; this region is called linear sublayer since $u^+ = y^+$ and occupies a really thin region in contact with the wall, $y^+<5$, where no turbulence is found (laminar flow), and the flow is dominated by viscous effects. Following this region, for values of $5<y^+<30$, the magnitude of viscous and turbulent stresses are of the same order in what is called the buffer layer. The last part of the inner layer is called log-law layer, due to the logarithmic relationship between u^+ and y^+, in this region turbulent stresses are dominant and its extension reaches values up to $y^+ = 500$.

The outer region cover from 80 to 90% [8] of the total boundary layer thickness, in this region viscous effects are negligible since it is far enough from the wall and the flow is dominated by inertial forces.

An important aspect of the boundary layer related with the aerodynamic performance study of a body is its possible separation in different areas of the surface, since it generally increases the pressure drag [10]. Separation can be induced by abrupt changes of the geometry or by characteristics of the flow, mainly the pressure gradient. An adverse pressure gradient, $dp/dx>0$, near the wall makes the boundary layer unstable due to the decrease of velocity, this can lead to reverse flow, if the gradient is too large for the flow to overcome it; causing the boundary layer separation. The macroscopic scale momentum exchange on a turbulent boundary layer increases the streamwise momentum, delaying the separation with respect to a laminar boundary layer since the flow can overcome the adverse pressure gradient for a longer distance.

2.2 Truck Aerodynamics

Aerodynamic performance is an important aspect for trucks used on good transportation, especially the aerodynamic drag force since it is directly related with the fuel consumption of the vehicle. According to [11], in highway conditions the major contributors to fuel burnt are the aerodynamics losses and rolling resistance with more than a 30% of the total each. Hence, reducing the aerodynamics losses can significantly reduce the total fuel consumed by heavy transport vehicles such as timber trucks.

From the two main aerodynamic forces explained in Sec. 2.1.1, the influence of lift on heavy vehicles can be neglected due to their large weight and relatively low

velocity. An important aspect to consider for aerodynamic forces on heavy vehicles is the wind conditions, as explained on [2] the total drag coefficient of these vehicles would significantly increase for higher yaw angles, angle between the wind and the vehicle, due to the increasing tangential force. Hence, a more significant value for drag comparison should include the influence of lateral wind, there are several formulations to obtain different wind-average drag coefficients as shown in [12].

In order to improve the aerodynamic performance it is important to identify which regions of the vehicle contribute more to the total drag value. A loaded timber truck could be considered similar to a long combination vehicle form by a rigid truck, a dolly and a semi-trailer, with two main loads separated by a gap, Fig. 2.2. The larger values of drag on these type of vehicle comes from the cab, the gap between the two loads and the wheels and underbody, according to [11].

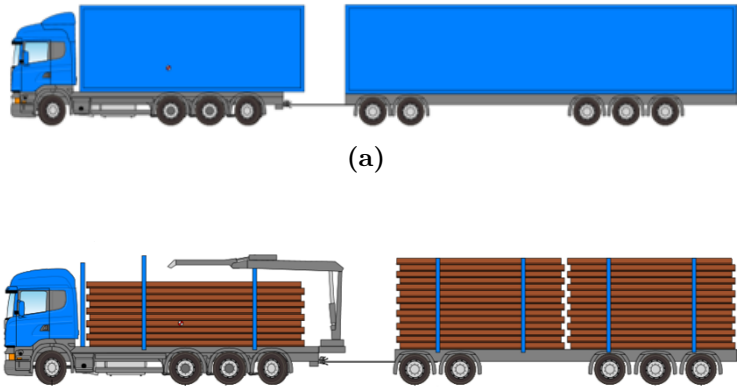

(a)

(b)

Figure 2.2: Rigid truck, dolly and semi-trailer configuration (a). Fully loaded timber truck (b).

Common solutions implemented for drag reduction on these vehicles include modifications on the deflector angle, devices to change the features of the flow inside the gap, devices to reduce the base pressure on the back face of the trailer or underbody flow management by the implementation of solutions such as skirts.

2.3 Governing equations

Three main equations are needed to solve the physics of fluids in motion: Continuity, momentum and energy equations.

Different simplifications can be applied to these equations according to the flow characteristics of the problem. Such as flows where no significant changes of temperature are expected, where the energy equation does not need to be solved, that is the case for all the cases studied on this thesis.

The continuity equation, on vector form in 2.9, represents the requirement of mass conservation, meaning that the flow field is physically possible.

$$\frac{\partial \rho}{\partial t} + \frac{\partial \left(\rho u_i\right)}{\partial x_i} = 0 \tag{2.9}$$

Where, ρ is the density, t the time, u_i the velocity components, and x_i the coordinates.

The conservation of linear momentum is expressed by the momentum equation 2.10, consisting on Newton's Second law applied to a fluid particle, that is, the net force acting on that particle is equal to the time rate of change of its linear momentum. The forces of interest acting on a particle are body forces, directly on the particle, and pressure and viscous forces acting on its surface.

$$\rho \frac{Du_i}{Dt} = -\frac{\partial \rho}{\partial x_i} + \rho f_i + \frac{\partial}{\partial x_j} + \left(2\mu S_{ij} - \frac{2}{3}\mu \frac{\partial v_k}{\partial x_k}\delta_{ij}\right) \tag{2.10}$$

Where, ρ is the density, t the time, u_i the velocity components, x_i the coordinates, f_i the body force per unit of mass in each direction, μ the dynamic viscosity, and S_{ij} the strain-rate tensor.

2.4 Turbulence

Almost all problems of engineering interest are turbulent in some regions, that is, Reynolds number above Re_{crit} on those locations. The flow in this condition is characterized by, [13]: Irregularity, diffusivity, large Reynolds numbers, three-dimensional features, dissipation and model as a continuum.

A turbulent flow contains eddies of different scales; the larger scales extract kinetic energy from the flow that then is passed to the smaller scales trough a cascade process; at the smallest scales near the wall, for which friction forces are more important than turbulent, the energy is dissipated as thermal energy.

These characteristics make the flow unsteady and the variables have a random behavior with the appearance of fluctuations with respect to time. The value of a property (φ) at every time can be expressed using the Reynolds decomposition (2.11), as the sum of a steady mean $\bar{\varphi}$ value and a time dependent fluctuation with zero mean value $\varphi'(t)$.

$$\varphi(t) = \bar{\varphi} + \varphi'(t) \tag{2.11}$$

2.4.1 Reynolds Average Navier-Stokes Equations

Using the Reynolds decomposition (2.11) on all the variables involved in the continuity and momentum equations for incompressible flows, which is the case for all flows in this work since it is low speed aerodynamics (M<0.3), the RANS (Reynolds Average Navier-Stokes) equations are obtained, continuity 2.12 and momentum 2.13; these are the base for the steady state turbulence models.

$$\frac{\partial \bar{v}_i}{\partial x_i} = 0 \tag{2.12}$$

$$\rho \frac{\partial \bar{v}_i \bar{v}_j}{\partial x_j} = -\frac{\partial \bar{p}}{\partial x_i} + \rho f_i + \frac{\partial}{\partial x_j}\left(\mu \frac{\partial \bar{v}_i}{\partial x_j} - \rho \overline{v_i' v_j'}\right) \tag{2.13}$$

Where, $\bar{v}_i$ represents the components of the steady mean value of velocity,$\bar{v}_i'$ the components of the velocity fluctuations, $\bar{p}$ the steady mean value of pressure, ρ the density, μ the dynamic viscosity.

A new term appears in the momentum equation (2.13) due to the velocity fluctuations generated by the turbulence, this term $\left(\rho \overline{v_i' v_j'}\right)$, called Reynolds stress tensor, is unknown and represents the correlations between the fluctuating velocities. Now the number of equations is smaller than the total number of unknowns, hence a model for the Reynolds stress tensor is needed to close the problem.

2.4.2 Turbulence modeling

The components of the Reynolds stress tensor of equation (2.13) need to be modeled in order to use the RANS equations to solve a turbulent flow. Additional transport equations are added to the set of RANS equations (2.12) and (2.13) to close the problem and obtain a solution for the flow field. The more common RANS turbulence model are classified according to the number of new equations added to the original RANS equations; such as zero (Mixing length model), one (Spalart-Allmaras), two ($k-\varepsilon$, $k-\omega$) or seven (Reynolds stress model).

$k-\varepsilon$ model is one of the most commonly used turbulence models, and the one chosen for this thesis; it is based on the Boussinesq assumption from which the Reynolds stresses are related to the viscous stresses (velocity gradients). Hence, a new variable called turbulent or eddy viscosity (μ_t) is introduced, and the Reynolds stress tensor on the RANS equation (2.13) is replaced by the product of the turbulent viscosity by the velocity gradients.

$$-\rho \overline{v_i' v_j'} = \mu_t \left(\frac{\partial \bar{u}_i}{\partial x_j} + \frac{\partial \bar{u}_j}{\partial x_i}\right) - \frac{2}{3}\rho k \delta_{ij} \tag{2.14}$$

Eddy viscosity models are used to mathematically model the turbulent or eddy viscosity introduced on equation (2.14); the $k-\varepsilon$ model, developed by Launder and Spalding in [14] , in particular adds two transport equations to the RANS equations to solve the turbulent kinetic energy (k) and the rate of viscous dissipation (ε); and the turbulent viscosity is modeled as shown in equation (2.15).

$$\mu_t = \rho C_\mu \frac{k^2}{\varepsilon} \tag{2.15}$$

There are several modifications to the original standard $k-\varepsilon$ model that improve its performance in different situations, for this thesis work the Realizable $k-\varepsilon$ is

chosen; in this model the turbulent viscosity is model with the same equation (2.15) as in the standard. However, the coefficient C_μ does not have a constant value in the Realizable model and it is calculated with expression (2.16), where A_0 and A_s are constants and U^* is calculated as introduced by [15].

$$C_\mu = \frac{1}{A_0 + A_s \frac{kU^*}{\varepsilon}} \tag{2.16}$$

The modified transport equations for k (2.17) and ε (2.18)in the Realizable $k-\varepsilon$ model are:

$$\frac{\partial}{\partial t}(\rho k) + \frac{\partial}{\partial x_j}(\rho k u_j) = \frac{\partial}{\partial x_j}\left[\left(\mu + \frac{\mu_t}{\sigma_k}\right)\frac{\partial k}{\partial x_j}\right] + G_k + G_b - \rho\varepsilon - Y_M + S_k \tag{2.17}$$

$$\begin{aligned}\frac{\partial}{\partial t}(\rho \varepsilon) + \frac{\partial}{\partial x_j}(\rho \varepsilon u_j) = \frac{\partial}{\partial x_j}\left[\left(\mu + \frac{\mu_t}{\sigma_\varepsilon}\right)\frac{\partial \varepsilon}{\partial x_j}\right] + \rho C_1 S\varepsilon - \\ - \rho C_2 \frac{\varepsilon^2}{k + \sqrt{\nu\varepsilon}} + C_{1\varepsilon}\frac{\varepsilon}{k} C_{3\varepsilon} G_b + S_\varepsilon\end{aligned} \tag{2.18}$$

Where G_k and G_b represent the generation of turbulence kinetic energy due to the mean velocity gradients and due to buoyancy, respectively; Y_M is the contribution to the overall dissipation rate of the fluctuating dilatation in compressible turbulence; and S_k and S_ε are user-defined source terms. For the constant, the default values on ANSYS Fluent [16] were used, that is, $C_{1\varepsilon} = 1.44$, $C_2 = 1.9$, $\sigma_k = 1.0$, $\sigma_\varepsilon = 1.2$.

These modifications improve the performance of the Realizable over the Standard $k-\varepsilon$ when solving flows with strong streamline curvature, vortices and rotation; and it also captures better the possible separation of the flow and the secondary flow features, [16].

Another commonly used turbulence model used for aerodynamics studies is the Shear-Stress Transport (SST) $k-\omega$; which is based on the standard $k-\omega$ model, but differs in the treatment on the outer layer of the boundary layer where a version of the $k-\varepsilon$ model is used, and in the formulation of the turbulent viscosity where the SST takes into account the transport effects of the principal turbulent shear stress, adding a limiter of the shear stress in regions of adverse pressure gradients;[16], [13].

The SST $k-\omega$ is a two-equations model, that is, transport equations for turbulent kinetic energy , k, (2.19) and specific dissipation rate , ω, (2.20) are added to the RANS equations. The specific dissipation rate is defined as the ratio of the rate of viscous dissipation to the turbulent kinetic energy, $\omega = \varepsilon/k$.

$$\frac{\partial}{\partial t}(\rho k) + \frac{\partial}{\partial x_i}(\rho k u_i) = \frac{\partial}{\partial x_j}\left(\Gamma_k \frac{\partial k}{\partial x_j}\right) + G_k - Y_k + S_k \tag{2.19}$$

$$\frac{\partial}{\partial t}(\rho \omega) + \frac{\partial}{\partial x_i}(\rho \omega u_i) = \frac{\partial}{\partial x_j}\left(\Gamma_\omega \frac{\partial \omega}{\partial x_j}\right) + G_\omega - Y_\omega + D_\omega + S_\omega \tag{2.20}$$

Where Γ_k and Γ_ω are the effective diffusivities of k and ω. G_k represents the generation of turbulence kinetic energy due to the mean velocity gradients; G_ω the generation of specific dissipation rate; Y_k and Y_ω the disipation due to turbulence of k and ω, respectively; D_ω the cross-diffusion term; and S_k and S_ω are user-defined source terms. The default values of ANSYS Fluent Theory Guide [16] were used for the constants included in the variables described above; that is, $\sigma_{k,1} = 1.176$, $\sigma_{\omega,1} = 2.0$, $\sigma_{k,2} = 1.0$, $\sigma_{\omega,2} = 1.168$, $a_1 = 0.31$, $\beta_{i,1} = 0.075$, and $\beta_{i,2} = 0.0828$.

Main advantage of the standard $k-\omega$ over the $k-\varepsilon$ model is its better performance on flow regions with adverse pressure gradients and a better prediction of boundary layer separation. However, this model is strongly sensitive to the freestream values of k and ω when solving the flow outside the shear layer.

The aim of the SST model is to remove this sensitivity of the standard formulation by using a blending of the $\omega-$ and $\varepsilon-$equation; in this way a better performance on the near-wall region is achieved with the $k-\omega$ model, while maintaining freestream independence results of the $k-\varepsilon$.

As explained on Sec. 2.1.3, the solution of flow adjacent to the wall is of great importance for the accuracy of the global solution, since the flow field on the bulk flow would be calculated using the value at the end of the boundary layer as a reference. There are two different ways on which the turbulence models can resolve this region depending on the mesh resolution.

If the resolution of the mesh is fine enough, $y^+<1$, the boundary layer can be resolved all the way down to the wall. On the other hand, the region adjacent to the wall where the viscosity effects are important can be left unresolved and, instead, use empirical formulations called wall-function to model the flow between the wall and the fully turbulent flow on the freestream. This case is computationally cheaper since the resolution of the mesh near the wall does not need to be as fine. Since there is no intention of resolving the viscous flow in the linear and buffer sublayers, a value of $y^+>30$ is generally adequate for the use of wall functions. Values of $y^+ \approx 15$, that is the first would be placed inside the buffer layer, may lead to numerical errors in the traditional wall functions. y^+ independent formulations have been added to several turbulence models in ANSYS Fluent [16], such as the Enhanced Wall Treatment used together with the Realizable $k-\varepsilon$ model on this thesis work. This near wall treatment uses a two-layer approach to solve the near wall region, meaning that the viscous sublayer would be resolved if the mesh resolution is fine enough all the way down to the wall; otherwise a wall function would be used, making the model work with a decent level of accuracy independently of the mesh resolution. This approach can lead to numerical problems if the first node is placed in the intermediate region between the near wall modeling and the region acceptable to use the empirical formulation of the wall functions; this is also solved by the blending functions used on the Enhanced Wall Treatment approach.

For resolving the viscous sublayer in the near wall region, the resolution of the mesh needs to have great refinement all over the region, not just a small enough value of y^+. That is, the total thickness of the boundary layer needs to be cover by enough number of prism layers, minimum 10 [16].

2.5 Improved simulation speed

This section explains the theory applied on the methodology study with the objective of increasing the simulation speed by the use of pseudo-transient solver to obtain a steady state converged solution.

2.5.1 Unsteady RANS model

The URANS model is used on the transient approach. This model consist of the same RANS equations shown on Sec. 2.4.1 but keeping the original transient term (partial derivation over time),continuity equation (2.21) and momentum equation (2.22); moreover, the flow field variables are now also a function of time, not only of the spatial coordinates.

$$\frac{\partial \bar{v}_i}{\partial x_i} = 0 \tag{2.21}$$

$$\frac{\partial \bar{v}_i}{\partial t} + \rho \frac{\partial \bar{v}_i \bar{v}_j}{\partial x_j} = -\frac{\partial \bar{p}}{\partial x_i} + \rho f_i + \frac{\partial}{\partial x_j}\left(\mu \frac{\partial \bar{v}_i}{\partial x_j} - \rho \overline{v_i' v_j'}\right) \tag{2.22}$$

The Reynolds decomposition applied on the variables of the URANS equations results on three different terms for each variable (2.23): a time-average part ,$\langle\bar{\varphi}\rangle$, a resolved fluctuation, φ', and a modeled turbulent fluctuation, φ'', [13].

$$\varphi(t) = \bar{\varphi} + \varphi''(t) = \langle\bar{\varphi}\rangle + \varphi'(t) + \varphi''(t) \tag{2.23}$$

To resolve part of the turbulence with a time average set of equations the time step use for the Reynolds decomposition of the URANS equations must be much smaller than the time scale of the turbulence structures to be resolved. However, this is not the case on this study since the URANS method is just used as a way to faster advance the solution towards a converged steady state solution. Hence, the time step used is larger than the characteristic time of the problem.

2.5.2 Temporal discretization

To perform a transient simulation the URANS equations must be discretized on time, a first-order implicit scheme (2.24) from [16] is normally accurate enough for most of the problems [17], and unconditionally stable with respect to the size of the time step used.

$$F(\varphi) = \frac{\varphi^{n+1} - \varphi^n}{\Delta t} \tag{2.24}$$

F is a function of the variable φ that includes the spatial discretization used, Δt is the time step size, n indicates the value of the variable (φ) at the current time

step and $n+1$ the value at the next time step, $t+\Delta t$, this value is obtained from equation (2.24) by solving the flow field equations iteratively inside every time step.

2.5.3 Pressure-Based Coupled Solver

ANSYS Fluent 18 offers two possible methods to obtain the flow field solution, Pressure-Based Solver or Density-Based Solver. The Pressure-Based Solver is used on this study of low speed incompressible flow. On this approach the velocity field is obtained from the momentum equations and the pressure from a pressure correction equation created from the continuity and momentum equations, in a form to guarantee that the continuity requirement is fulfilled.

Continuity and momentum equations are coupled to each other and the Pressure-Based Solver has two possibilities to solve them: segregated or coupled algorithms. For the desired increase on simulation speed the coupled algorithm is recommended [17], since solving a coupled set of the equations with the momentum and continuity improves the rate of convergence, although the memory required also increases.

Solver settings

Different solver settings are available when using the Pressure-Based Coupled Solver to control the advancement of the solutions from iteration to iteration, these parameters are related with the under-relaxation of the solution, both explicit and implicit.

The explicit under-relaxation, or under-relaxation of variables, is applied on pressure and momentum in the coupled solver; this parameter controls the change of the variable per iteration in the inner loop of the coupled solver by updating its value according to the user defined under-relaxation factor, [16]:

$$\varphi_{new} = \varphi_{old} + \alpha_{exp}\,\Delta\varphi \tag{2.25}$$

Where α_{exp} is the explicit under-relaxation factor and $\Delta\varphi$ is the change of the variable value in the current iteration. Hence, a higher explicit under-relaxation factors updates the solution faster, but might make the solution unstable; whereas a smaller factor keeps more influence form the previous iteration facilitating the convergence.

The implicit under-relaxation, or under-relaxation of equations, is set by the Courant flow number (acting on the flow equations of pressure and momentum) and the implicit under-relaxation factors for the turbulence model equations, for this case k and ε equations; and controls the convergence of the outer iterations of the coupled solver.

$$\frac{a_p\varphi_{new}}{\alpha_{imp}} = \sum_{nb} a_{nb}\varphi_{nb} + b + \frac{1-\alpha_{imp}}{\alpha_{imp}} a_p\varphi_{old} \tag{2.26}$$

The relation between Courant flow number (CFL) and the equivalent implicit under-realaxation of the flow equations is:

$$\alpha_{imp} = \frac{CFL}{1 + CFL} \tag{2.27}$$

This can be understood as a transient advancement of the solution where CFL defines the local time step size in each cell as multiples of the cell Courant number; since the implicit temporal discretization is used the formulation is unconditionally stable with respect to the time step size and the CFL number of the solver can be used to increase the speed of the convergence. As for the explicit under-rellaxation, larger values of implicit under-realaxation factors or solver CFL introduce less information from the previous solution in the current iteration.

3 Method

This section presents the overall approach followed during the thesis work and describes the methodology used to obtain the different results. The methodology used for the Allan Body study is explained first, as it is an introduction for the more detailed analysis on the timber truck and also used in some phases of the simulation speed methodology development. The geometry of the models, the computational domain and mesh used, and the numerical setup for each case are explained in this section.

3.1 Allan Body

3.1.1 Geometry and computational domain

The Allan Body is a simplified truck geometry consisting on two boxes in tandem, Fig.3.1, representing a tractor-trailer combination, used in [7] for wind tunnel testing and drag and pressure measurements. In [7], both boxes have sharp edges in the baseline geometry and the influence of rounded edges on the front boxes is studied. For this thesis, the rounded edges of the front box were chosen as part of the geometry, since it is a more realistic simplification of a truck model, and the analysis was focused on the gap distance between the two boxes. Another simplification assumed for the study in this project was the symmetry of both the model and the flow field, since cross wind conditions are beyond the scope of this part of the thesis. Hence, the geometry used for the Allan body study was half of the original one used in [7] with radius edges on the front face of the front box.

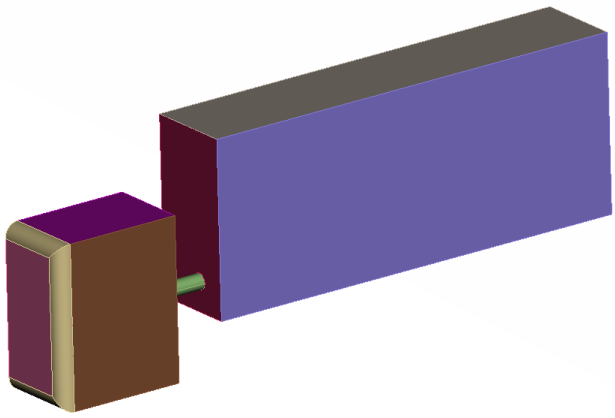

Figure 3.1: Allan Body geometry for gap distance $g/b = 0.17$.

Since the later study on turbulence models aimed for a gap distance influence on the drag results, four different geometries were created with distances between boxes (g), compared with the height of the model (b), of $g/b = 0.17$, $g/b = 0.25$, $g/b = 0.50$

and $g/b = 0.67$; chosen for easier comparison with the experimental results shown on [7] and the simulations carried out in [18] and to get a enough values to see the trend in the whole range of gap distances.

The domain used, Fig.3.2,for the computational simulation, equivalent to the one in [7] and [1], had a length of $9.4\,l$ a width of l and a height of $1.6\,l$; where the model was placed at $2.4\,l$ from the inlet, to obtain a uniform flow field upstream of the model, and a distance of $6\,l$ was left until the outlet to properly capture the wake and not affect the results on the model with the boundary condition set on the outlet, where l is the length of the model.

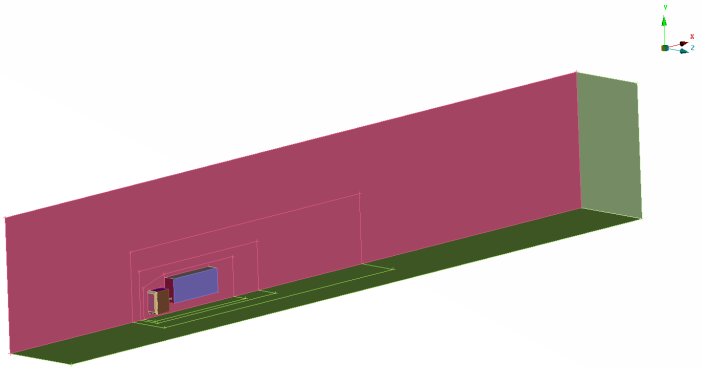

Figure 3.2: Compautational domain used for the simulations on the Allan body.

3.1.2 Numerical setup

The numerical setup used for the simulations on ANSYS Fluent 18 consisted on steady state simulations performed with two different turbulence models for comparison, SST $k-\omega$ and Realizable $k-\varepsilon$ with Enhanced Wall Treatment. The Reynolds number of the problem was 0.51e6 based on the height of the model $b = 0.305$ m, as in [7], with a freestream velocity of 24.4 m/s (Mach number of 0.07).

For this low speed incompressible case the Pressure-Based solver was used with the coupled scheme for the pressure and velocity relation, and Least Square Cell-Based for the gradients evaluations. The discretization schemes used for the different equations are, as recommended for this type of studies in [19]:

Table 3.1: Discretization schemes used on the Allan Body simulations.

Equation	Scheme
Pressure	Standard
Momentum	Second Order Upwind
Turbulence kinetic energy (k)	First Order Upwind
Turbulence dissipation rate(ε)	First Order Upwind

The simulations were intended to model wind tunnel conditions to reproduce the study on [7] and compare the CFD simulations results with the experimental values

obtained in the real wind tunnel [7], therefore the boundary conditions applied on the domain were set as indicated on Table 3.2.

Table 3.2: Boundary conditions used on the Allan Body simulations.

Boundary zone	Condition
Inlet	Velocity-inlet
Outlet	Pressure-outlet
Top wall	Stationary, no slip wall
Side wall	Stationary, no slip wall
Symmetry plane	Symmetry
Ground	Moving, no slip wall
Model surfaces	Stationary, no slip wall

The velocity in the inlet was set to 24.4 m/s, in order to obtain the same Reynolds number as in the wind tunnel measurements of [7] in standard atmospheric conditions with $\rho = 1.225\ kg/m^3$ and $\mu = 1.789 \cdot 10^{-5}\ kg/ms$ and using the height of the model, 0.305 m, as the characteristic lenght of the problem. The level of turbulence in the inlet was set according to [19], with turbulence intensity of 0.1% and turbulent viscosity ratio of 50.

The outlet condition was set to zero static pressure flow.

The top and side walls were model with no slip condition in order to model the boundary layer that would appear on a wind tunnel experiment.

The ground was modeled as a moving wall, with the same velocity set in the inlet to simulate the same boundary layer of road conditions. Also model as no slip wall to properly capture the characteristics of the flow especially under the model.

The solution was initialized using the Full Multigrid (FMG) feature of ANSYS Fluent, [16]; this method creates different grid levels from the original one and, starting from a uniform flow field with zero velocity obtained with a standard initialization, user defined method to initialize the solution to the desired values of the flow field variables; the FMG lower the residuals on each level starting form the coarsest one. In this initialization process the Euler equations for inviscid flow are solved using a first order discretization. This does not require a lot of computational cost and gives a better initial solution that can make the convergence of the final solution faster.

During the solution process, monitors of the forces in the three directions were saved on each iteration for later check the convergence of the solution, mainly the drag coefficient, together with the residuals values of the flow equations. The solution was considered as converged if the residuals dropped below 10e-4 and the variation of the drag coefficient monitor was less than 2% per iteration, as recommended in [19].

3.1.3 Computational mesh

The computational mesh for the Allan Body study was created in two steps, surface mesh was done with ANSA and volume mesh was generated using ANSYS Fluent Meshing; for the volume mesh three different approaches were tested (tetrahedral, hexahedral and polyhedral) for comparison of results accuracy and computational cost. Refinement regions on the surface and bodies of influence on the volume were used for a more effective mesh result.

The surface of the Allan Body geometry was meshed with two different main size sets in order to get a more refine mesh in regions with important flow characteristics; that is a smaller element size was used on the rounded edges of the front box, on the cylinder connecting the two boxes, on the front face of the rear box and on the edges where flow separation could be expected. The bodies of influence used in the volume cut the ground and the symmetry plane, therefore to obtain a good size transition the same size of the bodies of influence was applied on the intersection edges on those surfaces and spacing between the consecutive sizes was used in the common edge of the ground and the symmetry plane. The rest of the outer surfaces of the domain were all mesh with a constant element size.

The surface mesh created in ANSA was exported to Fluent Meshing to generate a volume mesh; three refinement boxes were used around the model and meshed as bodies of influence, this was done doubling the element size of the previous one to get a refined mesh close to the model and a coarser one on the farfield. Prism layers to capture the flow characteristics on the near wall region were also generated by Fluent Meshing, 12 layers were used all around the Allan Body surfaces, except of the cylinders where no boundary layer was expected and the sharp edges in the connection to the boxes would difficult the creation of prism layers especially for the shortest gap distance. Six prism layers were used on the top and lateral wall to capture the boundary layer created since the simulation corresponds to wind tunnel conditions. Finally, although a moving ground was implemented, five prism layers were used to capture the acceleration of the flow due to the reduction of area especially below of the front box.

3.1.4 Mesh sensitivity study

A mesh sensitivity study was carried out on each of the three volume meshes types, starting from the same surface mesh size; that is, three surfaces meshes with different sizes were created in ANSA and one volume mesh of each type was created in Fluent Meshing for every surface mesh, resulting in nine final meshes for each of the gap distances tested. Different independence analysis were done for each type of volume mesh, and later the performance of the different types was assessed by comparing the mesh-independent results obtained with each type. This procedure was done for the two extreme cases of gap distance, $g/b = 0.17$ and $g/b = 0.67$; to ensure that the resulting mesh most likely worked for all the cases used for further studies.

The size on the refined regions of the surface mesh was set from 0.8 mm on the coarsest mesh to 0.52 mm on the finest; the maximum size range was from 5 mm to

3.2 mm. In the volume mesh the sizes of the bodies of influence were set to make each body have double the size of the previous one, directly set for the hexahedral mesh and kept the same in the other approaches for the later comparison. In this manner, the body of influence in contact with the surface had a size of 6.25 mm in the coarse mesh, 5 in the medium, and 4 in the fine mesh. All the volume meshes were crated with the same number of prism layers and same first node height, since the mesh sensitivity study was done using the Realizable $k-\varepsilon$ model, a value of $y+ \simeq 30$ is enough and a first node height of 1.1 mm was therefore used for all the layers around the Allan Body surface.

From the mesh independence analyses on each type, mesh-independent results were obtained for meshes of 3 million elements on the polyhedral mesh, 4.6 million on the hexahedral mesh and 7.5 million on the tetrahedral mesh, since the total drag coefficient and the drag on the gap faces did not change more than a 5% if the mesh resolution was increased. These three meshes were compared to original experimental results on the Allan Body [7] to assess their performance.

Table 3.3: Total drag coefficient for different mesh types.

g/b=0.17		
	C_D	% from [7]
Exp. [7]	0.76	-
Polyhedral (3M)	0.69	9.2
Hexahedral (4.6M)	0.73	3.9
Tetraedral (7.4M)	0.79	3.94
g/b=0.67		
	C_D	% from [7]
Exp. [7]	1.28	-
Polyhedral (3M)	1.20	6.3
Hexahedral (4.6M)	1.22	4.6
Tetraedral (7.4M)	0.83	35

From the results shown on Table 3.3, it can be noted that the hexahedral mesh performed better for both small and large gap distances, with differences smaller than a 5% with respect to the experimental data on both cases. For the other mesh types it is noticeable the bad performance of the tetrahedral mesh for the larger gap distance, for which it is clearly under-predicting the drag value much more than the other two types of meshes that give more similar results. Regarding the polyhedral mesh, the results were not far form the ones obtained with the hexahedral mesh and the total number of elements was clearly lower. However, it also has to be consider the computational cost of creating the polyhedral mesh which was much higher than the one of the hexahedral mesh, since first a tetrahedral mesh is created and then converted into polyhedral elements [20].

A more detailed comparison was carried out by doing a breakdown of the forces on the different surfaces of the Allan Body, in order to see which ones influence more the total drag of the model and where the differences between the mesh types and

the experimental data are found, the results for are shown on Fig.3.3.

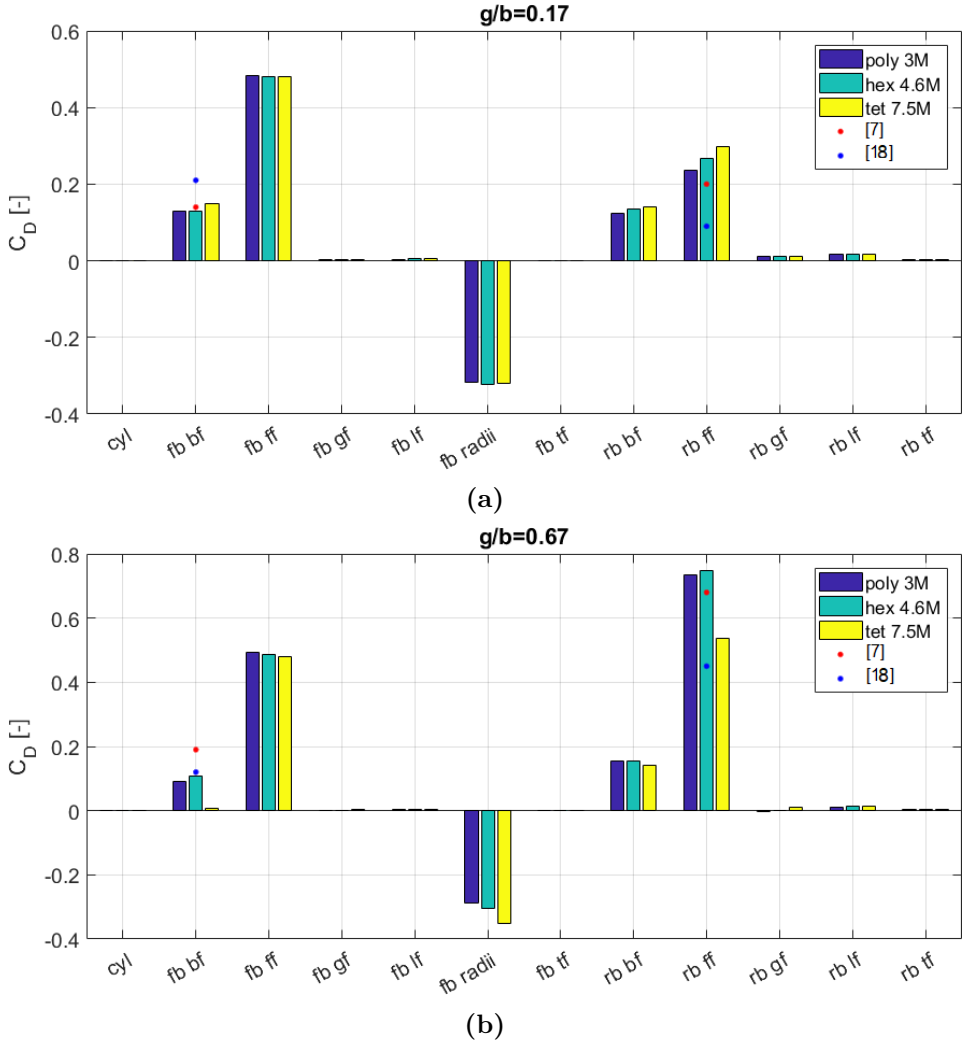

Figure 3.3: Comparison of the breakdown of the drag coefficient on the different surfaces of the Allan body; $g/b = 0.17$ **(a),** $g/b = 0.67$ **(b).**

Comparing the results from the two different gap distances it can be noted that for the larger gap, Fig.3.3(b), the faces on the gap contributed more to the total drag coefficient than for the smaller gap, Fig.3.3(a), where the front face of the cabin (fb-ff) was the mayor contribution. Whereas the more flow present between the two boxes makes the drag of the rear box (rb-ff) increase for the second case. Regarding the differences between the types of meshes, it can be seen that the disagreement were found in the faces of the gap (fb-bf and rb-ff), being the values on the other surfaces more similar, especially for the smaller gap distance. The tetrahedral mesh gave the worst performance of the three types, with especial disagreement with the experimental data on the larger gap distance, Fig.3.3(b). Probable cause for this difference is the fail of correctly capture the separation on the front box by the tetrahedral mesh and therefore a wrong flow field obtained in the gap.

Considering all these facts, it was decided that the hexahedral mesh of 4.6 million elements was the one chosen for the next studies, Fig. 3.4. This mesh consisted

on a hexahedral mesh in the bulk flow, with prism layers around the surfaces of the model (12 layers, 1 mm of first node height), the walls of the domain (6 layer, maximum aspect ratio of 8) and the ground (5 layers, maximum aspect ratio of 4), that were connected to the hexahedral mesh by peel layers of tetrahedral elements. The smallest element size used on the surface mesh was 0.64 mm on the refined regions and a maximum element size of 4 mm was used for the surface mesh. The bodies of influence used for refinement around the model were set to 5, 10 and 20 mm; then the last stage of hexahedral elements had a size of 40 mm until the peel layers on the outer surfaces of the domain.

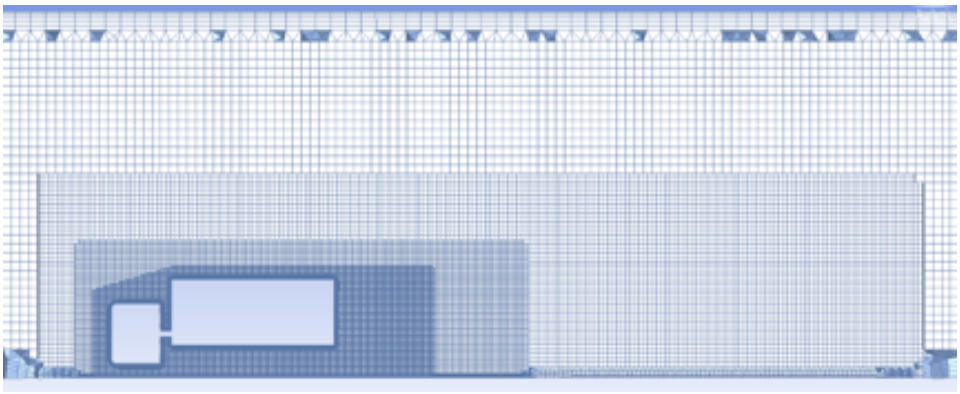

Figure 3.4: 4.6 million hexahedral mesh used on the Allan Body simulations.

3.1.5 Turbulence models comparison

A turbulence model study was carried out on the Allan Body to compare the performance between Realizable $k-\epsilon$ with Enhanced Wall Treatment and SST $k-\omega$ with two different near wall resolutions, $y^+ \simeq 30$ and $y^+ \simeq 1$. The final hexahedral mesh of 4.6 million elements chosen on the previous section was used for the $y^+ \simeq 30$ cases, and a new mesh with first node height of 0.013 mm on the prism layers on the model surfaces was created for the SST $y^+ \simeq 1$ case, without changing any other setting, leading to a total number of elements of 6 million.

The total drag coefficient for the different turbulence models and the four gap distances studied are shown on Fig.3.5, and compared with the experimental data obtained by [7] and the CFD simulations, done with RKE turbulence model, results from [1]. It can be seen that both RKE and SST with $y^+ \simeq 30$ followed the same tendency as the experimental data with increasing drag coefficient for larger gap distances, but with somehow lower values especially for the SST with $y^+ \simeq 30$ and RKE at large gap distances. On the other hand, the SST model with $y^+ \simeq 1$ did not follow that tendency, clearly underpredicting the total drag for the two cases with larger gap distances.

In order to see where those big differences came from the drag coefficient on the gap faces was obtained; from the results on Fig.3.6 it can be noted that the lower total values obtained with the SST model and $y^+ \simeq 1$ for the larger gap distances were mainly caused by an underprediction of the drag generated on the front face

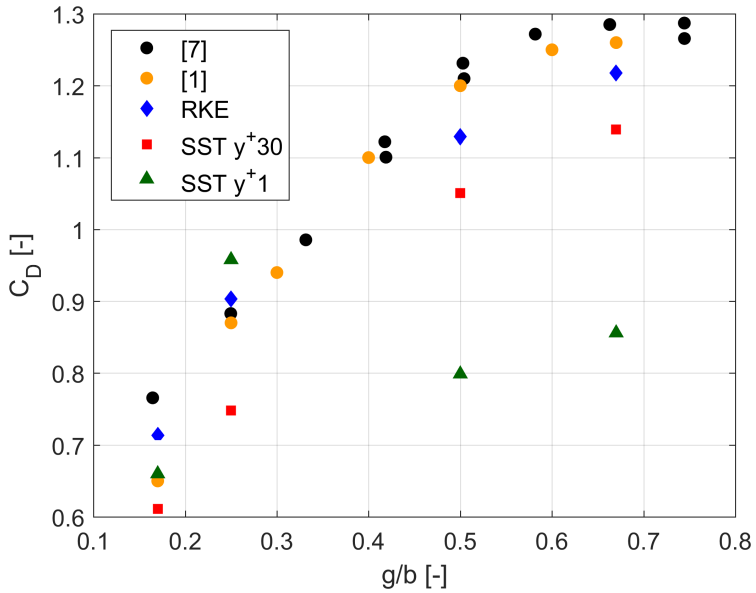

Figure 3.5: Comparison of total drag coefficient for different turbulence models.

of the rear box (rb-ff), the model also get a lower value of drag on the back face of the front box (fb-bf) which explained the clearly poorer performances of the SST $y^+ \simeq 1$ shown on Fig. 3.5 . Whereas the, smaller, underprediction of the other two models was caused by the value on the back face of the front box (fb-bf), since there is a good agreement with experimental data on [7] and CFD simulations with RKE on [1] on the front face of the rear box (rb-ff) for all the gap distances. As a general comment from Fig. 3.6, it can be noted that the increase of drag with increasing gap distance comes almost completely from the front face of the rear box. The drag on the back of the front box is almost constant for the different gap distances, indicating that the flow field leaving the front box is not really affected by the distance between the boxes; whereas the larger distance, and therefore more flow on the gap, clearly increases the drag on the rear box.

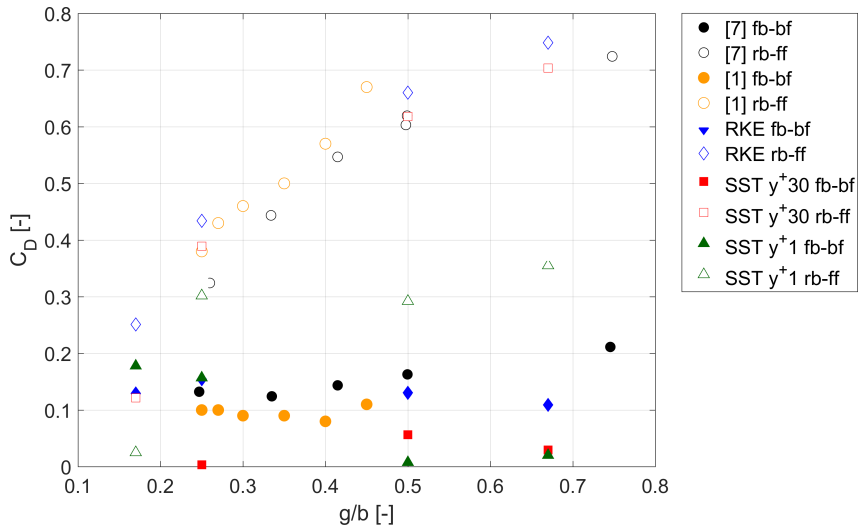

Figure 3.6: Comparison of drag coefficient on gap faces for different turbulence models.

Analyzing the flow field for one of those larger gap distances, $g/b = 0.50$, it can be seen in Fig.3.7 how in the low-drag values results obtained with the SST $y^+ \simeq 1$ the region of high static pressure on the front face of the rear box is clearly smaller than the one of the more accurate results obtained using RKE or SST $y^+ \simeq 30$ and therefore wall functions. Hence, since this is the face with more influence on the drag for the large gap distances, the SST with $y^+ \simeq 1$ was underpredicting the total value of drag coefficient for these distances as seen on Fig.3.5.

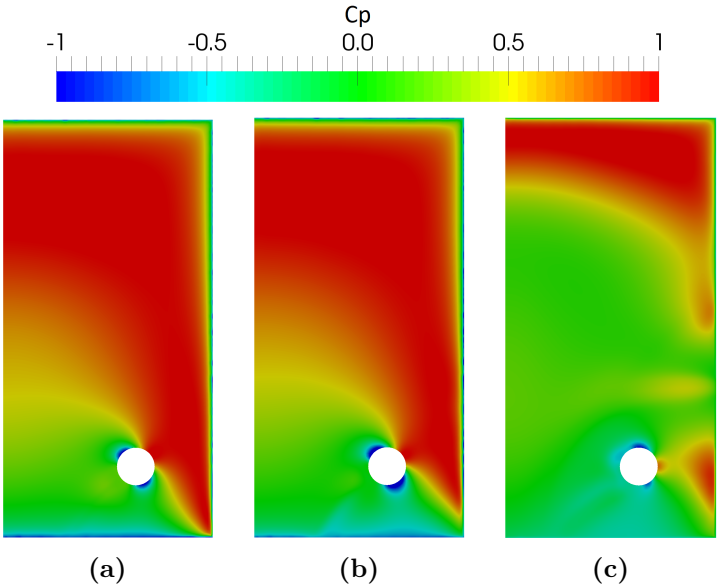

Figure 3.7: Pressure coefficient on the front face of the rear box for RKE $y^+ \simeq 30$ (a), SST $y^+ \simeq 30$ (b) and SST $y^+ \simeq 1$ (c); $g/b = 0.50$.

That difference on the front face of the rear box is generated by the different flow on the gap and, therefore, by how the flow leaves the front box. A contour of total pressure coefficient on the symmetry plane is shown on Fig.3.8 for the same turbulence model comparison. It can be noted that on Fig.3.8(a) the flow remains attached all along the top face of the front box, whereas on Fig.3.8(c) separation occurs directly downstream of the rounded edges of the front box. This big separation detected by the SST when resolving the flow all the way down to the wall with $y^+ \simeq 1$, directs the flow towards the top part of the rear box reducing the amount of flow inside the gap, that causes the low base pressure on the front face of the rear box shown on Fig.3.7. The use of wall function with the SST model, Fig.3.8(b), also showed a separation on the top of the front box; in this case the separation occurred a bit later after the rounded edges than in the RKE model; this separation is smaller when using wall function than when resolving the near wall region; that explains the more similar results obtained with RKE and SST $y^+ \simeq 30$ shown on Fig.3.5.

This differences on flow separation can also be noted using iso-surfaces of total pressure coefficient around the model, Fig.3.9. The same conclusion obtained with Fig.3.8 can be drawn with the iso-surfaces; in Fig.3.9(a) it can be seen that just a small separation occurs after the rounded edges on the top face of the front box and how the flow reached the end of that box attached to the surface to later separate on the sharp edges of the back face of the front box and the front face of the rear box.

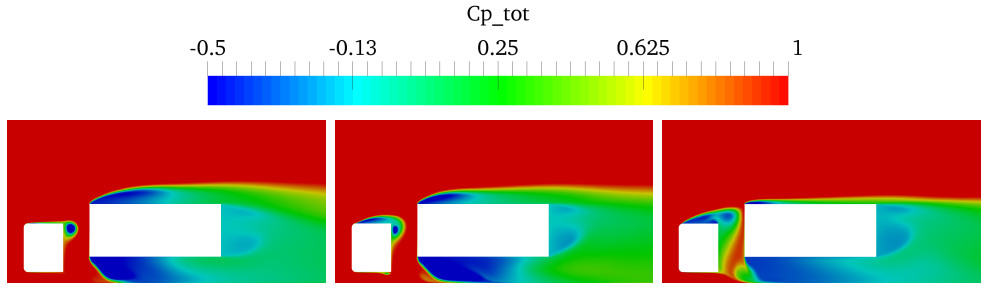

(a) **(b)** **(c)**

Figure 3.8: Total pressure coefficient on the symmetry plane: RKE $y^+ \simeq 30$ (a), SST $y^+ \simeq 30$ (b) and SST $y^+ \simeq 1$ (c); $g/b = 0.50$

On the other hand, on Fig3.9(c), a large flow separation occurred all around the front box and the flow did not reattach to the surface of this box. An intermediate situation is shown on Fig3.9(b), were most of the flow on reattached to the surface of the top face of the front box before the gap, leading to the more similar results of the two models using wall functions, RKE and SST with $y^+ \simeq 30$.

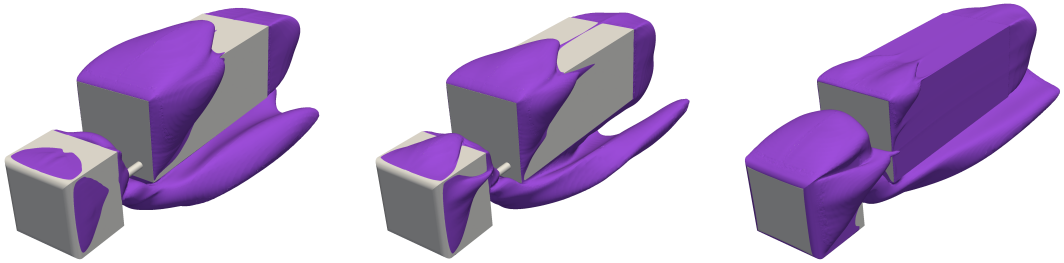

(a) **(b)** **(c)**

Figure 3.9: Iso-surfaces of zero total pressure coefficient: RKE $y^+ \simeq 30$ (a), SST $y^+ \simeq 30$ (b) and SST $y^+ \simeq 1$ (c); $g/b = 0.50$

These different predictions of the location of the flow separation for the two turbulence models comes from the amount of turbulence generated by each of them in the boundary layer. The Realizable $k - \varepsilon$ model tends to produce too much turbulence; therefore, as explained on Sec.2.1.3, the more energetic turbulent boundary layer could remain attached for a longer distance. On the other hand, the SST model produces less turbulence, promoting an earlier separation of the flow. This can also be compared with the experimental results on [7] where the separation behavior of the flow was intermediate with respect to the three cases shown on Fig. 3.9.

3.2 Loaded timber truck

This subsection explains the methodology applied for the studies on a loaded timber truck, some conclusions drawn on Sec.3.1 for the Allan Body were directly applied on the timber truck. And some studies were done for the unloaded configuration of the timber truck and later translated to the loaded one with some modifications.

3.2.1 Geometry and computational domain.

The original truck on which this thesis is based on is a 74 ton timber truck with 9 axles in a 1-3-2-3 configuration, a detailed model of this truck is shown on Fig.3.10. A simplified model of this geometry for the unloaded configuration was obtained from [5], to which different timber stacks configurations were added, Fig. 3.11.

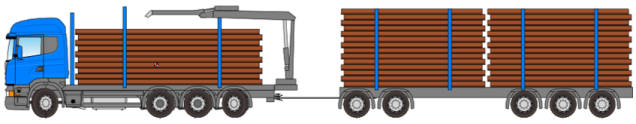

Figure 3.10: Detailed model of the 74 ton timber truck vehicle.

The stacks of logs were created in CATIA, where the contacts regions between them were simplified adding chamfers in order to eliminate the sharp edges that would later difficult the meshing work. These stacks were then imported to ANSA and merged with the simplified geometry model of the unloaded timber truck, Fig.3.11(a), after placing the stacks on the correct position on the truck some CAD cleaning was required on the contacts between the logs, stakes and bunks. The objective was to remove the sharp edges and small gaps between those parts, since that would require unnecessarily small elements to obtain a mesh with proper quality and those regions are not important for the global flow field behavior. Hence, the connections between logs and stakes and bunks were simplified by adding a new face instead of the sharp edge contact, Fig.3.11(b).

As a baseline geometry for the loaded timber truck, logs of diameters between 320 and 350 millimeters were used in stacks 5600, 6260 and 7260 millimeters long, starting from the one directly after the cabin. The total height of the stacks for this case is approximately 2520 millimeters, using the frame of the truck as a reference. The height of the bulkhead is 2840 millimeters, leaving some space available for increasing the stacks height and compare different configurations.

The importance of the flow going through the stacks of logs and its influence on the flow field around the truck and the total drag coefficient of it was studied on this baseline geometry; for this model the area of the openings was 0.5 m^2 over a total frontal area of the stacks of 4.5 m^2.

The total length of the simplified model is l =25.4 meters, and the computational

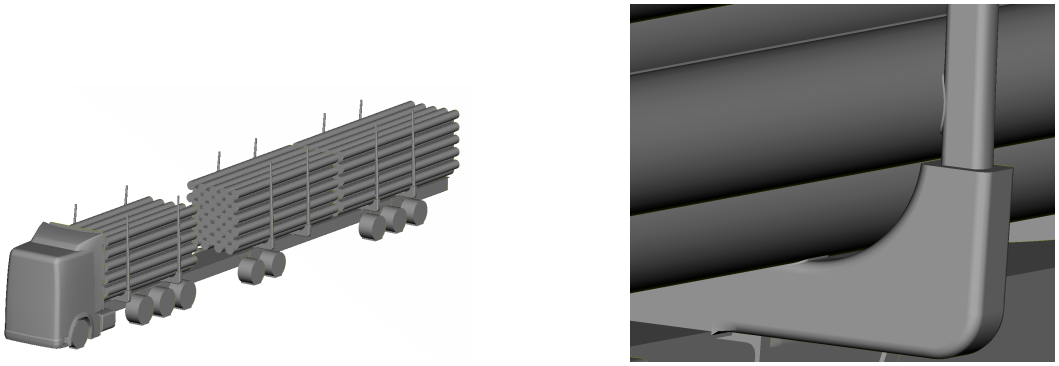

(a) (b)

Figure 3.11: Example of loaded configuration geometry (a). Detail of the connection of logs to stakes and bunks (b)

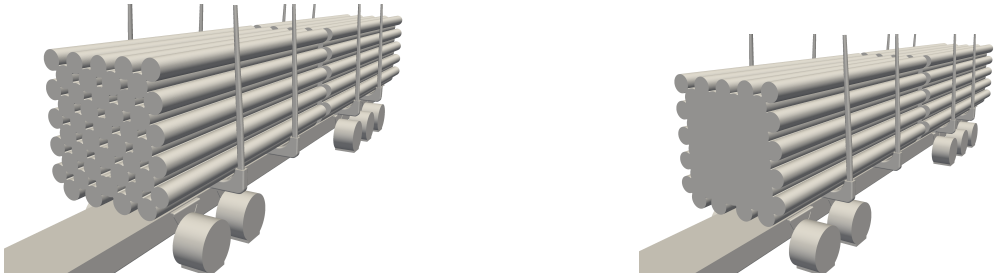

(a) (b)

Figure 3.12: Stacks of logs used on the baseline model (a), simplified model without flow going through the logs (b)

domain used for the simulations was $9.33\,l$, with the model placed at $3.5\,l$ from the inlet of the domain, and $4.83\,l$ were left behind the model to capture the wake, Fig.3.13.

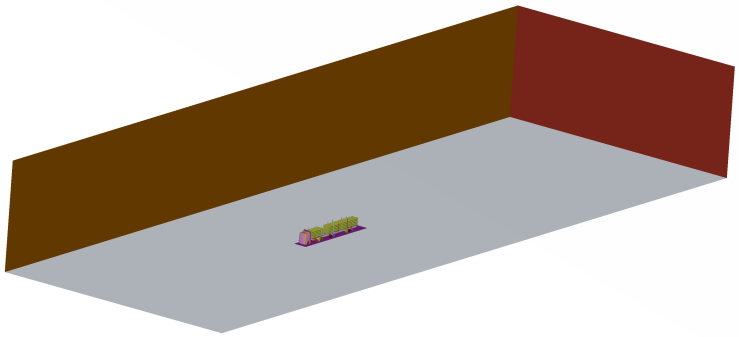

Figure 3.13: Computational domain used on the timber truck simulations.

3.2.2 Numerical setup

The numerical setup used for ANSYS Fluent 18 simulations was the same described for the Allan Body on Sec.3.1.2; for this case, after the results of the turbulence models study on the Allan Body, only the Realizable $k-\varepsilon$ turbulence with Enhanced Wall Treatment was used. The discretization schemes used for the different flow equations are shown on Table 3.1.

The simulations on the timber truck intended to model road conditions with different cross wind conditions, yaw angles, and with a Reynolds number of 4.9e6 based on the square root of the frontal area. Therefore, the boundary conditions applied on the domain, Table 3.4, were modified from the ones used on the Allan Body since the flow field is not symmetric for the cross wind simulations, and were also different between the cases with and without crosswind.

Table 3.4: Boundary conditions used on the timber truck simulations.

Boundary zone	Condition ($Yaw = 0°$)	Condition ($Yaw \neq 0°$)
Inlet	Velocity-inlet	Velocity-inlet
Outlet	Pressure-outlet	Pressure-outlet
Top wall	Symmetry	Symmetry
Left-side wall	Symmetry	Velocity-inlet
Right-side wall	Symmetry	Pressure-outlet
Ground-moving	Moving, no slip wall	Moving, no slip wall
Ground	Stationary, free slip wall	Stationary, free slip wall
Model surfaces	Stationary, no slip wall	Stationary, no slip wall

The inlet was set as velocity-inlet on both cases of Table3.4, however the velocity values were different; for no cross wind conditions the velocity is set with only and x-component of the same value as the truck travel velocity ($22.222\ m/s = 80\ km/h$); for the different cross wind conditions, the x-component of the velocity was kept with the truck velocity value and a velocity on the z-direction was added with the corresponding value for every yaw angle simulated (2.5, 5, 7.5, 10 and 15 degrees). The turbulence level on the inlet was set according to the standards of the industry [19], with a turbulent intensity of 0.1% and a turbulent viscosity ratio of 50.

The outlet was set to pressure-outlet with zero static pressure, for all the cases.

To simulate the cross wind correctly in the whole domain, the boundary conditions on the lateral walls also needed to be modified. For straight wind conditions, they were modeled as symmetry since they were far enough from the truck to get an undisturbed flow. The cross wind was assumed to enter from the left side of the truck, therefore the left-side wall was changed to velocity-inlet with the same values as the inlet for every condition, whereas the right-side wall was modified to pressure outlet with zero static pressure.

The top wall of the domain was placed far enough from the model, so the flow in that region was undisturbed by the truck and it could be modeled as symmetry.

In order to get a realistic boundary layer reaching the model, the ground was divided

on two different regions, Fig. 3.13: a stationary free slip wall was used far from the model, and a moving no slip wall was set on the proximity of the truck. The velocity of this moving ground was set on the x-direction and equal to the travel velocity of the truck ($22.222\ m/s = 80\ km/h$), also for the cross wind simulations since the intention was to keep the truck traveling always at the same speed.

The surfaces of the model, except for the wheels, were set as stationary no slip walls to model the boundary layer. The wheels instead were modeled as moving no slip walls, where the velocity was set using the rotational speed of the wheels, 44.004 rad/s and 50.505 rad/s for the wheels on the truck and the trailer respectively, based on the different radius of the tires.

The solver was initialized using the Full Multigrid method on [16], and the solution advanced on several steps changing the Pressure-Based Couple solver settings, for a total of 3270 iterations. During the solution process, monitors of force coefficient on the three directions were saved to check the convergence of the solution, this was assessed by looking if the residuals dropped below 10e-4 and the oscillation of the drag coefficient monitor was less than 2% per iteration. Finally, the drag coefficient value was averaged over the last 900 iterations to obtain the final result for each simulation.

3.2.3 Computational Mesh, unloaded timber truck.

This thesis was done in collaboration with two other students involved in the ET-Taero2 project, working on different truck models; hence, for simplification, the computational mesh sensitivity study was done together in only one truck model (unloaded), and later adapted to the particular case of this report, fully-loaded timber truck.

The generation of the mesh was done following the same procedure explained for the Allan Body, that is, the surface mesh was created in ANSA and imported into ANSYS Fluent Meshing where the volume mesh was created. Triangular elements were used on the surface and hexahedral mesh for the volume, including prism layers for the near-wall modeling, and tetrahedral elements in the peel layers for the transition to the bulkflow.

For the surface mesh generation of the unloaded timber truck, the model was divided in three different sets in ANSA according to their importance for the flow field solution; the most refined set included the radius edges of the cabin and the stakes, the medium one the rest of the surfaces in the cabin, and the coarsest set all the other surface of the body, such as the chassis and the wheels.

Those same sets were also used for the generation of the prism layers on Fluent meshing; more layers and less first-node-height was used in on the refined set were the flow was expected to be attached. Prism layers were also implemented on the ground to properly capture the acceleration of the underbody flow, in this case a maximun aspect ratio of 8 was specified instead of defining the height of the first node. Table 3.5 shows the setup of prism layers used for the unloaded timber truck, this setup was kept constant during the mesh sensitivity study, where only the

surface mesh and volume were modified.

Table 3.5: Prism layers used on the unloaded timber truck.

Region	Number of layers	First-node-height [mm]
Set 1	16	0.75
Set 2	16	1
Set 3	10	1.2
Set 4-Ground	6	- (1^{st}layer AR=8)

Different levels of refinement were used in the volume mesh by the implementation of bodies of influence; the octree hexahedral mesh approach used on the volume mesh makes every level of the mesh be double the size of the previous one. Hence, the element size in the volume was defined by specifying the size of the most refined body of influence closed to the truck, and the geometry of the bodies of influence where the element size changes to the nest level. Out of the last body of influence, the element size grows in the number of levels required until the surface mesh size defined for the outer boundaries of the domain.

For the unloaded timber truck five bodies of influence were used, with four levels of elements size since two bodies were used with the most refined size in different locations of the geometry; one from the cabin, the first and second pair of stakes and the chassis, and one for the rest of the stakes on the back of the truck. Then, the rest of the bodies of influence grow to the bulk flow oriented in the direction of the yaw angles to properly capture the wake in crosswinds conditions studies.

Mesh sensitivy study, unloaded timber truck.

A mesh sensitivity study was carried out on an unloaded timber truck for the 10 degrees yaw angle condition, since it was considered a limiting case to asses the good performance of the mesh for the whole sweep of yaw angles.

Three different mesh sizes were used for the study, starting from a different surface mesh and creating three final volume meshes of 50, 87 and 122 million elements, distributed in an equivalent form on the domain. The variables studied for the mesh sensitivity performance were drag coefficient, total and buildup along the truck on the x-direction, and velocity profiles at different locations.

The results on total drag coefficient did not yield big differences between the three meshes, smaller than 2% on all the cases. Hence, the study was focused more on the velocity profiles, Fig. 3.14, since the drag is an integrated value that can give a similar final result due to mismatches at different locations.

From the velocity profiles shown on Fig. 3.14 it can be noted that, specially in the underbody flow influenced by the wheels, there are large differences between the coarsest (50 million elements) mesh and the other two meshes. However, the improvement in terms of performance by increasing the number of elements from 87 to 122 millions is not significant meaning that the results are mesh-independent, therefore, a mesh of 87 million elements was considered enough to resolve this flow field, final size values for this mesh are shown on Table 3.6 and 3.7.

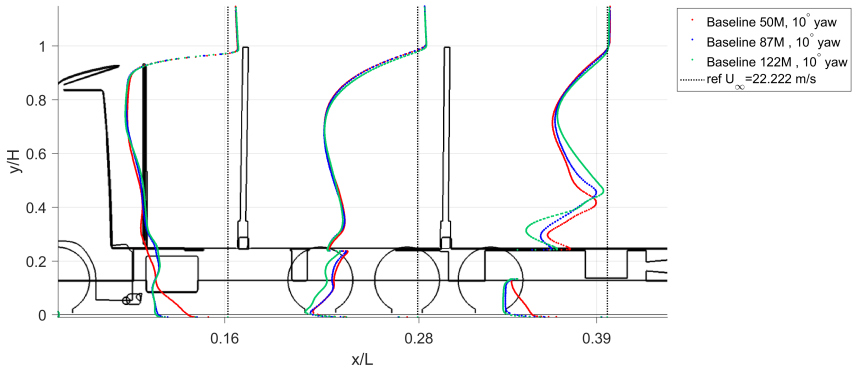

Figure 3.14: Velocity profiles on the symmetry plane at different x/L positions.

Table 3.6: Surface mesh sizes used on the unloaded timber truck.

Region	Min. size [mm]	Max. size [mm]
Set 1	6.2	13.8
Set 2	7.7	18.5
Set 3	9.2	18.5

Table 3.7: Volume mesh sizes used on the unloaded timber truck.

Region	Element size [mm]
BOI 1	198.4
BOI 2	99.2
BOI 3	49.6
BOI 4	24.8
BOI 5	24.8
Outer Domain	1800

3.2.4 Computational Mesh, fully-loaded timber truck.

The differences on geometry between the unloaded and fully-loaded timber truck forced some modifications in the mesh. Hence, starting from the setup of the 87 million elements, these modifications were applied to the sizes and distribution of elements in a way that the resulting mesh could be assumed to give independent results also for the fully-loaded timber truck.

The change of the geometry caused by the addition of the logs required a modification in the regions included in the bodies of influence. First, BOI 4 and BOI 5 on the unloaded timber truck had the same size but covered different regions of the domain; for the fully-loaded timber truck these two BOIs were merged in one that covers all the flow region closer to the truck. Moreover, the length of all the BOIs was increased in the x-direction to completely capture the main wake that now is also created by the logs and not just by the cabin. The element sizes of these new BOIs was also changed to rounded numbers starting from 24 mm, Table 3.8; and the regions can be seen on Fig. 3.15.

Table 3.8: Volume mesh sizes used on the fully-loaded timber truck.

Region	Element size [mm]
BOI 1	192
BOI 2	96
BOI 3	48
BOI 4	24
Outer Domain	1800

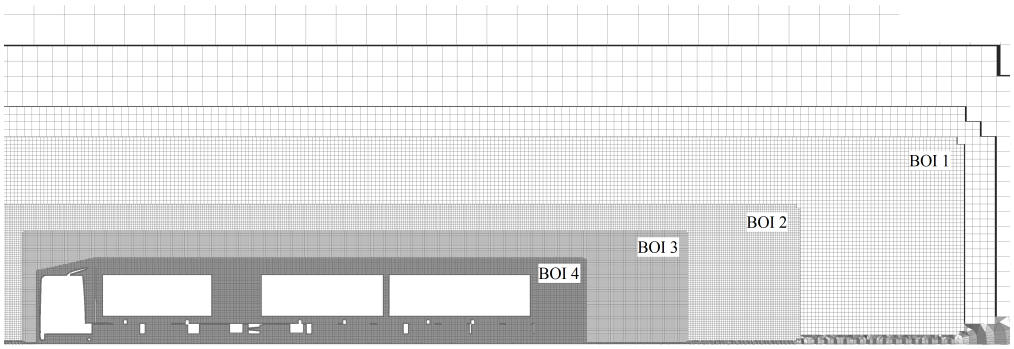

(a)

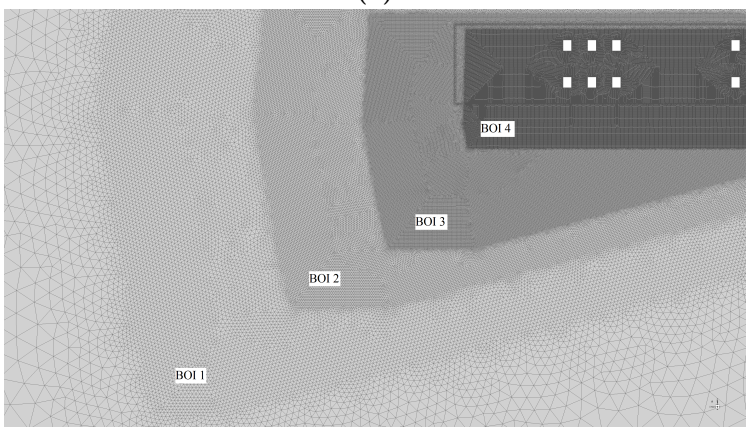

(b)

Figure 3.15: Bodies of influence used on the fully-loaded timber truck volume mesh.

Regarding the prism layers used on the surfaces, new sets needed to be defined in order to obtain a good transition between the different surfaces and to introduce enough layers in the new surfaces added with the logs. The stacks of logs were introduced in Set 3 together, keeping the same surface element sizes but reducing the total number of prism layer and the first-node-height to be able to introduce them in the holes left in between the logs without causing collisions. After adding the logs and creating the small faces to connect them to the stakes and bunks as explained on Sec. 3.2.1; the stakes and bunks needed a smaller surface element size to be able to place enough element on those small surfaces and also the same number of prism layers than the logs for a good transition in that region. Hence, a new set for the stakes and the bunks was defined with the original surface element size of Set 1 of the unloaded timber truck and the same number of layers used on Set 3.

The final setup for surface mesh and prism layers for the fully-loaded timber truck is shown on Table 3.9.

Table 3.9: Surface mesh sizes used on the fully loaded timber truck.

Region	Min. size [mm]	Max. size [mm]	No. of layers	First-node-height [mm]
Set 1	6	14	16	0.75
Set 2	8	18	16	1
Set 3	9	18	8	1
Set 4	-	-	6	- (1^{st}layer AR=8)
Set 5	6	14	8	1

With these adapted values from the unloaded timber truck, the baseline model mesh of the fully-loaded timber truck reached 153 million elements if the flow inside the logs is considered and 126 million elements for the closed stacks simplified model.

3.3 Post Processing

This subsection presents the main variables used for the results analysis and discussion and the reference values used for their calculations, for both the study on the Allan body and on the timber truck.

3.3.1 Reference values

Table 3.10 shows the reference values used on the post-processing of the Allan body and the timber truck to obtain the different non-dimensional coefficients.

Table 3.10: Reference values used on the post-processing of the results.

Variable	Allan body	Timber truck
Density (ρ_∞) $[kg/m^3]$	1.225	1.225
Dynamic viscosity (μ_∞) $[Ns/m^2]$	1.789e-5	1.789e-5
Velocity (u_∞) $[m/s]$	24.4	22.222
Frontal Area (S_{ref}) $[m^2]$	0.0465	10.4
Characteristic length (l_c) $[m]$	0.305	3.225

3.3.2 Resultant variables

The following variables are the ones obtained for every case studied on this report and used for the comparisons between them.

Pressure coefficient

Static pressure coefficient is used on the surfaces of the models and is defined as:

$$C_P = \frac{p}{q_\infty} = \frac{p}{\frac{1}{2}\rho_\infty u_\infty^2} \tag{3.1}$$

Total pressure coefficient is used on flow points and is defined as:

$$C_P tot = \frac{p+q}{q_\infty} = \frac{p+\frac{1}{2}\rho u^2}{\frac{1}{2}\rho_\infty u_\infty^2} \tag{3.2}$$

Where p and q are, respectively, the static and dynamic pressure at the evaluation point and q_∞ the dynamic pressure in the freestream flow.

Friction coefficient

Skin friction coefficient is used to evaluate the friction forces on the walls and to detect regions with separated flow, the variable is defined as:

$$C_f = \frac{\tau_w}{q_\infty} \tag{3.3}$$

Where τ_w is the wall shear stress on the desired point of the surface.

Drag coefficient

The drag coefficient is the main variable of interest for truck aerodynamics and is defined as the non-dimensional form of the force acting on the opposite direction of the velocity of the body, drag D.

$$C_D = \frac{D}{q_\infty S_{ref}} \tag{3.4}$$

Wind averaged drag coefficient

Due to the great influence of cross-wind conditions on the aerodynamic performance of road vehicles, a new variable called wind average drag coefficient is defined in order to obtain a drag value representative of real road conditions. For this a range of yaw angles is calculated and then averaged following different methods, as explained on [12], to obtain the final value of wind averaged drag coefficient (C_{DW}).

The two methods used on this report are the MIRA and the SAE J1252 methods, explained in detail on [12]. Both methods assumed a fixed vehicle velocity. However, MIRA uses seven different wind velocities (from 2 to 26 km/h), weighted with different factors. Whereas in SAE a fixed wind velocity (11.3 km/h) is used and assumes that this wind approach the vehicle with the same probability on any direction.

The baseline model of this report is simulated for 0, 2.5, 5, 7.5, 10 and 15 degrees yaw angle conditions, and with these results the wind average value is calculated following two different methods, MIRA and SAE. A comparison between the average and the individual values for each yaw angle is used to determine which angle is more representative of the whole sweep, and therefore it can be used for the study of the different aerodynamic concepts. It must be taken into account that the SAE method for the wind average is the current standard in the industry and hence it would be considered more important in case of disagreement between the two methods.

3.4 Improved simulation speed

In this section the procedure used during the methodology development part of this thesis is explained. The aim of this study is to reach a steady state converge solution within fewer iterations by the use of the URANS model with the adequate time step size and solver settings.

During the study three different models were used: Allan body, NACA 0008 airfoil and Ground Transportation System (GTS) model; in this particular order due to the results found on the first stages as explained on Sec. 4.6.

The procedure consisted of; first, analyze the effects on independent parameters on the results, such us the Pressure Based Coupled solver Courant number (PBC-Courant on the figures) or the number of iterations inside each time step. The settings providing better results in terms of faster convergence of the drag coefficient monitor over iterations, were later combine together to see the overall impact. The convergence was also studied by analyzing the drop of the residuals for the different settings, as an addition to the drag coefficient monitor. Finally, different time step sizes were used in the same simulation, by changing the setup after a fixed number of iterations, to study if the fastest convergence obtained by changing the solver settings could be further improved.

3.4.1 Allan body

The methodology study for the simulation speed improvement was first carried out on the Allan body geometry, the same test model used for the mesh types and turbulence models for the timber truck work. The shorter gap distance, $g/b = 0.17$, was chosen for this study; and, since no cross wind condition was applied on this study, only half of the model was used. Therefore, the final 4.6 million elements hexahedral mesh chosen after the mesh study on the Allan body, Fig. 3.16 was the one used for the URANS approach of the solver. The quality of this is mesh is a maximum value of 0.85 of Skewness, 0.89 of ICEM Quality and 0.85 of Inverse Orthogonal Quality.

The boundary conditions used for the Allan body simulations are the same explained on Sec. 3.1.2 and shown on Table 3.2.

For the steady RANS solver setup, used as a reference for convergence throughout the

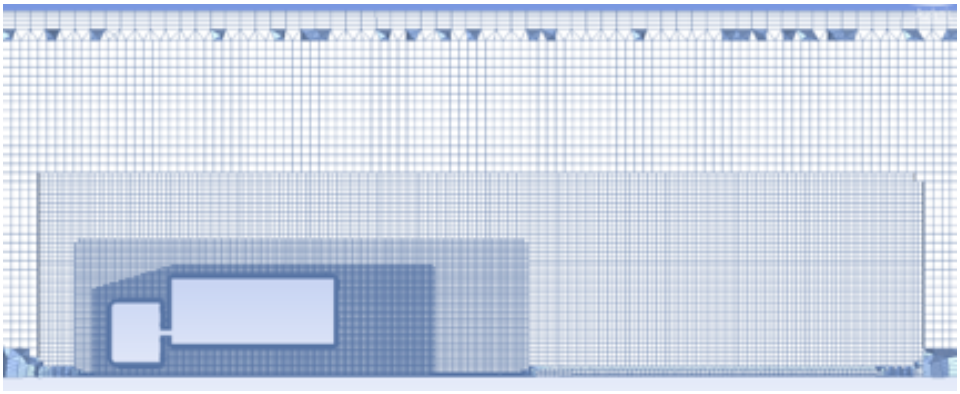

Figure 3.16: 4.6 million hexahedral mesh used for the simulation speed study on the Allan Body.

URANS simulations, the same setup indicated on Sec. 3.1.2 was applied. Important to notice for the simulation speed study is that the Courant flow number of the Pressure Based Coupled solver (PBC-Courant) was 200, the explicit under relaxation factor on the variables in the pressure and momentum equations was 0.75 and the implicit under relaxation factor on the turbulence model equation, k and ε, was set to 0.8; which are the default values on ANSYS Fluent.

Table 3.11: Baseline solver setup for the URANS model simulations on the Allan Body.

Solver	Pressure Based
Algorithm	Coupled
Temporal disc.	First Order Implicit
Gradients disc.	Least Squares Cell-Based
Pressure disc.	Standard
Momentum disc.	Second Order Upwind
Turbulence kinetic energy (k) disc.	First Order Upwind
Turbulence dissipation rate(ε) disc.	First Order Upwind
Time step size [s]	0.1
Time scale factor (α_t)	8
Iterations/Δ_t	2
PBC-Courant	200
Explicit UR. factor Pressure eq.	0.75
Explicit UR. factor Momentum eq.	0.75
Implicit UR. factor k eq.	0.8
Implicit UR. factor ε eq.	0.8

The baseline solver setup for the unsteady simulations using URANS consisted on the same discretization schemes used for the steady state simulations, with the same values for the Pressure Based Coupled solver Courant flow number and under relaxation factors. For the transient solver a time step of 0.1 seconds and 2 iterations inside each time step were used. This time step size corresponds to a time scale factor (α_t) of 8, based on the characteristic time (t_c) of the problem, 0.0125 seconds

from equation (3.5) .The parameters to be tuned during the study are: the gradient discretization scheme, the time step size, the number of iterations per time step, the Pressure Based Coupled solver Courant number, and the under relaxation factors. The indications in legends and captions on the results, Sec. 4.6, are changes with respect to the baseline setup describe on Table 3.11.

$$t_c = \frac{l_c}{u_\infty} \tag{3.5}$$

Where the height of the model has been used as the characteristic length ($l_c = b = 0.305$) m. and the freestream velocity is $u_\infty = 24.4$ m/s.

$$\Delta_t = \alpha_t \, t_c \tag{3.6}$$

During the simulation speed methodology study, the initialization of the flow field was not done with the Full Multi Grid approach, instead a standard initialization to 0 m/s velocity was used and the first 20 iterations were run with the RANS model before changing to the URANS solver.

3.4.2 NACA 0008

For the NACA airfoil a quad mesh was generated on ICEM CFD with 48000 elements and a minimum ICEM quality of 0.91, Fig. 3.17. The computational domain used consisted on 10 chord lengths between the inlet and the airfoil, 15 chord lengths until the outlet, and 10 chord lengths on top and bottom of the airfoil.

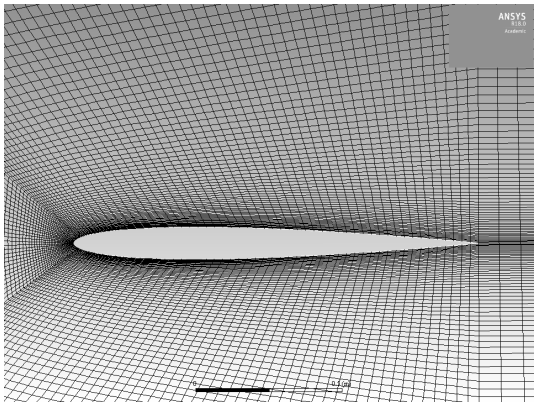

Figure 3.17: Detail of the quad mesh used on the NACA 0008 airfoil for the simulation speed methodology study.

The boundary conditions applied for these 2D simulations are shown on Table 3.12. The velocity in the inlet was set to keep the same Reynolds number that was used on the Allan body simulations, that is a velocity of 7.302 m/s to obtain the same 0.51e6 Reynolds number, in this case based on the chord length (1 m) and with sea level properties, $\rho = 1.225 \; kg/m^3$ and $\mu = 1.789 \cdot 10^{-5} \; kg/ms$.

The numerical setup for the steady RANS solution was the same used for the Allan body study, and the only difference on the URANS setup with respect to the settings

Table 3.12: Boundary conditions used on the NACA 0008 simulations.

Boundary zone	Condition
Inlet	Velocity-inlet
Outlet	Pressure-outlet
Top wall	Symmetry
Bottom wall	Symmetry
Airfoil wall	Stationary, no slip wall

shown on Table 3.11 was the time step size; in this case the time step size, equation 3.6, was set using a scale factor (α_t) of 2.5 based on the characteristic time of the problem (t_c), equation 3.5; that is, for a characteristic length (l_c) of 1 meter and a freestream velocity (u_∞) of 7.302 m/s corresponds a characteristic time of 0.137 seconds, hence the time step size used on the URANS baseline set up was 0.35 seconds.

3.4.3 Ground Transportation System model

Next step on the methodology investigation was performed in a 3D model, in this case the Ground Transportation Model (GTS), Fig. 3.18, which is a simplified model of a cab-over-engine tractor trailer combination without gap or wheels, [21], used in this study to avoid the convergence problems found due to the separation on the gap region of the Allan body geometry explained on Sec. 4.6.1.

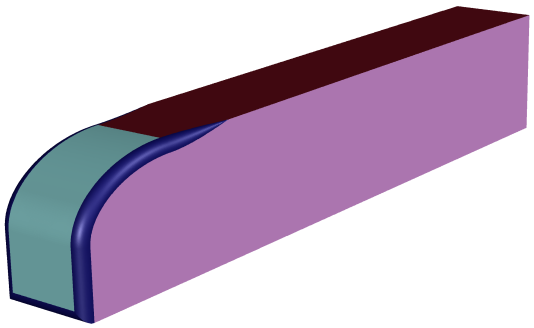

Figure 3.18: Ground Transportation System (GTS) model geometry.

A hexahedral mesh with quality of maximum 0.89 of Skewness, ICEM Quality and Inverse Orthogonal Quality, was used for the GTS model geometry, Fig. 3.19.

The boundary conditions used on the GTS cases are shown on Table 3.13; in this case the velocity on the inlet, and on the moving ground, is set to 29.21 m/s for a Reynolds number of 2.785e6, based on the height of the model b=1.392 meters and at sea level conditions, $\rho = 1.225\ kg/m^3$ and $\mu = 1.789 \cdot 10^{-5}\ kg/ms$. This is a Reynolds number commonly used in experimental and CFD studies on the GTS model.

According to the better results obtained when using the Green-Gauss Node Based scheme, instead of Least Square Cell-Based, for the gradient discretization in the

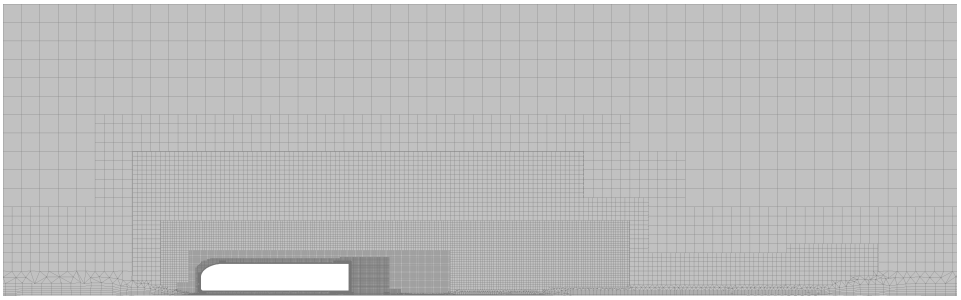

Figure 3.19: Detail of the hexahedral mesh used for the simulations on the GTS model.

Table 3.13: Boundary conditions used on the GTS model simulations.

Boundary zone	Condition
Inlet	Velocity-inlet
Outlet	Pressure-outlet
Top wall	Symmetry
Right wall	Symmetry
Left wall	Symmetry
Ground	Moving, no slip wall
GTS walls	Stationary, no slip wall

previous cases, Sec. 4.6.1 and 4.6.2; it has been implemented as part of the steady RANS setup and the baseline URANS solver setup for the study on the GTS model. The rest of the settings for the steady RANS solver are the same explained for the Allan body on Sec. 3.1.2. For the unsteady simulations, the same scale factor of 2.5 used on the NACA airfoil is applied on the GTS to obtain the time step size for the baseline setup; in this case the characteristic length used is the height of the model, b=1.392 meters, together with a freestream velocity of 29.21 m/s results in a characteristic time of 0.04765 seconds. Hence, the time step size used on the baseline setup was 0.12 seconds. All the settings used on the baseline setup for the GTS model are listed on Table 3.14.

On the GTS model a time step size analysis was also carried out, for this the time scale factor (α_t) was modified after the first 50 iterations of the URANS solver. According to [23], it is better to have a larger time step in the beginning, hence in this study the time step was reduced to half after the first 50 iterations.

Table 3.14: Baseline solver setup for the URANS model simulations on the GTS model.

Solver	Pressure Based
Algorithm	Coupled
Temporal disc.	First Order Implicit
Gradients disc.	Green-Gauss Node Based
Pressure disc.	Standard
Momentum disc.	Second Order Upwind
Turbulence kinetic energy (k) disc.	First Order Upwind
Turbulence dissipation rate(ε) disc.	First Order Upwind
Time step size [s]	0.12
Time scale factor (α_t)	2.5
Iterations/Δ_t	2
PBC-Courant	200
Explicit UR. factor Pressure eq.	0.75
Explicit UR. factor Momentum eq.	0.75
Implicit UR. factor k eq.	0.8
Implicit UR. factor ε eq.	0.8

4 Results and Discussion

This section presents the results obtained for the different geometric models studied on the fully-loaded timber truck; starting from the baseline model, implementation of aerodynamic concepts of the baseline, and a final model of the timber truck as a combination of concepts for a higher overall reduction of drag values; and different possibilities in terms of loading configurations.

4.1 Baseline model

4.1.1 Effect from stack geometry

First the results for the baseline model consisting of logs of diameters between 320 and 350 millimeters in stacks of 2520 millimeters height with respect to the frame are exposed; for this baseline case a whole sweep of yaw angles simulations were carried out to study crosswind conditions, and an analysis to determine if the importance of considering or not the flow inside the stacks was significant for the flow field results was done.

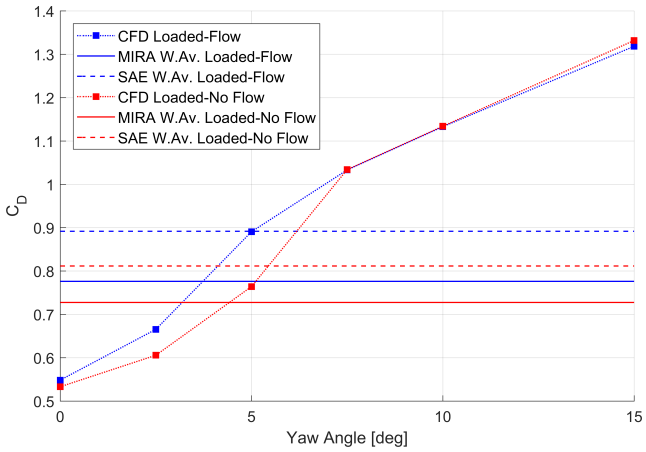

Figure 4.1: Baseline model drag coefficient for different yaw angles.

Fig. 4.1 and Table 4.1 show the drag coefficient results for the baseline model, and the simplified baseline model with closed stacks (no flow through), compared with the wind average drag coefficient obtained with the two different methods explained on Sec. 3.3.

It can be seen on Fig. 4.1 that the drag coefficient value obtained for a yaw angle of 5 degrees is the one in better agreement with the wind average drag coefficient, especially if obtained with the SAE method which is the current standard in the industry; hence, it was decided that the next simulations would be run for this yaw angle since the results can be considered representative of the whole sweep.

Table 4.1: Drag coefficient results for the added inlet investigation.

Yaw angle [deg]	C_D Real, Flow	C_D Simplified, No Flow
0	0.548	0.533
2.5	0.665	0.606
5	0.891	0.764
7.5	1.033	1.033
10	1.133	1.134
15	1.318	1.332
MIRA Wind Av.	0.776	0.727
SAE Wind Av.	0.891	0.812

Regarding the comparison between opened or closed stacks, and the validity of the simplification of removing the flow inside the logs; it can be noted from Fig. 4.1 how the results agree with each other for no crosswind conditions, where not much flow is expected to go through the stacks. However, there is a clear disagreement for 2.5 and 5 degrees yaw angles, for these cases more flow is expected to be in the gap region and therefore more of it can go through the stacks. In both cases the simplification of closing the stacks yielded less drag coefficient that the case in which the flow inside was modeled. Again, for bigger yaw angles the results agree again indicating that some other flow features, separation, influence more the results for those cases than the consideration of the flow inside the stacks. This can also be seen from a drag build up comparison, Fig. 4.2, where no significant difference are found for 0 or 10 degrees but a clear disagreement between the two models is present for 5 degrees of yaw angle. Moreover, it can be noted that the difference is mainly generated on the cab region, after that both models follow a similar trend.

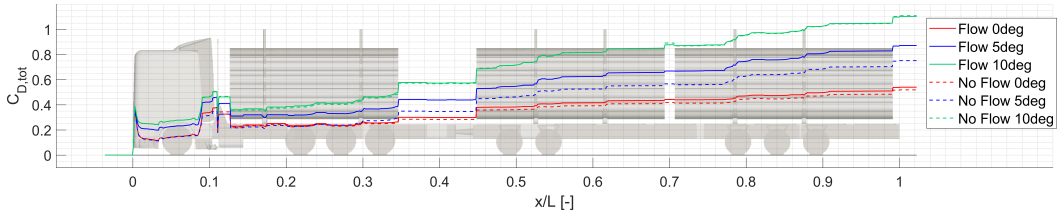

Figure 4.2: Drag coefficient build up comparison between the model with flow and without flow through the stacks for three different yaw angles.

From the surface breakdown of the total drag coefficient shown for both cases on Fig. 4.3, it can be noted that the major difference between the two cases for the 5 degrees yaw angle conditions comes from the cabin, followed by the wheel and the bulkehead, and not from the stacks where the simplification of the flow was carried out. This indicates that removing the flow through the stacks influences the general flow field around the truck, specially the region close to the cabin and the bulkhead where the major drag value difference are found.

The value of the skin friction coefficient on the right side of the cabin, Fig. 4.4, shows that the flow is clearly separated ($C_f = 0$) on the real case, whereas it keeps attached ($C_f > 0$) for the simplified model without flow going through the stacks.

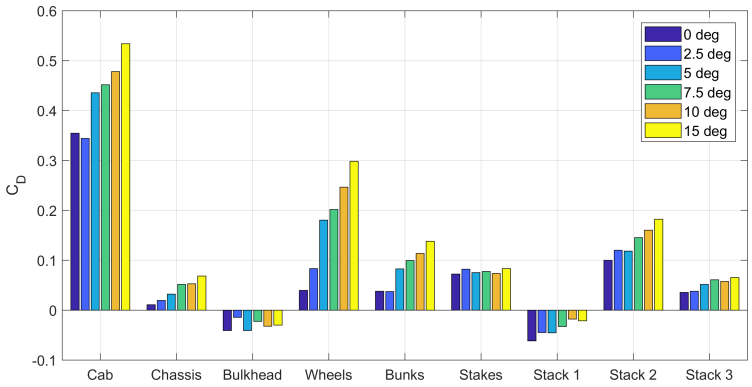

(a)

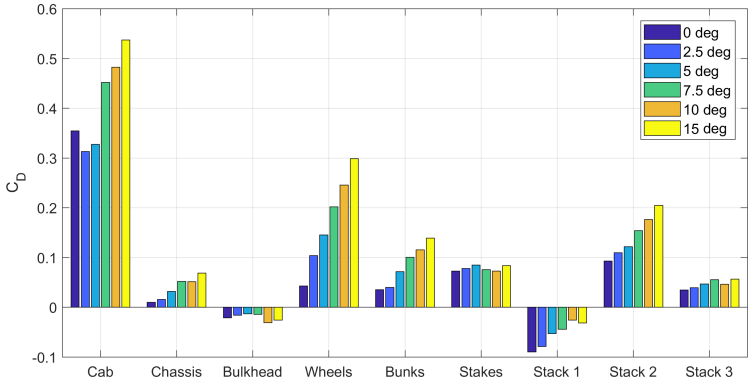

(b)

Figure 4.3: Surface breakdown of the total drag coefficient for the baseline model and the different yaw angles; flow through stacks (a), no flow through stacks (b)

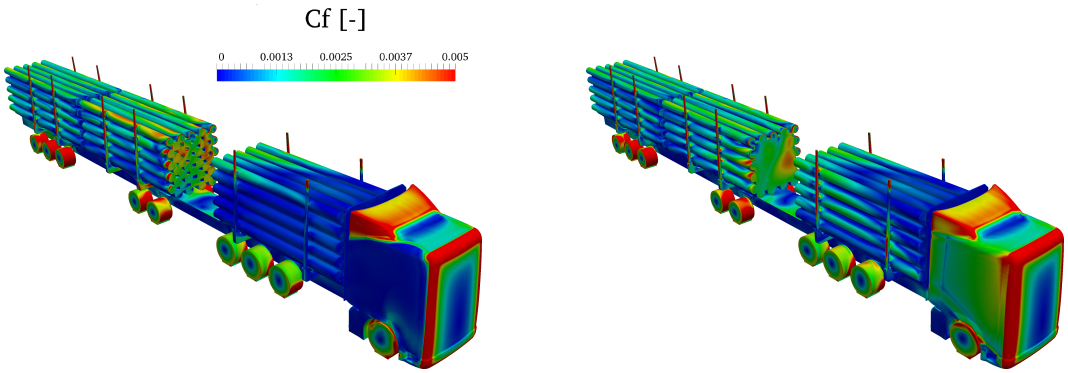

(a) (b)

Figure 4.4: Skin friction coefficient for 5 degree yaw angle; flow through stacks (a), no flow through stacks (b)

If the case of 5 degrees yaw angle, Fig. 4.5, is compared with one of the larger yaw angles with smaller difference in drag coefficient, such as 15 degrees, Fig. 4.6; it can be noted that the difference in total drag coefficient for the cases with 5 degrees comes from the separation on the right side of the cabin, which is not present if the flow inside the stacks is not considered. However, for the larger angle this separation exists for both, flow and no flow through the stacks, conditions. This indicates that

the separation for large yaw angles (starting from 7.5 degrees) is caused by the crosswind; however, for smaller yaw angles (2.5 and 5 degrees) the presence of flow inside the stacks have an impact of the separation in the cabin and therefore in the final total drag coefficient value.

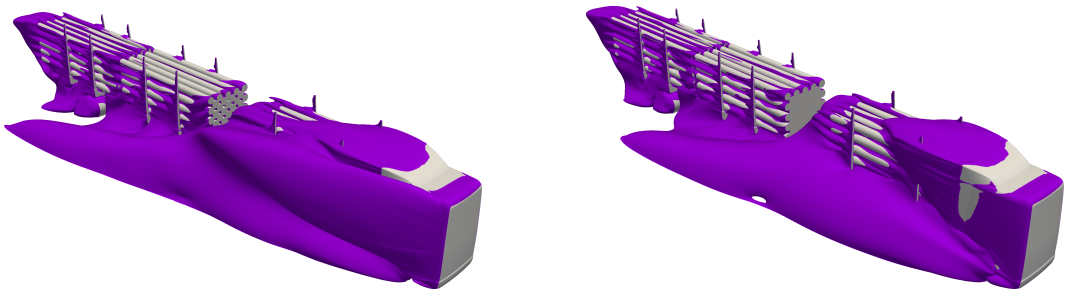

(a) (b)

Figure 4.5: Iso-surfaces of total pressure coefficient equal to zero for 5 degree yaw; flow through stacks (a), no flow through stacks (b)

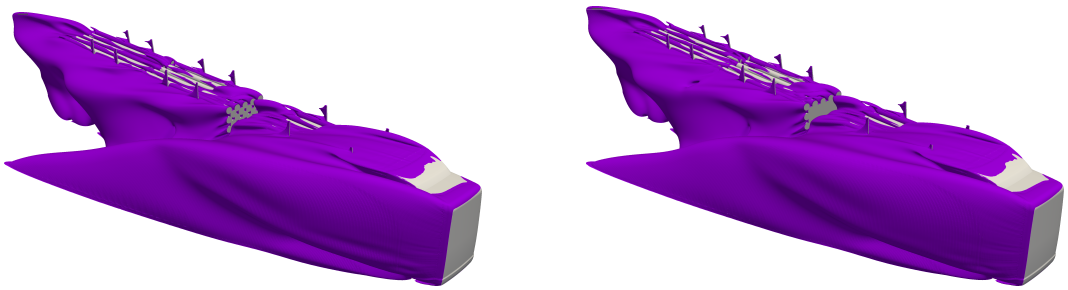

(a) (b)

Figure 4.6: Iso-surface of total pressure coefficient equal to zero for 15 degree yaw; flow through stacks (a), no flow through stacks (b)

In order to assess how significant could the influence of the flow inside the stacks be for the separation on the cab found in the 2.5 and 5 degree yaw angle cases; the amount of flow going through the stacks was measured, for the 5 degrees yaw angle reference case and on the first and second stack where the impact on the global flow field can be greater. A mean x-velocity of -3.64 m/s was measured inside the first stack, that is a mass flow rate of 2.23 kg/s going upstream; on stack 2 the mean x-velocity was 4.29 m/s, for a mass flow rate of 2.63 kg/s on the same direction as the freestream flow. If the frontal area of the stacks and the freestream velocity are used to calculate a reference mass flow rate for the logs; 1.82% and 2.15% of that reference value is going inside the first and second stack respectively.

As seen on Fig. 4.7 the separation occurs on the cabin and the reverse flow inside the first stack can influence that region when going out in between the bulkhead and the first stack to the leeward direction. The velocity of the flow between the bulkhead and the first stack of logs was measured on the 5 degrees yaw angle case; as seen on Fig. 4.8 the flow going through the stack is then leaving that region with a velocity of 2 m/s on the leeward direction, whereas no flow in the leeward direction is found on the simplified model with the closed stacks.

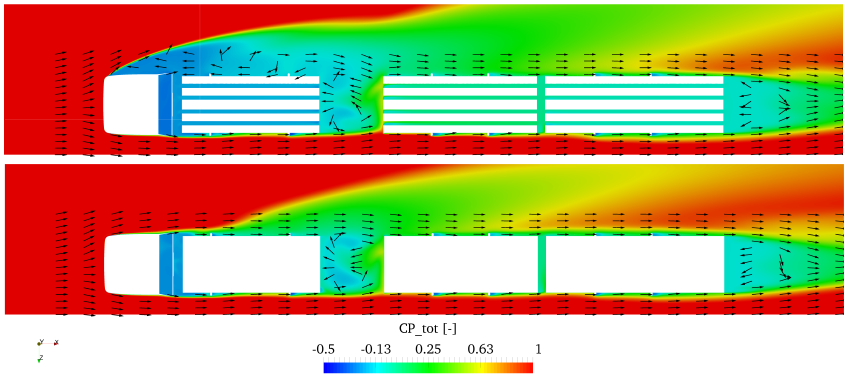

Figure 4.7: Total pressure coefficient and flow direction on a plane at y=1.25 m for 5 degrees yaw angle; flow through stacks on top, simplified no flow model on bottom.

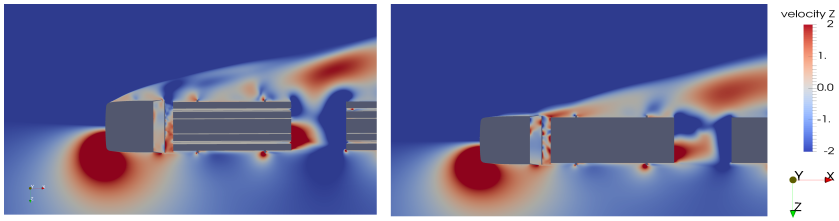

Figure 4.8: Contour of z-velocity on the y=0.89 m plane, detail of leeward flow on the bulkhead region.Real model with flow through on the left, simplified model on the right.

Fig. 4.9 shows the flow characteristics on the region between the bulkhead and the first stack; it can be seen how the case with flow through the stacks already presents a separation wake (low pressure region) on this x-position, whereas the simplified model on Fig. 4.9(b) maintains the flow attached on the leewards side of the truck. As explained before, and indicated here by the arrows on Fig. 4.9, the z-velocity of the flow going out the first stack on Fig. 4.9(a) is the main difference between the two cases and the probable cause for the separation on the cabin.

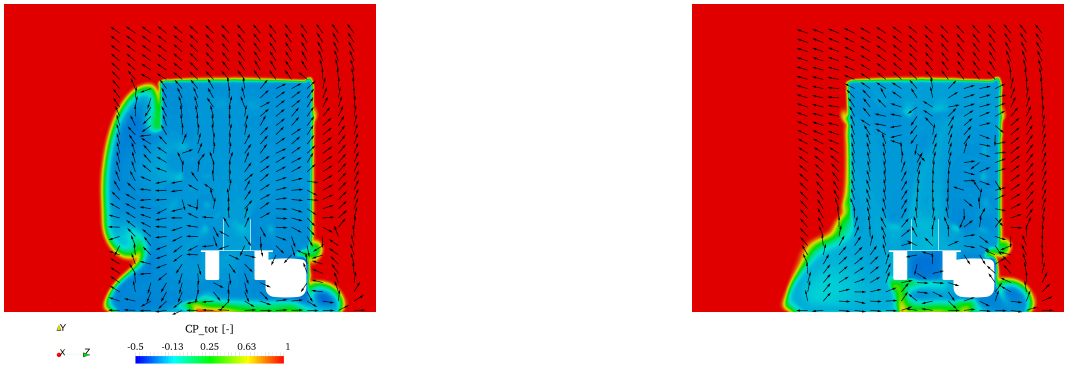

(a) **(b)**

Figure 4.9: Contours of total pressure coefficient for 5 degree yaw at x=-7.13 m; flow through stacks (a), no flow through stacks (b)

To prove that this velocity in the leeward direction was the reason for the different separation behavior on the cabin, a fictitious inlet was added behind the bulkhead, Fig. 4.10, on the simplified closed stacks case with the same velocity measured on the real case, 2 m/s.

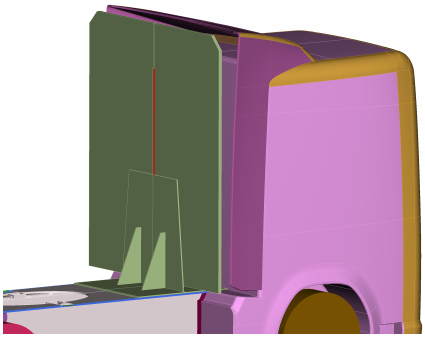

Figure 4.10: Fictitious inlet added behind the bulkhead, marked in red.

Flow field results on Fig. 4.11 show that the separation on the cabin is present when a z-velocity is added on the bulkhead, a similar result of the one obtained with the realistic model, Fig. 4.11 top.

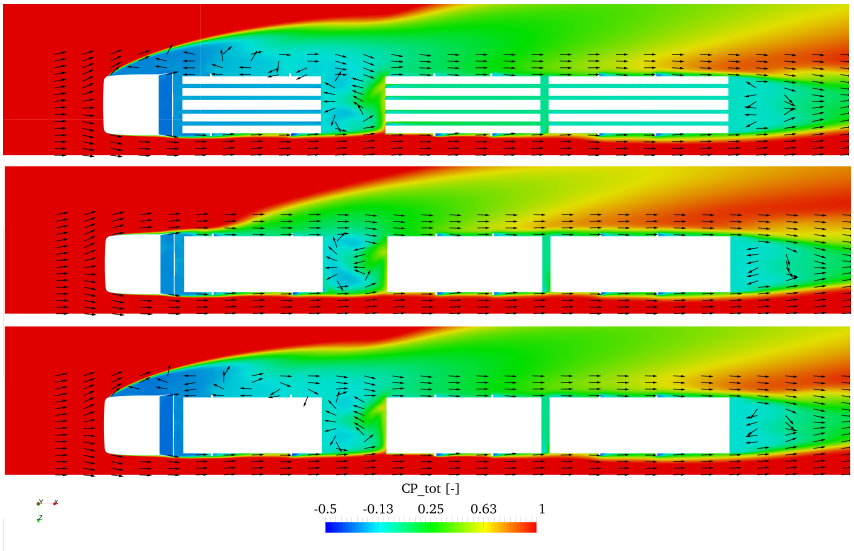

Figure 4.11: Total pressure coefficient and flow direction on a plane at y=1.25 m for 5 degrees yaw angle; real open stacks model on top, original closed stacks model in the middle, model with fictitious inlet on bottom.

Table 4.2: Drag coefficient results for the added inlet investigation, for 5 degrees yaw angle.

Model	C_D	% from real
Real, flow through	0.891	-
Simplified, no flow through	0.764	-14.3
Simplified, added inlet	0.872	-2.13

The results shown on Table 4.2 indicate that the simplification of the flow inside the logs is not realistic since the influence on the flow field is significant and the total value of drag coefficient is reduced by a 14% when the openings are closed. Hence, this simplified model was discarded and the rest of the studies on the fully-loaded timber truck were done on a more realistic model in which the flow inside the stacks was modeled.

4.1.2 Baseline, realistic model

To study the overall flow field for the realistic baseline model and later implement aerodynamic concepts that could improve its performance, it is worth noting from Fig. 4.3(a) that the cabin, the wheels, the bunks and the second stack (gap region), are the main contributors to the total drag on the baseline model for the representative 5 degrees yaw angle case; hence, the aerodynamics concepts should focus on improving the flow on those regions. These regions can also be seen in the drag coefficient build-up shown on Fig. 4.12 where an increase in drag is present at the position of each of these components. Analyzing the drag build-up along the truck starting from its front; it can be seen how, after the initial increase of drag at the front face of the cabin, there is a decrease of drag on the rounded edges of the cabin due to the acceleration of the flow. The wheel of the cabin influences the flow and a rise of drag can be noted both on the front and the back of the wheel. In between the cabin and the bulkhead there is a low pressure region which causes and opposite effect on these components; the suction is creating drag on the back face of the cabin while pushing the truck forwards on the front face of the bulkhead. The same effect is also present on the next region after the bulkhead and before the first stack, now increasing the total drag on the bulkhead and decreasing it on the front face of the stack. Fig. 4.3 shows how the overall change of drag in both the bulkhead and the first stack surfaces is negative, meaning that the suction in their front faces is stronger than the one creating drag on the back. Going along the first stack the drag increases continuously, with bigger changes at the positions of the bunks and the wheels. The gap between the first and second stack is one of the most important regions to consider in terms of drag reduction, since both faces on the gap contribute significantly to the total drag of the truck. The suction created by the separated flow after the first stack increases the drag on its back face; whereas the flow hitting the front face of the second stacks pushes the truck backwards also increasing its drag. From the second stack until the end of the truck, the drag continues increasing with the same behavior as before at the position of the wheels and bunks. The gap between the second and third stack is much smaller and its effect on the drag not as significant as the main gap. Finally, the drag increases on the back face of the third stack due to the low pressure region generated in the wake.

Regarding the cabin, as explained before, the drag comes mainly from the separation on the leeward side; however, the study of the cabin is beyond the scope of this report and no modifications of its shape were implemented. The focus instead was centered on the other regions that are explained on more detail below.

From a global distribution of pressure around the truck, the x-component since is

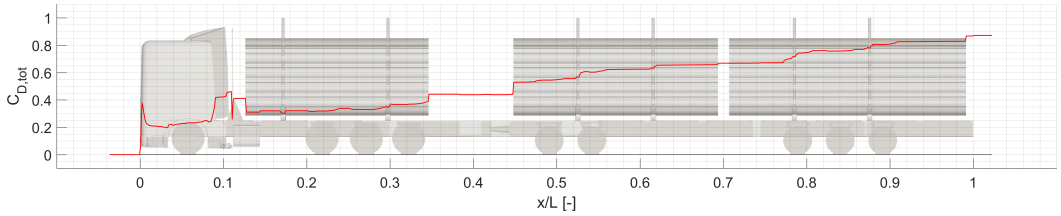

Figure 4.12: Drag coefficient build-up along the truck for the baseline model at 5 degrees yaw angle.

the one contributing to the drag Fig. 4.13, it can be noted that regions of high pressure pushing the truck backwards and increasing its drag are present mainly in the front of the cabin, the front of the second stack, the surfaces of the bunks and stakes exposed to the freestream flow and the front part of the wheels. Whereas suction regions appears on the zones of separated flow, such as the back face of the bulkhead and the first and third stack.

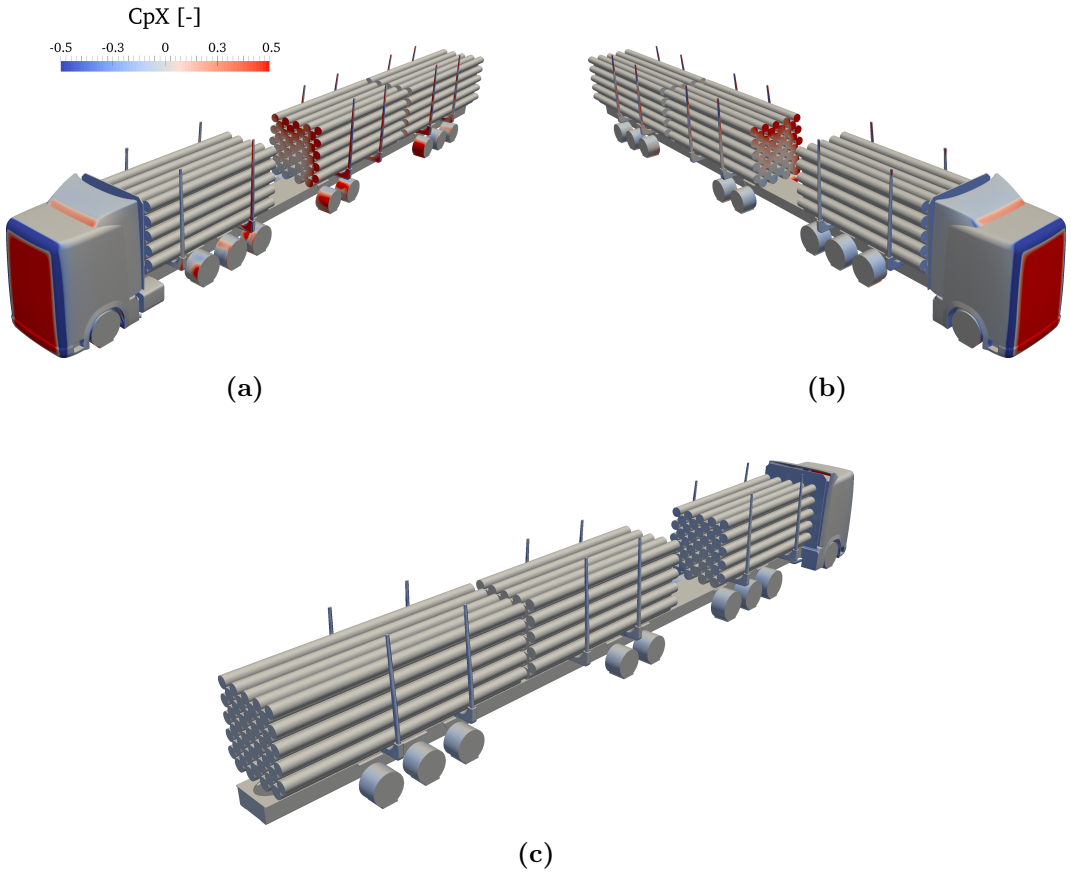

Figure 4.13: Contours of x-component of static pressure coefficient on the baseline model surfaces for 5 degree yaw.

Regarding the influence of the wheels on the total drag of the truck, it is important to consider the flow under the chassis of the truck. Fig. 4.14 shows that due to the cross wind conditions (5 degrees in this case) the flow enters from the windward side of the truck and the wheels after the gap on that side are the ones with higher

pressure and contribution to the drag. It is also worth noting how the flow on the underbody moves to the leeward side on the back of the truck creating a high pressure region also on the last wheels of that side.

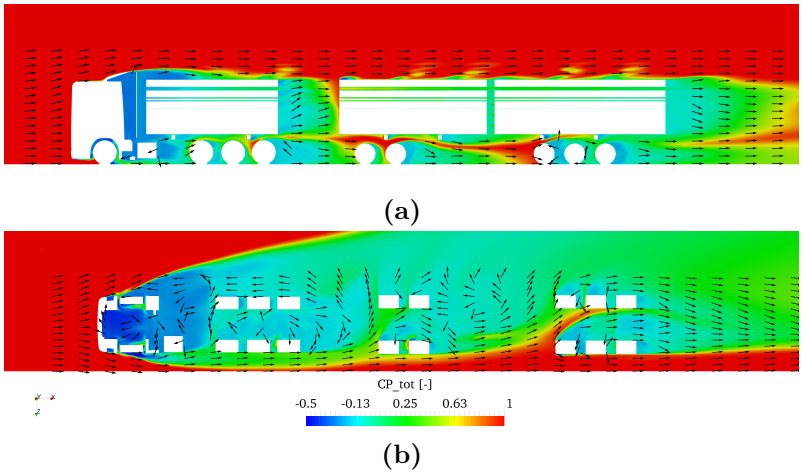

Figure 4.14: Contours of total pressure coefficient on the baseeline model for 5 degree yaw, at z=0.88 m (a) and y=-0.39 m (b)

On Fig. 4.14(a) it can also be seen a high pressure under the stacks, especially directly after the gap. This indicates that not only the surfaces of the bunks directly exposed to the freestram contribute to the drag, Fig. 4.13, but also the ones under the logs could add a significant value to the total drag of the truck. The flow field between the load and the chassis is shown on Fig. 4.15 and confirms that the bunks, especially the third and fifth ones, contribute to the total drag due to the high pressure on their front face along their whole span, and the suction region present downstream.

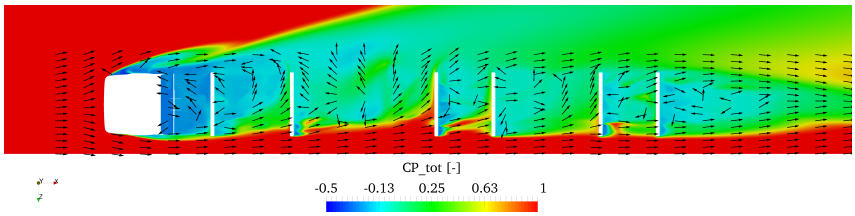

Figure 4.15: Contours of total pressure coefficient on the baseeline model for 5 degree yaw at y=0.34 m.

Finally, the last region with great influence on the total drag is the gap between first and second stack. Fig. 4.16(a), approximately on the symetry plane, shows that the flow separates behind the first stack creating a recirculation of the flow in the gap and a suction region affecting the back face of that stack. Whereas a higher pressure zone on the other side of the gap increases the drag of the truck on the front face of the second stack. This effect is even more important at position closer to the windward side of the truck, Fig. 4.16(b), where the freestream flow is impacting on that face.

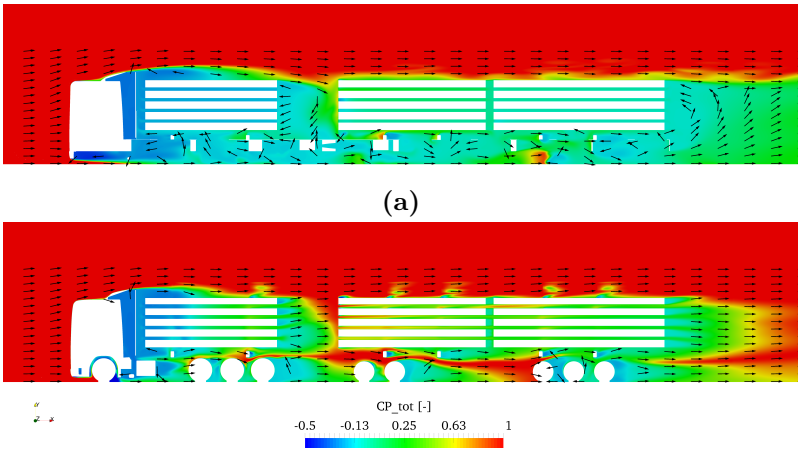

(a)

(b)

Figure 4.16: Contours of total pressure coefficient on the baseeline model for 5 degree yaw, at z=0.04 m (a) and z=1.02 m (b)

Considering all the flow field characteristics of the baseline model explained above, different aerodynamic concepts were implemented to modify the flow on those regions and reduce the total drag coefficient of the truck.

4.2 Aerodynamic concepts

4.2.1 Side-skirts

Due to the great influence of the underbody flow on the total drag coefficient of the truck, skirts were implemented on the baseline model to prevent all the flow to go under the chassis and to the wheels, Fig. 4.17. These side-skirts cover all the lateral part of the chassis, except from a small part where the joint of the trailer is positioned, a boat-tail shape was also included after the last wheel of the truck with the intention of reducing the size of the wake on the back.

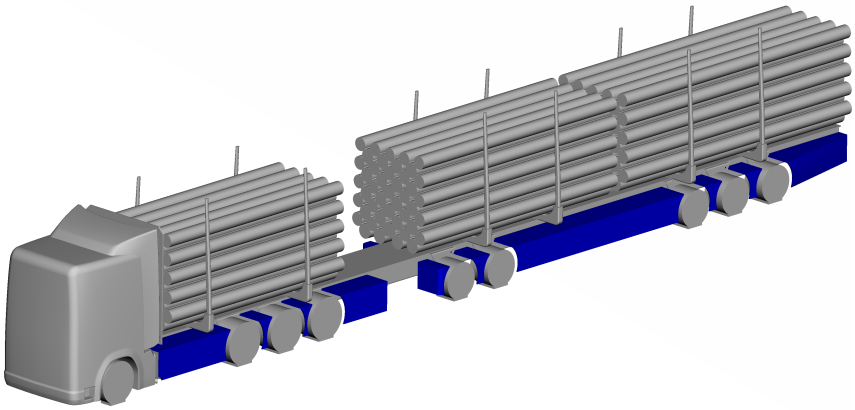

Figure 4.17: Side-skirts aerodynamic concept added to the baseline model.

The implementation of this concept yielded a total drag coefficient of 0.830, which means a reduction of 6.85% with respect to the baseline model, Table 4.3. This drag reduction comes mainly from the wheels; as seen on Fig. 4.20 the addition of the skirts removes the flow in between the wheels and therefore the high pressure region on the front of each of them, Fig. 4.18, now the highest pressure is only present on the skirt surface after the gap. Fig. 4.19 also shows that the suction region downstream of each wheel is smaller when using the skirts and, more important, how skirts avoid the underbody flow to go on the leeward side removing the high pressure region on the back wheels on that side.

Table 4.3: Drag coefficient results for the side-skirts aerodynamic concept compared with the baseline model, for 5 degrees yaw angle.

Model	C_D	% from baseline
Baseline	0.891	-
Side-skirts	0.830	-6.85

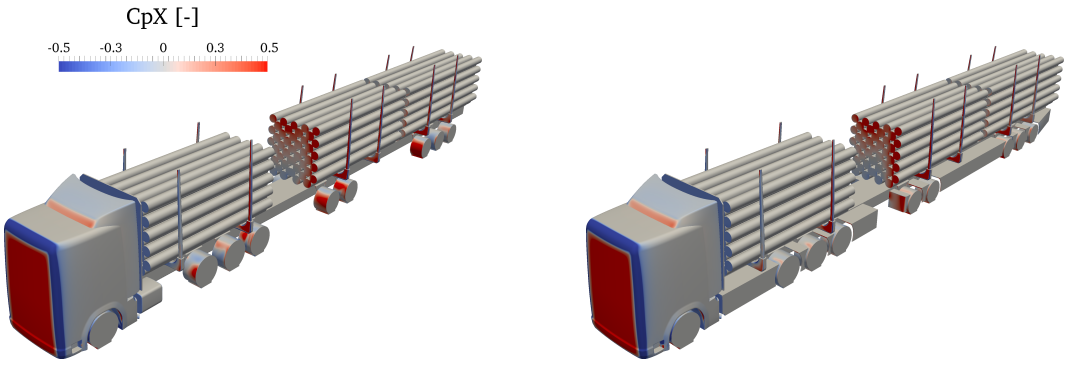

(a) **(b)**

Figure 4.18: Comparison of static pressure coefficient distribution between the baseline model (a) and the side-skirts aerodynamic concept (b). At 5 degree yaw angle.

The drag build up along the truck, Fig. 4.21, shows that the largest difference of drag coefficient with respect to the baseline model is found at the front face of the seventh wheel, as seen on Fig. 4.19 the addition of the skirts shielded the underbody removing the high pressure region upstream of the last set of wheels and therefore reducing the total drag.

Another shape of the skirts, without the gap in the middle of the chassis, was studied and resulted in less than a 1% reduction of drag coefficient, for the 5 degrees yaw angle case, with respect to the skirts explained above. Due to the more realistic implementation of the divided skirts, those were chosen for the following studies of aerodynamic concepts. Moreover, since the use of skirts improve the underbody flow, some of the other aerodynamic concepts analyzed are implemented together with the skirts.

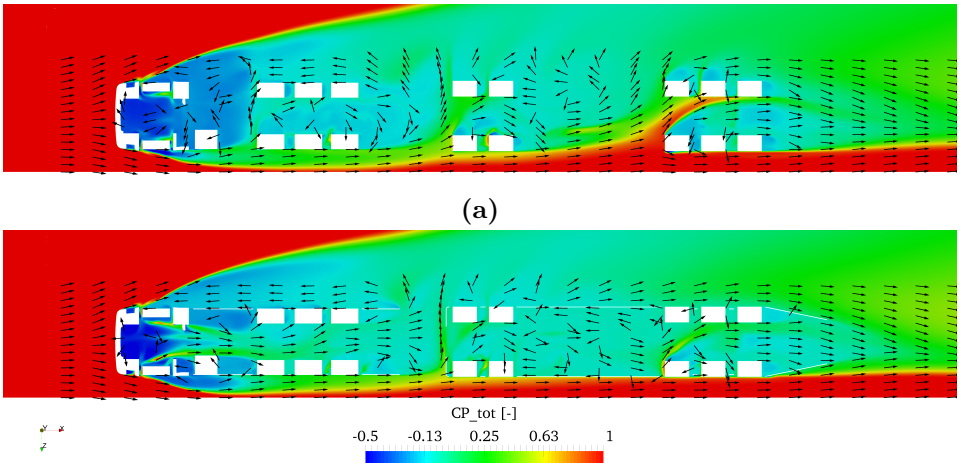

(a)

(b)

Figure 4.19: Comparison of total pressure coefficient on the underbody region (y=-0.39 m) between the baseline model (a) and the side-skirts aerodynamic concept (b). At 5 degree yaw angle.

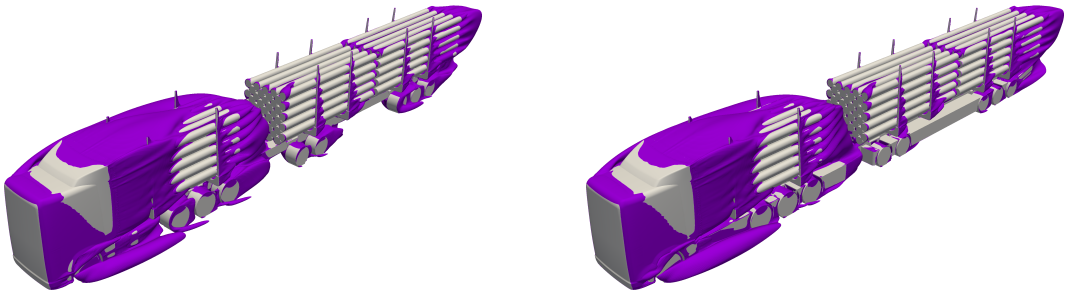

(a) (b)

Figure 4.20: Iso-surface of total pressure coefficient. Baseline model (a), side-skirts aerodynamic concept (b). At 5 degree yaw angle.

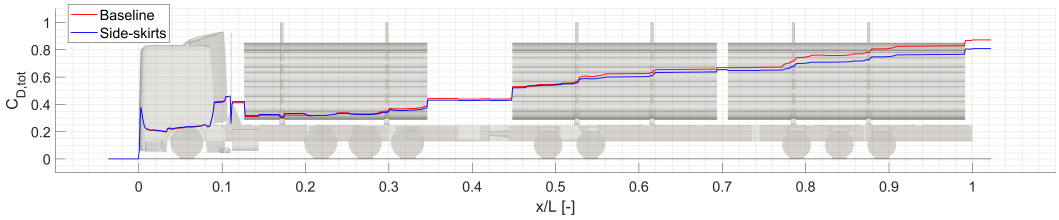

Figure 4.21: Drag coefficient build-up along the truck for side-skirts concept compared with the baseline model at 5 degrees yaw angle.

4.2.2 Closed bunks

The results of the baseline model showed that the surfaces of the bunks perpendicular to the freestream flow contributed significantly to the total drag, due to high pressure region under the load after the gap, and suction on the back faces of the bunks, Fig. 4.15. Hence, an aerodynamic concept as shown on Fig. 4.22 was implemented with the intention of removing or limiting the flow in between the pair of bunks supporting

each stack of timber; stacks were removed on Fig. 4.22 for easier visualization of the added concept.

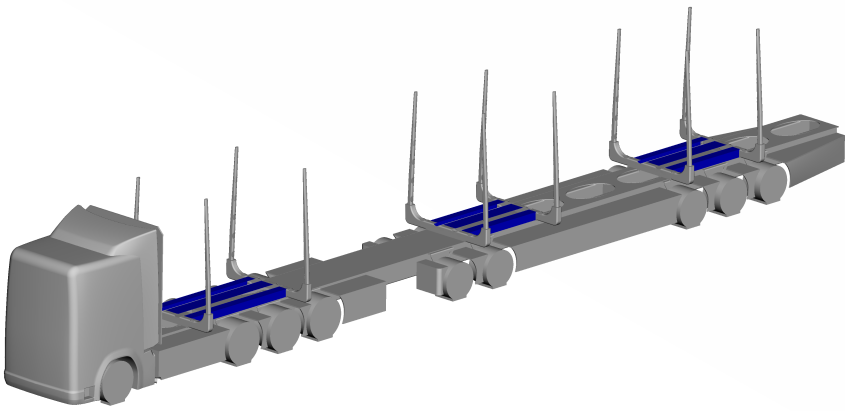

Figure 4.22: Closed bunks aerodynamic concept added to the baseline model, together with the side-skirts.

Table 4.4: Drag coefficient results for the closed bunks aerodynamic concept compared with the baseline model, for 5 degrees yaw angle.

Model	C_D	% from baseline	% from skirts
Baseline	0.891	-	-
Side-skirts	0.830	-6.85	-
Closed bunks	0.784	-12.0	-5.54

Closing the space in between each pair of bunks, together with the side skirts, resulted on a drag coefficient reduction of 12% with respect to the baseline model, that is a drag coefficient of 0.784, Table 4.4 shows also the comparison with the side-skirts model.

The flow field on the underload region, Fig. 4.23, shows that closing the central part of the bunks removes the recirculating flow in that region reducing the suction on the downstream side of the bunks. Moreover, preventing the flow from going on the leeward side also reduces the wake on the back of the truck. However, since the closing structure was only created on top of the frame, it does not remove the flow on the bunk region completely and, therefore, zones of high pressure on the front faces of the bunks are still present on the windward side of the bunks, especially on the bunks after the gap. This indicates that, for a further reduction of the drag coefficient, the whole span of the bunk should be closed.

From the drag build up of this aerodynamic concept, Fig. 4.24, it can be noted that no significant improvement is obtained with this aerodynamic concept on the bunks holding the first stack. However, with the flow field modifications shown on Fig. 4.23, the drag is reduced on the four bunks after the gap, both with respect to the baseline model and the side-skirts aerodynamic concept.

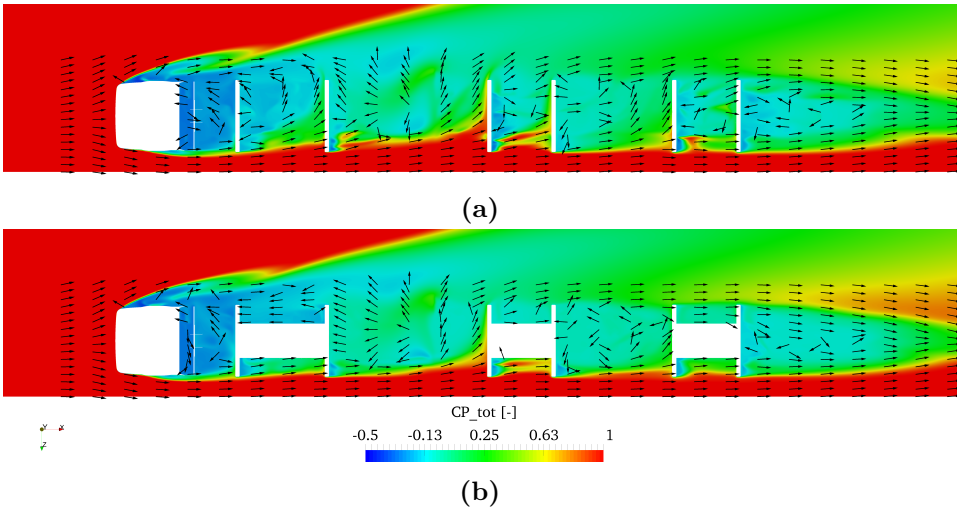

Figure 4.23: Comparison of total pressure coefficient on the underload region (y=0.34 m) between the baseline model (a) and the closed bunks with side-skirts aerodynamic concept (b). At 5 degree yaw angle.

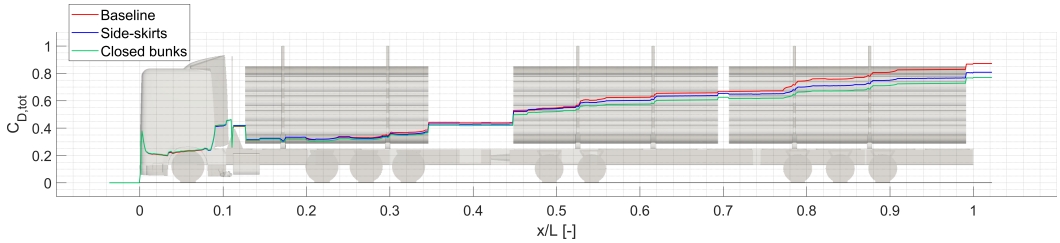

Figure 4.24: Drag coefficient build-up along the truck for closed bunks concept compared with the baseline model at 5 degrees yaw angle.

4.2.3 Increased height of skirts

As explained on the previous concept, removing the flow under the load reduces the aerodynamic drag of the truck. Hence, and increased height of the lateral walls of the skirts was implemented to prevent the flow from entering that region; expecting that this concept would improve the result obtained by just closing the space between the bunks on top of the frame. As shown on Fig. 4.25, the lateral surfaces of the side-skirts have been increased in height until the end of the bunks, with the exception of the boat-tail shape at the back that must keep the original height to not disturb the load position.

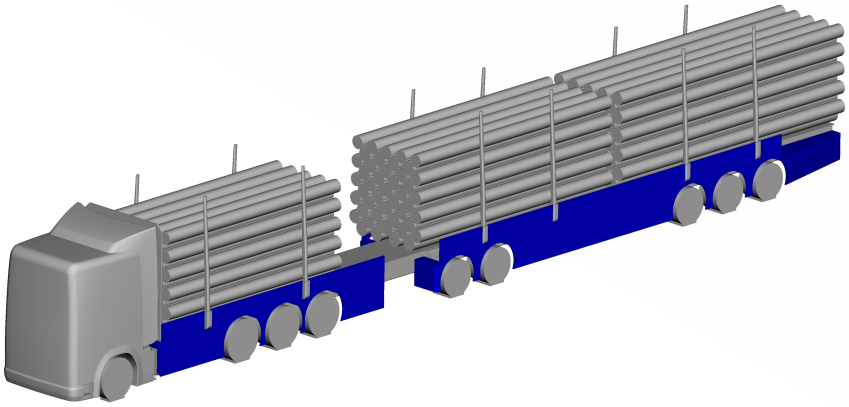

Figure 4.25: Increased height of the side-skirts aerodynamic concept added to the baseline model.

The result for this aerodynamic concept, Table 4.5, was a total drag coefficient of 0.685; that means a reduction of 23.1% with respect to the baseline model, and a further reduction of 17.5% with respect to the original skirts. Compared with the previous concept, that was aiming for affecting the same region, the skirts with increased height reduced the drag coefficient a 11% more than closing the space between the bunks.

Table 4.5: Drag coefficient results for the higher side-skirts aerodynamic concept compared with the baseline model, for 5 degrees yaw angle.

Model	C_D	% from baseline	% from skirts
Baseline	0.891	-	-
Side-skirts	0.830	-6.85	-
Higher side-skirts	0.685	-23.1	-17.5

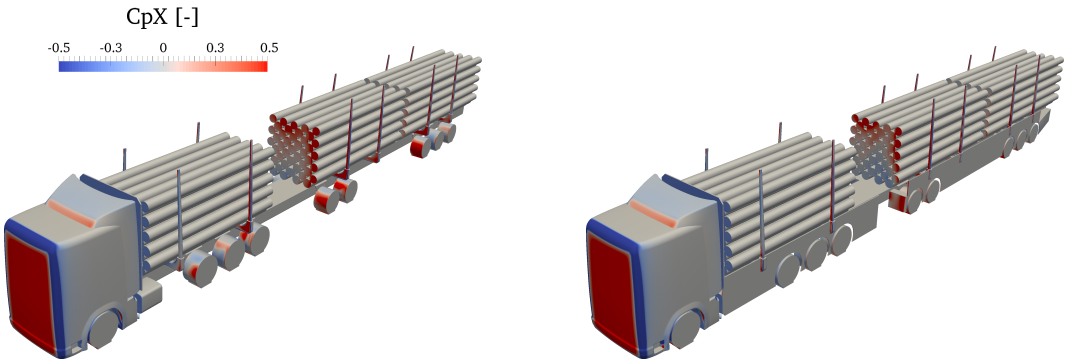

(a) **(b)**

Figure 4.26: Comparison of static pressure coefficient distribution between the baseline model (a) and the side-skirts aerodynamic concept (b). At 5 degree yaw angle.

As seen on the original skirts, the high pressure regions in front of each wheel is removed by the use of the skirts, Fig. 4.26, leaving only a high pressure region on

the surface after the gap. Furthermore, the increased height of the lateral wall of the skirts closes also the extreme sides of the bunks, therefore, the drag coming from that high pressure region seen in the baseline is also reduced by the implementation of this concept.

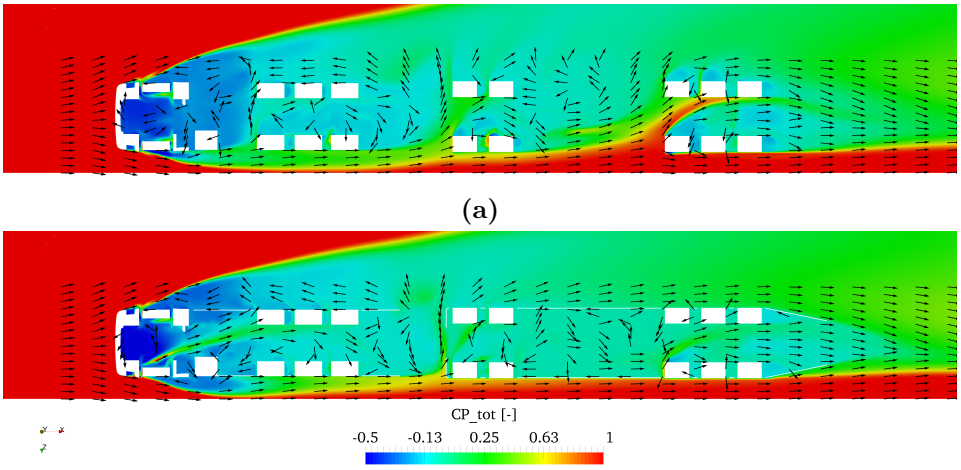

Figure 4.27: Comparison of total pressure coefficient on the underbody region (y=-0.39 m) between the baseline model (a) and the high side-skirts aerodynamic concept (b). At 5 degree yaw angle.

Regarding the underbody flow field, Fig. 4.27, the same effect obtained with the original skirts is present, shielding the space in between the wheels to prevent flow going on the leewards direction and creating high pressure regions on the wheels on that side.

As in the previous concept, the main objective of this concept was improving the flow under the load to reduce the drag coming from the bunks. If Fig. 4.28 is compared with Fig. 4.23, it can be noticed that shielding the bunks from their extreme sides is much more effective that closing the spacing between them. Now, the high pressure region has been removed all along the bunks span and the suction regions downstream of each pair has also disappeared.

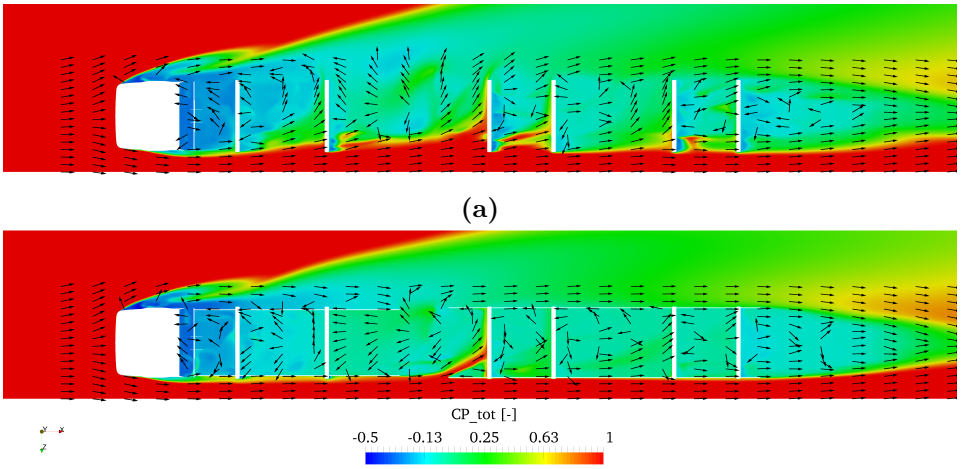

Figure 4.28: Comparison of total pressure coefficient on the underload region (y=0.34 m) between the baseline model (a) and the high side-skirts aerodynamic concept (b). At 5 degree yaw angle.

Finally, from the drag build up shown on Fig. 4.29 it can be noted that, with respect to the original side-skirts, increasing the height of them until the bunks improves the performnces from the gap until the end of the truck preventing flow to enter the region under second and third stack and reducing the drag at the position of each of the bunks.

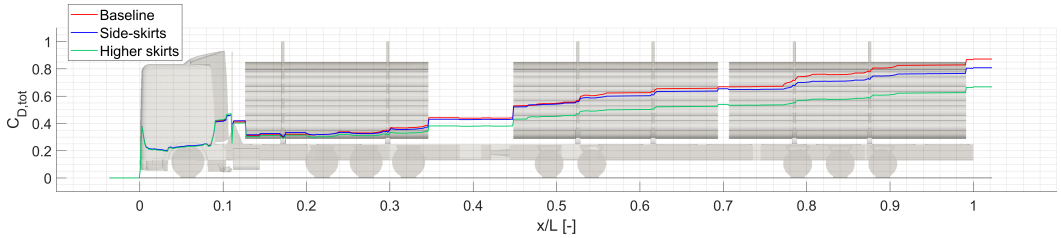

Figure 4.29: Drag coefficient build-up along the truck for higher side-skirts concept compared with the baseline model at 5 degrees yaw angle.

4.2.4 Bulkhead shield

It was seen on the baseline results that there was flow going through the first stack on the upstream direction and leaving the region between this stack and the bulkhead with a z-velocity that promoted the separation of the flow on the cabin. A shield was added as an aerodynamic concept to close the space between the bulkhead and the first pair of stakes as shown on Fig. 4.30.

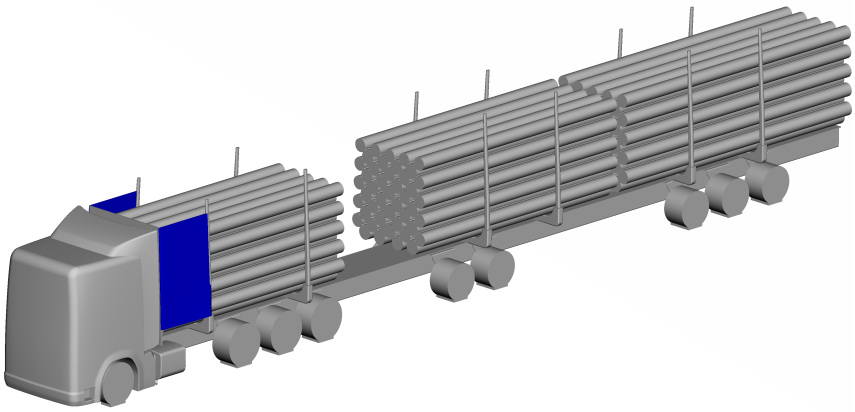

Figure 4.30: Bulkhead shield aerodynamic concept added to the baseline model, together with side-skirts.

Table 4.6: Drag coefficient results for the bulkhead shield aerodynamic concept compared with the baseline model, for 5 degrees yaw angle.

Model	C_D	% from baseline
Baseline	0.891	-
Bulkhead shield	0.805	-9.65

This concept improved the performance of the truck reducing its total drag coefficient to 0.805, that is a 9.65% reduction with respect to the baseline model, Table 4.6. As intended by closing that space, the separation after the cab is smaller, as indicated by the skin-friction coefficient shown on Fig. 4.31.

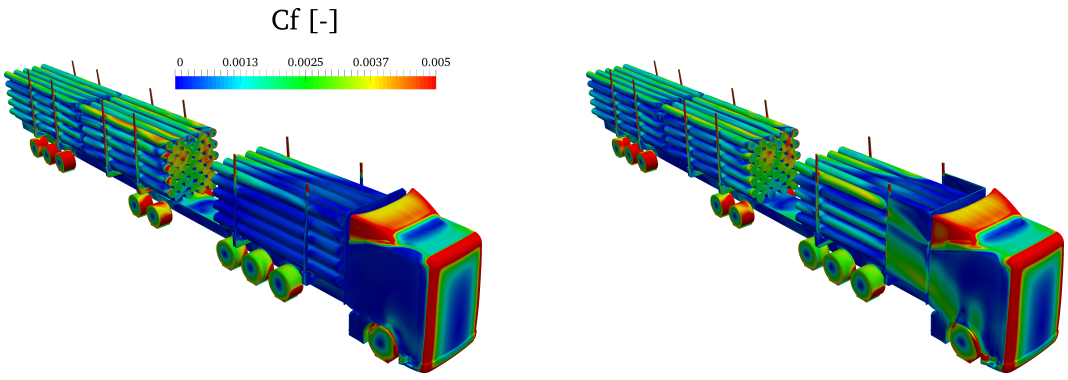

(a) **(b)**

Figure 4.31: Contour of skin friction coefficient. Baseline model (a), bulkhead shield concept (b). At 5 degree yaw angle.

This reduction of flow going on the leewards side of the truck from the bulkhead region, makes the wake on the right side of the truck smaller than the one present on the baseline case, Fig. 4.32.

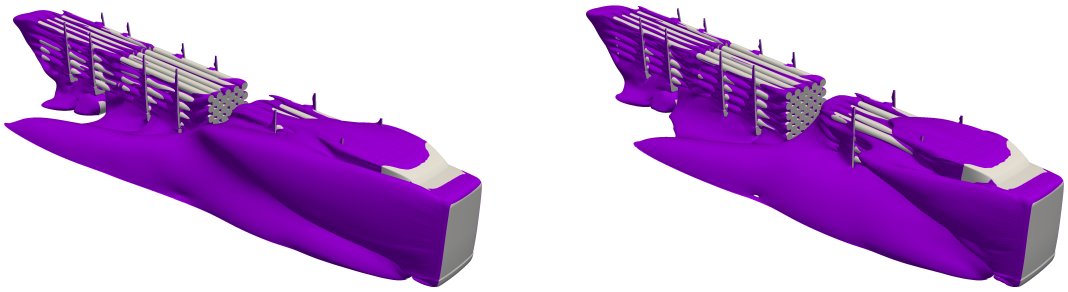

(a) (b)

Figure 4.32: Iso-surface of total pressure coefficient. Baseline model (a), bulkhead shield concept (b). At 5 degree yaw angle.

Furthermore, if the flow field on a plane cutting the bulkhead perpendicularly on the horizontal direction is analyzed, Fig. 4.33, it can be seen that the low pressure region on the leeward side is now narrower and shorter than on the baseline case, and how the flow in that region maintains a more uniform directions since it is not disturbed by flow going out from the first stack.

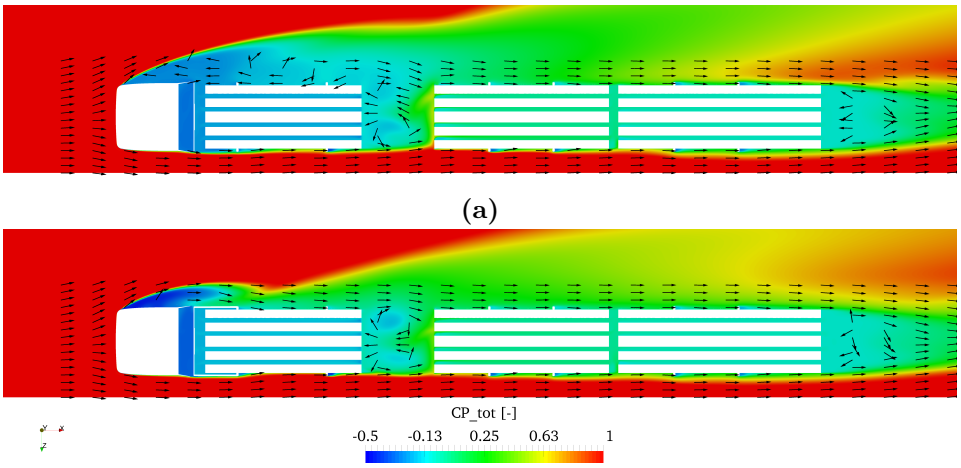

(a)

(b)

Figure 4.33: Comparison of total pressure coefficient at y=1.25 m between the baseline model (a) and the bulkhead shield aerodynamic concept (b). At 5 degree yaw angle.

The build up of the drag coefficient along the truck, Fig. 4.34, shows that the drag reduction obtained with this aerodynamic concept is focus just on the bulkhead region where the wake is reduced since the flow remains attached. Downstream of that region no significant effect is found since both drag coefficient follow the same trend until the end of the truck.

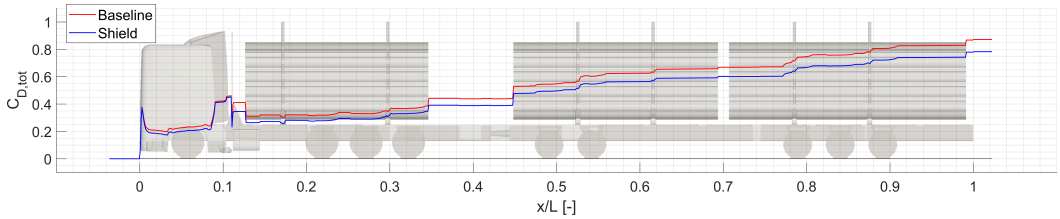

Figure 4.34: Drag coefficient build-up along the truck for bulkhead shield concept compared with the baseline model at 5 degrees yaw angle.

4.2.5 Closed stakes

Another part that contributes significantly to the total drag of the truck are the stakes holding the logs, mainly due to the high pressure on their front faces. Hence, in order to create a more streamlined shape on the lateral sides of the truck, the space between the stakes holding each stack was closed as shown on Fig. 4.35.

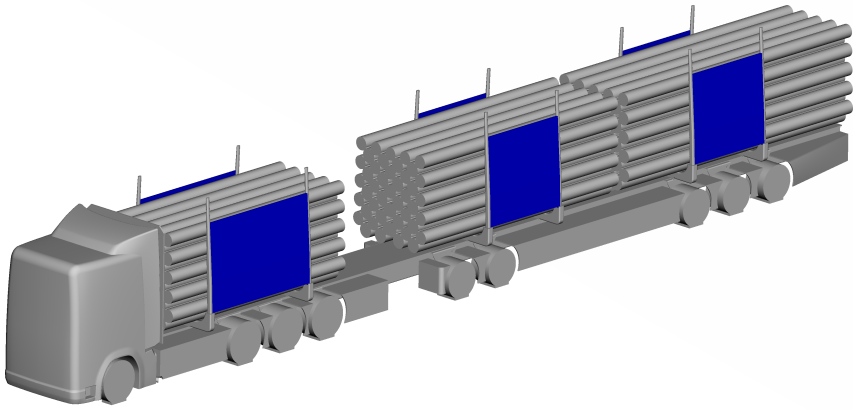

Figure 4.35: Closed stakes aerodynamic concept added to the baseline model, together with side-skirts.

The addition of these closing surfaces in between the stakes yielded a total drag coefficient of 0.853, together with the side-skirts. That is, closing the space between the stake in each stack increased the drag coefficient a 2.77% with respect to the model with just side-skirts implemented, Table 4.7.

Table 4.7: Drag coefficient results for the closed stakes aerodynamic concept compared with the baseline model, for 5 degrees yaw angle.

Model	C_D	% from baseline	% from skirts
Baseline	0.891	-	-
Side-skirts	0.830	-6.85	-
closed stakes	0.853	-4.26	+2.77

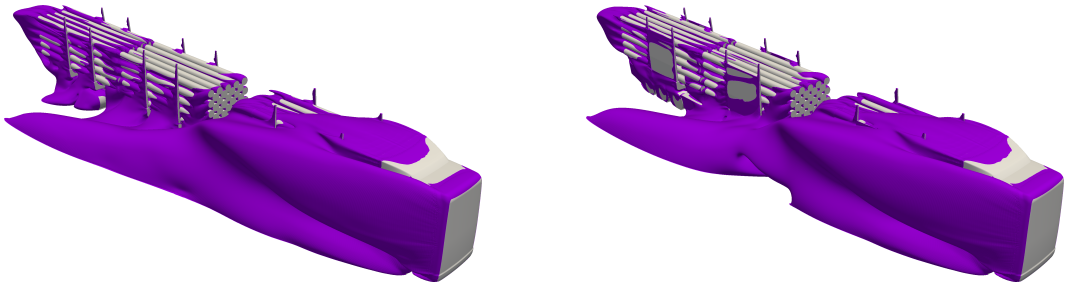

(a) (b)

Figure 4.36: Iso-surface of total pressure coefficient. Baseline model (a), closed stakes concept (b). At 5 degree yaw angle.

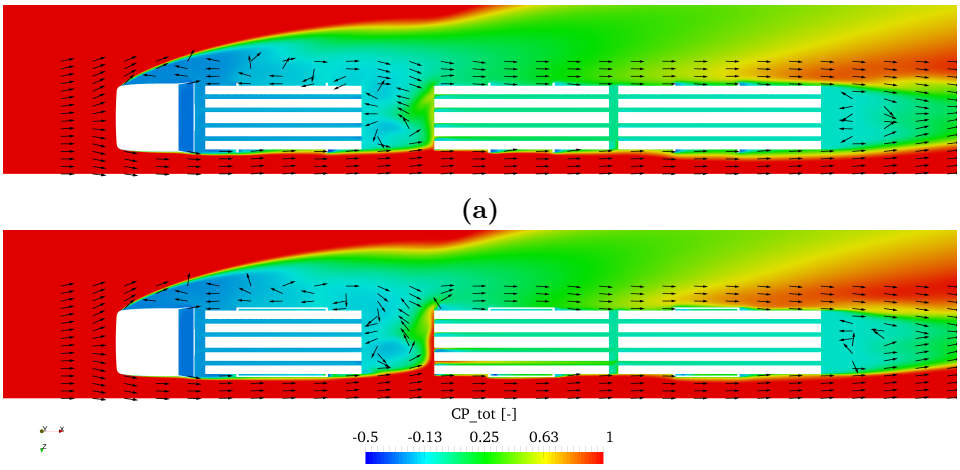

(a)

(b)

Figure 4.37: Comparison of total pressure coefficient at y=1.25 m between the baseline model (a) and the closed stakes aerodynamic concept (b). At 5 degree yaw angle.

The fact that the space between the first stack and the bulkhead is not closed by this concept, causes that the separation is still present on the right edge of the cabin, Fig. 4.36 and 4.37, and the drag at that location is the same as in the baseline model, Fig. 4.39, unlike on the bulkhead shield concept. Since this separation is a major contributor to the total drag, the aerodynamic concept consisting of closing just the space between the stakes did not show a improvement on the performance.

Flow field differences on the gap region are also created when adding this aerodynamic concept; as seen on Fig. 4.37 and 4.38 the high pressure region on the front face of the second stakes is larger than in the baseline model, this explains the increased of drag at that location shown on the drag build up on Fig. 4.39. Since the gap is one of the major contributors to the total drag of the truck, an increase in this region is not positive for the overall performance.

An improvement of the flow field created by this concept, although not enough for an overall decrease of drag when compared with the side-skirts model, is found on the stakes on the windward side of the truck. The closing between the stakes holding each stack maintains the flow attached to this surfaces, reducing the suction region

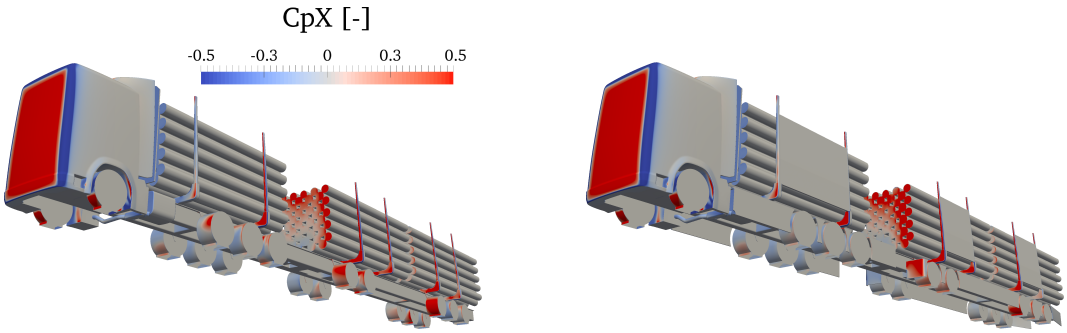

(a) (b)

Figure 4.38: Contour of static pressure coefficient, front view. Baseline model (a), closed stakes concept (b). At 5 degree yaw angle.

behind each stake present on the baseline model, Fig. 4.37. This effect is more noticeable on the third stake as seen on the drag build up, Fig. 4.39, where the drag coefficient of this concept increases less than for the baseline or the side-skirts models.

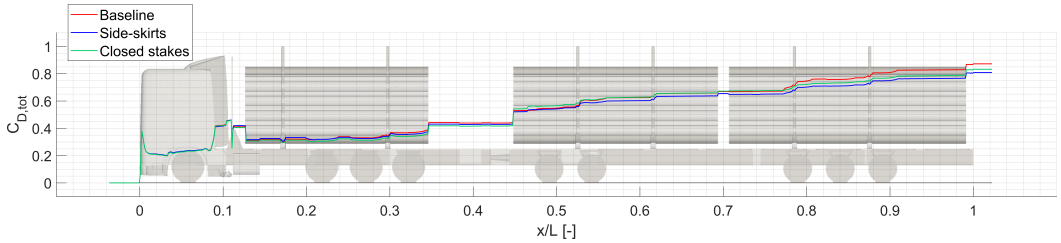

Figure 4.39: Drag coefficient build-up along the truck for closed stakes concept compared with the baseline model at 5 degrees yaw angle.

4.2.6 Full lateral cover

Since closing just the space in between each pair of stakes did not improve the total performance of the truck, but the use of a shield closing from the bulkhead to the first stake did; a prolongation of the shield all along the lateral sides of the truck was implemented, Fig. 4.40, to get a more streamline shape on the lateral and remove the separation of the flow after each pair of stakes shown on Fig.4.36.

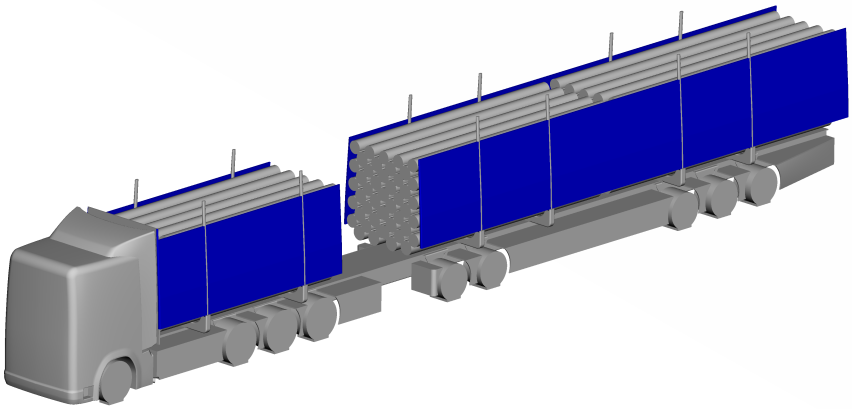

Figure 4.40: Full lateral cover aerodynamic concept added to the baseline model, together with side-skirts.

This aerodynamic concept did improve further the performance of the side-skirts, reaching a 0.727 value of total drag coefficient, Table 4.8, meaning a 18.4% reduction with respect to the baseline and 12.4% with respect to the model with only side-skirts added.

Table 4.8: Drag coefficient results for the full lateral cover aerodynamic concept compared with the baseline model, for 5 degrees yaw angle.

Model	C_D	% from baseline	% from skirts
Baseline	0.891	-	-
Side-skirts	0.830	-6.85	-
Full lateral cover	0.727	-18.4	-12.4

The skin-friction coefficient shown on Fig. 4.41, shows that the flow is attached in almost the whole lateral cover on the leewards side after the gap, which was not the case on the baseline model.

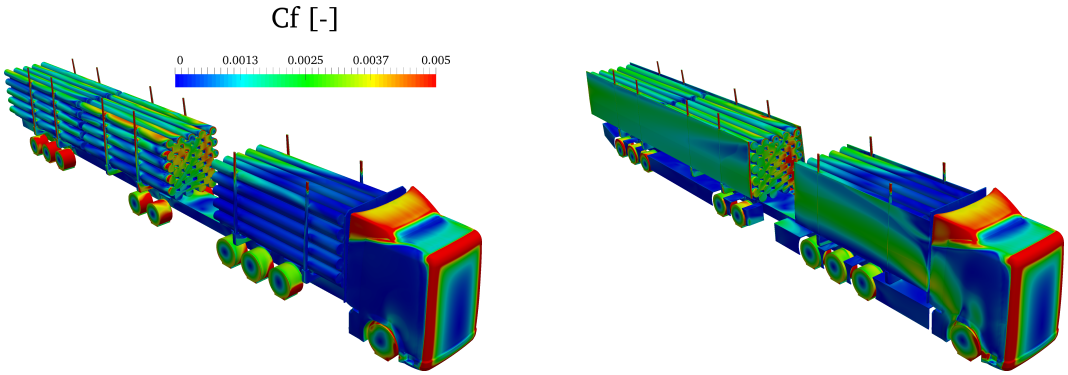

(a) (b)

Figure 4.41: Contour of skin friction coefficient. Baseline model (a), full lateral cover concept (b). At 5 degree yaw angle.

Adding the lateral cover all along the truck removes the high pressure regions on the front faces of the stakes, Fig. 4.42, and the suction regions on the back of them, Fig. 4.43, therefore the contribution of the stakes to the total drag of the truck is reduced.

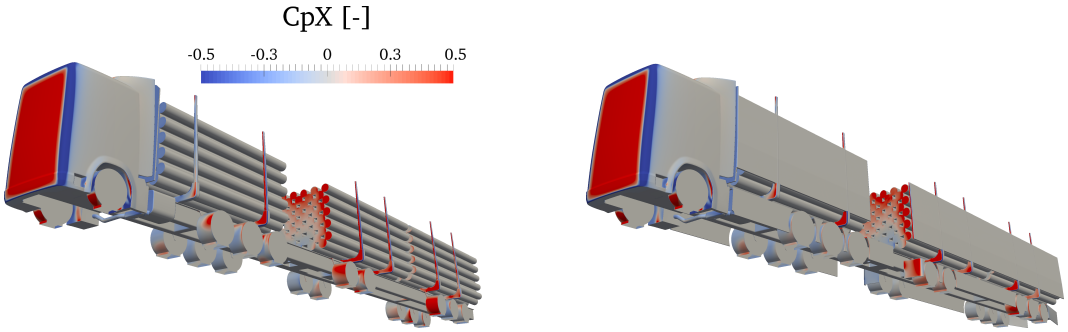

(a) (b)

Figure 4.42: Contour of static pressure coefficient, front view. Baseline model (a), full lateral cover concept (b). At 5 degree yaw angle.

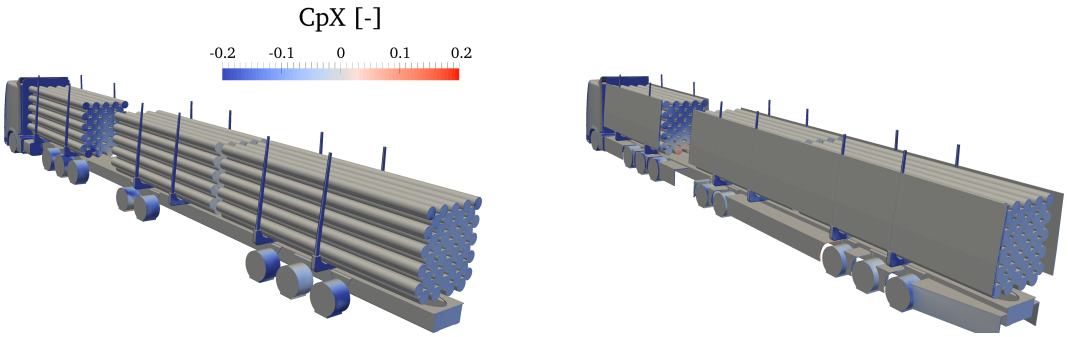

(a) (b)

Figure 4.43: Contour of static pressure coefficient, back view. Baseline model (a), full lateral cover concept (b). At 5 degree yaw angle.

Finally, the iso-surface of total pressure coefficient on Fig. 4.44 shows that the wake on the leeward side has been reduced by the addition of the side-skirts and the

lateral cover, that reduced the separation on the right edge of the cabin. Moreover, the lateral cover prevents the stakes from facing the freestream flow directly and therefore the separation that can be seen for the baseline model after every stake on the back part of the truck is now removed.

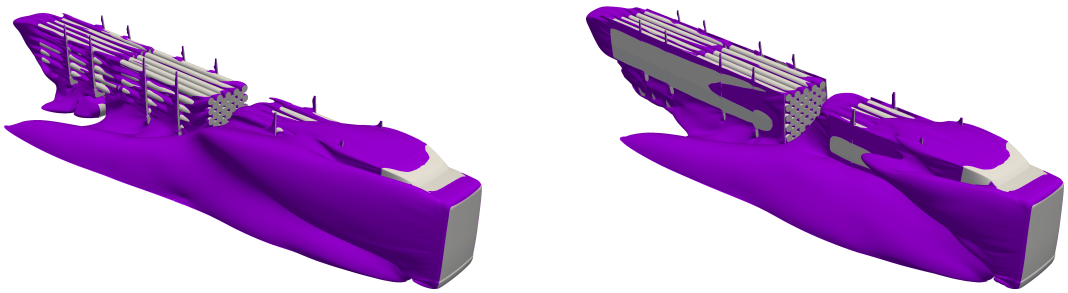

(a) (b)

Figure 4.44: Iso-surface of total pressure coefficient. Baseline model (a), full lateral cover concept (b). At 5 degree yaw angle.

All the effect of the lateral cover can be seen on the drag build up shown on Fig. 4.45. The main reduction occurs on the bulkhead region and is caused by the change of the separation behavior on the leeward side on the cabin. After that the drag follows a similar tendency than the other two cases shown on Fig. 4.45, with puntual improvements in each of the stakes and bunks locations.

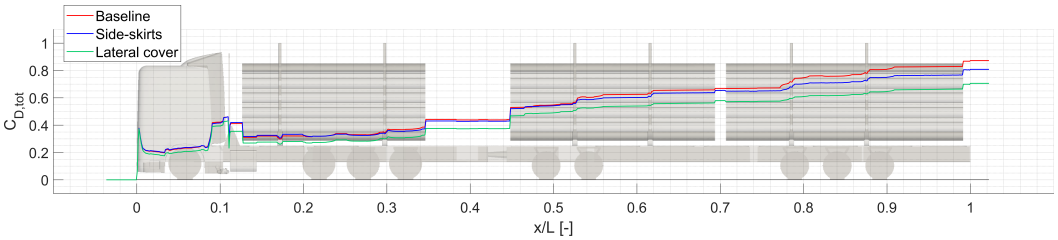

Figure 4.45: Drag coefficient build-up along the truck for full lateral cover concept compared with the baseline model at 5 degrees yaw angle.

4.2.7 Boat-tail

A boat-tail is one of the most common solutions for drag reduction used on trailer vehicles, a lateral version of a boat-tail, Fig. 4.46, has been implemented on the fully-loaded timber truck as a prolongation of the lateral cover for 500 millimeters, limit of the current regulation, and with a 12 degrees angle towards the symmetry plane of the truck, a common value used on trucks [22].

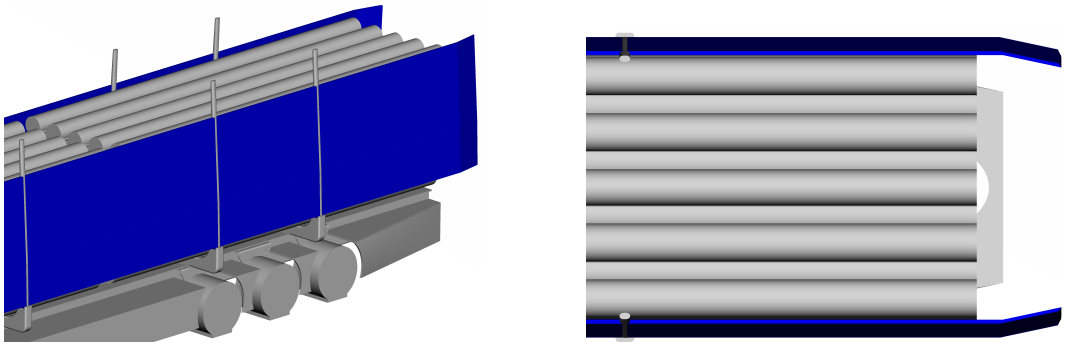

(a) (b)

Figure 4.46: Boat-tail aerodynamic concept added to the full lateral cover and the side-skirts.

This concept was added together with the side-skirts and resulted on a total drag coefficient of 0.720, that is, 19.2% reduction with respect to the baseline model. As shown on Table 4.9 the improvement gained with the addition of the boat-tail to the full lateral cover is almost non-existing, this is because the main effect of both concepts is on the cab-bulkhead region and not on the back of the truck as shown by the drag build up results on Fig. 4.49.

Table 4.9: Drag coefficient results for the boat-tail aerodynamic concept compared with previous concepts, for 5 degrees yaw angle.

Model	C_D	% from baseline	% from skirts	% from full cover
Baseline	0.891	-	-	-
Side-skirts	0.830	-6.85	-	-
Full lateral cover	0.727	-18.4	-12.4	-
Boat-tail	0.720	-19.2	-13.25	-0.96

The further reduction of drag from the side-skirt concept comes from the modified wake on the back by the boat-tail. Fig. 4.47 and Fig. 4.48 show that the wake is both narrower and shorter at the back of the truck, reducing the suction region and hence the drag force on the back face of the truck.

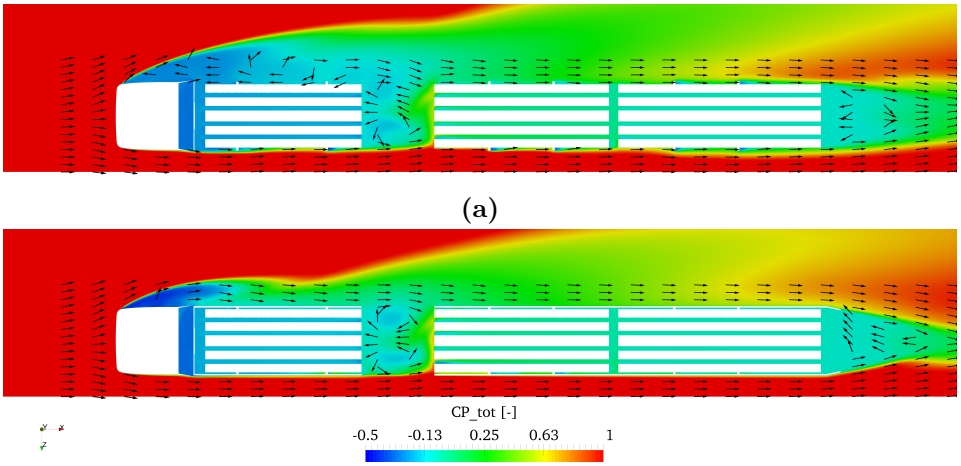

(a)

(b)

Figure 4.47: Comparison of total pressure coefficient at y=1.25 m between the baseline model (a) and the boat-tail aerodynamic concept (b). At 5 degree yaw angle.

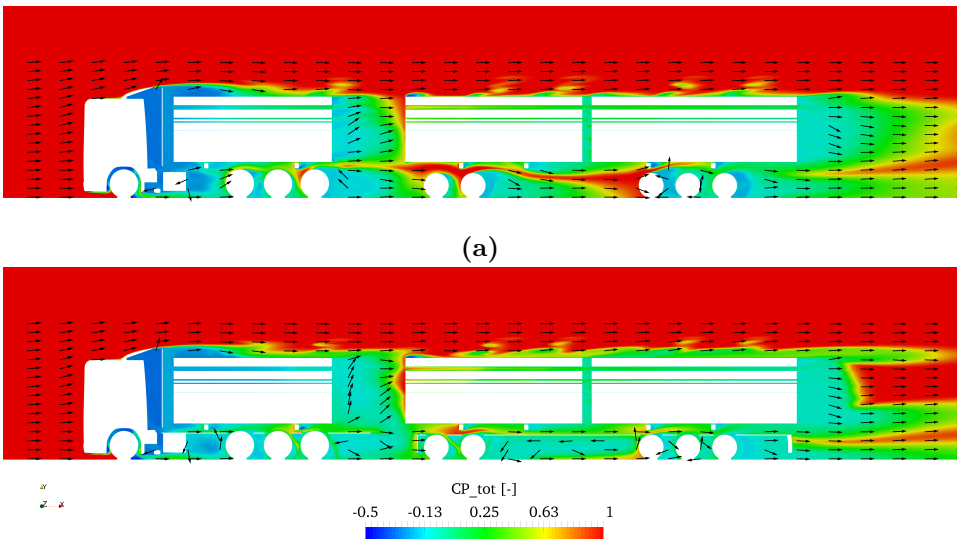

(a)

(b)

Figure 4.48: Comparison of total pressure coefficient at z=0.88 m between the baseline model (a) and the boat-tail aerodynamic concept (b). At 5 degree yaw angle.

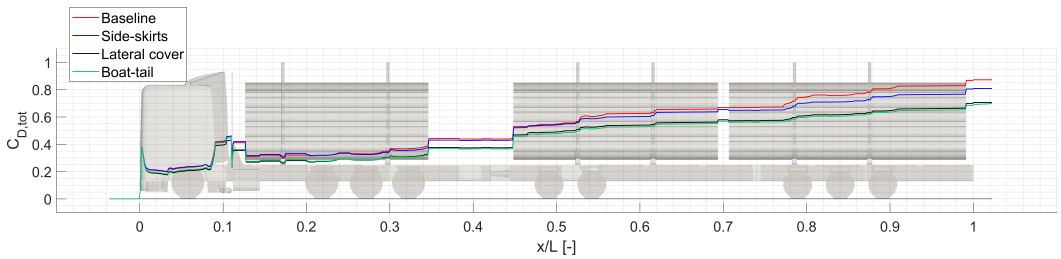

Figure 4.49: Drag coefficient build-up along the truck for boat-tail concept compared with the baseline model at 5 degrees yaw angle.

4.2.8 Gap spoiler

The gap between the first and second stack is one of the most important flow regions for the total drag value of the truck, especially the front face of the second stack where the flow hits creating a high pressure region. Hence, to reduce the amount of flow on that region a gap spoiler was added by prolonging the lateral cover of the first stack 500 millimeters more and with a 12 degrees outwards angle, Fig. 4.50, making the truck 68 millimeters wider.

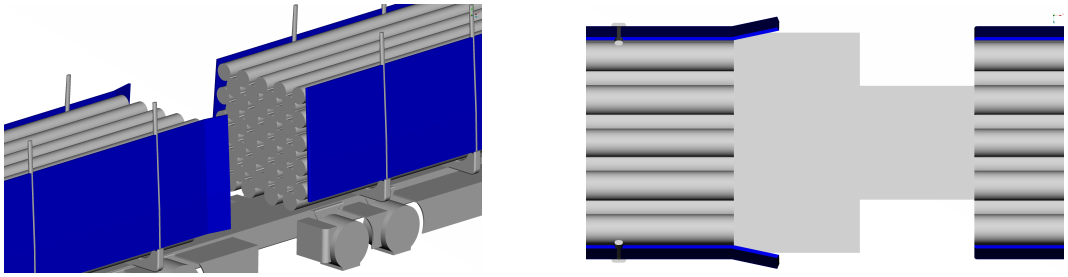

(a) (b)

Figure 4.50: Gap spoiler aerodynamic concept added to the full lateral cover and the side-skirts.

This aerodynamic concept showed a good performance yielding a drag coefficient of 0.609, together with the side-skirts, for a reduction of 31.6% with respect to the baseline model. Table 4.10 shows a comparison with other previous concepts implemented.

Table 4.10: Drag coefficient results for the gap spoiler aerodynamic concept compared with previous concepts, for 5 degrees yaw angle.

Model	C_D	% from baseline	% from skirts	% from full cover
Baseline	0.891	-	-	-
Side-skirts	0.830	-6.85	-	-
Full lateral cover	0.727	-18.4	-12.4	-
Gap spoiler	0.609	-31.6	-26.6	-16.2

Part of this reduction comes from the front face of the second stack, the deflection of the flow outwards prevents the flow from entering the gap region, Fig. 4.51; and, therefore, the region of high pressure on that face is reduced compared with the baseline case, Fig. 4.52.

Another big influence of the gap spoiler was found on the leewards side of the cabin, which seemed to be a very sensitive region of the flow. As seen on Fig. 4.53, the separation on the cabin and the wake on the leewards side, already reduced with the addition of the lateral cover, completely disappeared when using the gap spoiler, the modification of the flow on the gap could also affect upstream resulting on a more uniform flow field on the right side of the truck and removing the low pressure region that was generating drag there.

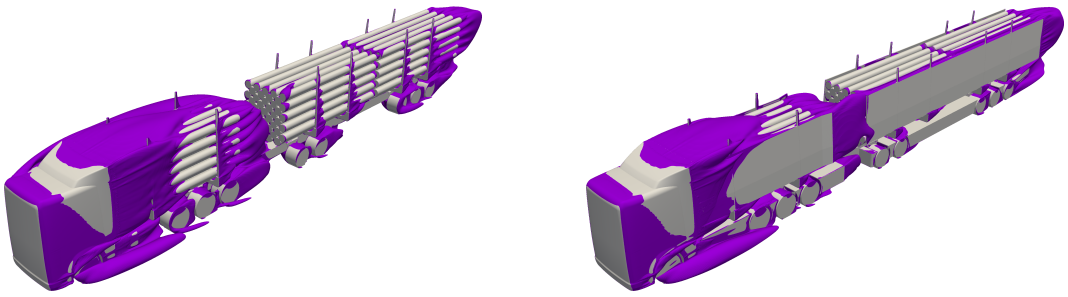

(a) (b)

Figure 4.51: Iso-surface of total pressure coefficient. Baseline model (a), gap spoiler concept (b). At 5 degree yaw angle.

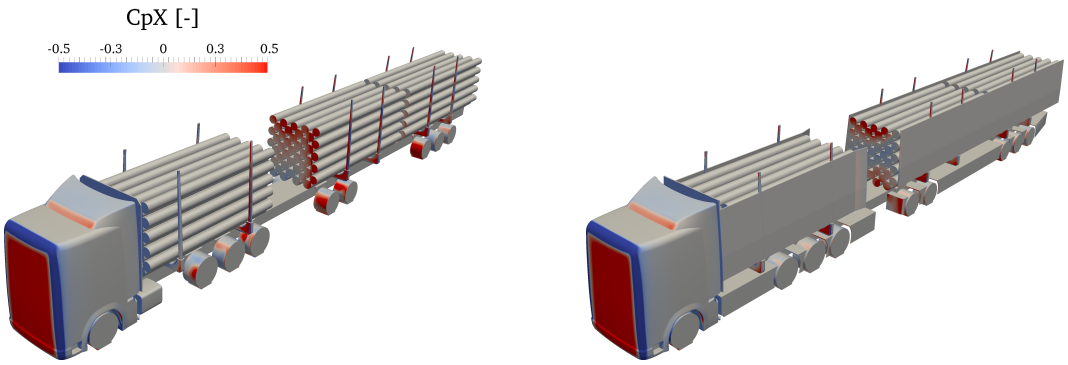

(a) (b)

Figure 4.52: Contour of static pressure coefficient, front view. Baseline model (a), gap spoiler concept (b). At 5 degree yaw angle.

The drag coefficient build up along the truck, Fig. 4.54, shows two main regions of influence of the gap spoiler in comparison with the lateral cover and the side-skirts. As said before the separation wake on the leeward side is removed when using the gap spoiler, therefore the drag in the bulkhead region is considerably lower than for the other concepts. Moreover, the wake after the first stack does not enter the gap region, Fig. 4.51, which clearly reduces the drag on the front face of the second stack, as indicated by the smaller increase on Fig. 4.54.

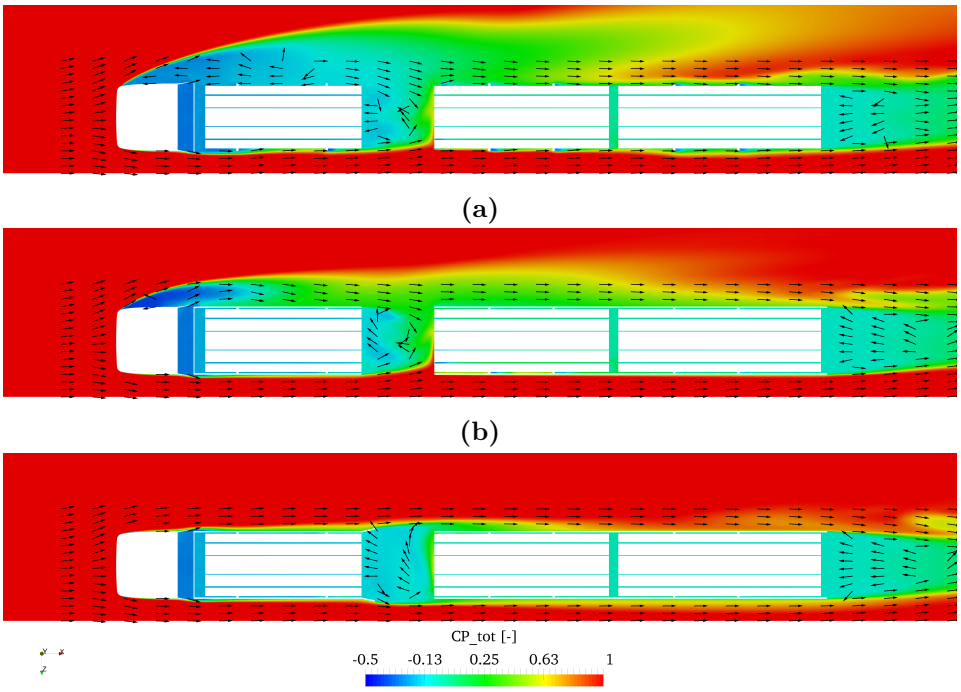

Figure 4.53: Comparison of total pressure coefficient at y=1.8m between the baseline model (a), full lateral cover concept (b) and the gap spoiler aerodynamic concept (c). At 5 degree yaw angle.

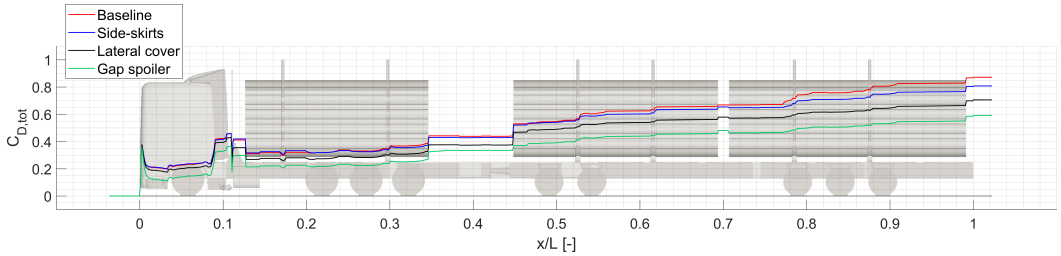

Figure 4.54: Drag coefficient build-up along the truck for gap spoiler concept compared with the baseline model at 5 degrees yaw angle.

4.2.9 Gap fairing

Other possibility to improve the flow field on the gap region is by modifying the front face of the second stack, instead of the back of the first as done with the gap spoiler. For this a gap fairing was added as shown on Fig. 4.55, with a shape that intends to deflect the flow outwards on the gap and to the bottom of the truck, so combined with the side-skirts it can improve the global flow field both in the gap and the underbody regions.

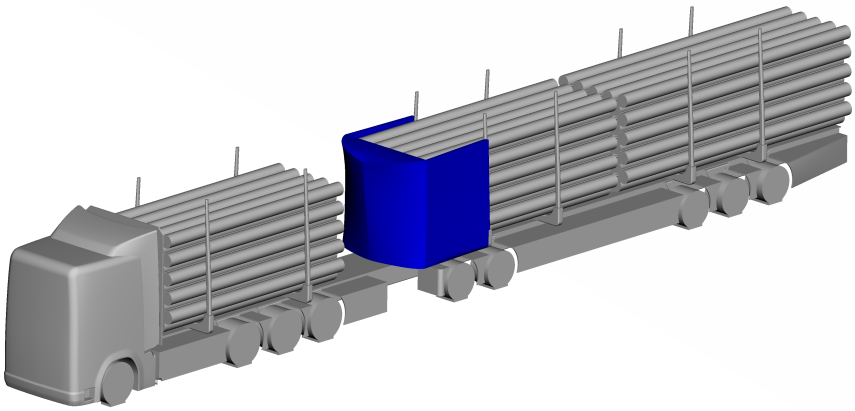

Figure 4.55: Gap fairing aerodynamic concept added to the baseline model, together with side-skirts.

Table 4.11: Drag coefficient results for the gap fairing aerodynamic concept compared with previous concepts, for 5 degrees yaw angle.

Model	C_D	% from baseline	% from skirts
Baseline	0.891	-	-
Side-skirts	0.830	-6.85	-
Gap fairing	0.738	-17.2	-11.1

The results for this concept, Table 4.11, gave a total drag coefficient of 0.738, that is a reduction of 17.2% with respect to the baseline model and a 11.1% with respect to the side-skirts model.

The addition of these surfaces on the front face of the second stack modified the flow field on the gap region as shown on Fig. 4.56; this new flow field in the gap improves the global performance of the truck since the high pressure region on the front face is reduced and a suction region is now present on the front of the faring, pushing the truck forwards, Fig. 4.57.

As seen with the gap spoiler, the wake on the leewards side of the truck, Fig. 4.58, is also improved with the addition of the fairing since the separation on the cabin is reduced.

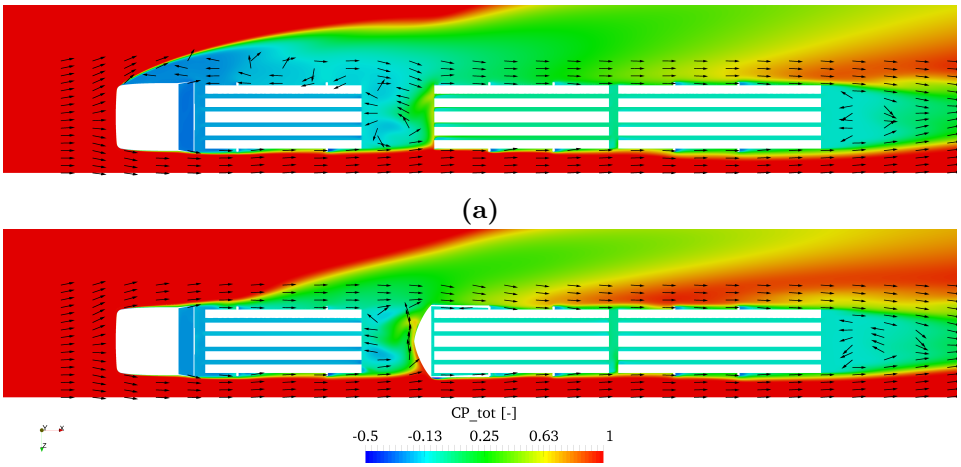

(a)

(b)

Figure 4.56: Comparison of total pressure coefficient at y=1.25 m between the baseline model (a) and the gap fairing aerodynamic concept (b). At 5 degree yaw angle.

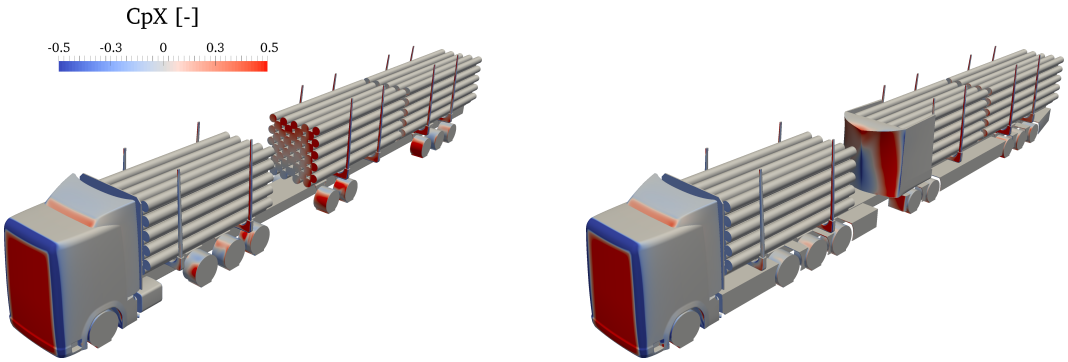

(a) (b)

Figure 4.57: Contour of static pressure coefficient, front view. Baseline model (a), gap fairing concept (b). At 5 degree yaw angle.

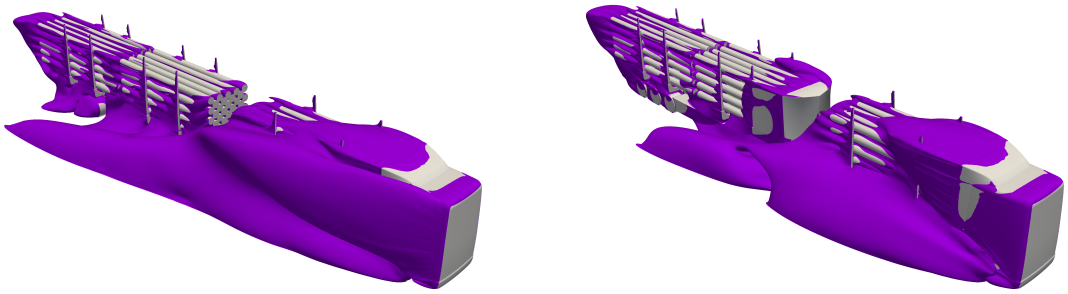

(a) (b)

Figure 4.58: Iso-surface of total pressure coefficient. Baseline model (a), gap fairing concept (b). At 5 degree yaw angle.

This effect is also seen on Fig. 4.59, where the low pressure regions on the right side of the truck are reduced. However, if compared with the gap spoiler, Fig. 4.53, it can be notice that a low pressure region is present in this case on the back right side of the truck, which was not the case when using the gap spoiler. Therefore, out of this two concept with a similar aim, it can be said that the modification of the first face of the gap by adding a gap spoiler is more effective that the addition of the fairing on the second face of the gap.

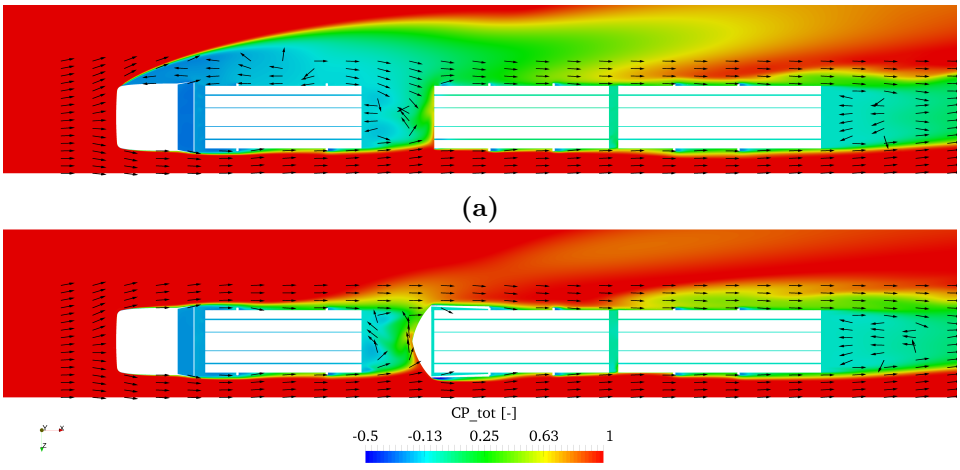

(a)

(b)

Figure 4.59: Comparison of total pressure coefficient at y=1.8 m between the baseline model (a) and the gap fairing aerodynamic concept (b). At 5 degree yaw angle.

Fig. 4.60 shows the decrease of drag on the cab region due to the smaller separation on the leeward side, and also the change of flow field on the gap region. With the addition of the fairing a larger increase of drag occurs upstream of the second stack, however the overall performance in that region is positive and the drag coefficient is lower for the gap fairing concept, following the same tendency as the baseline from the second stack until the end of the truck.

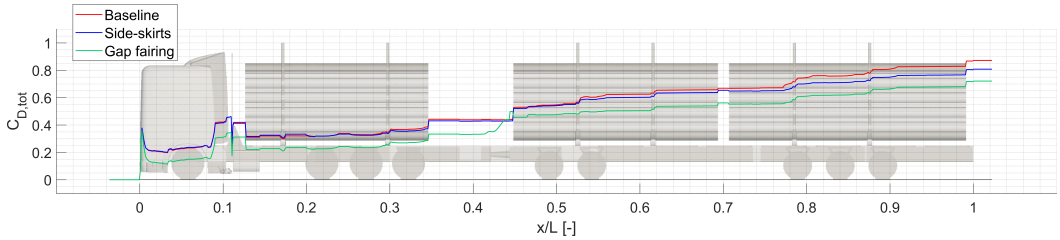

Figure 4.60: Drag coefficient build-up along the truck for gap fairing concept compared with the baseline model at 5 degrees yaw angle.

4.2.10 Closed gap

A supposedly ideal situation for the truck performance in terms of drag would be to not have any gap in the middle of the load, as seen in [6] where wind tunnel measurements led to a drag decrease of approximately 21% with a similar concept for a 5 degree yaw angle condition; since this would remove the high pressure on the second stack and the suction on the first, which are two of the main contributors to the total drag coefficient of the baseline model as indicated on Fig. 4.12. To investigate this possibility a squared body was created and fitted on the space between first and second stacks, as shown on Fig. 4.61.

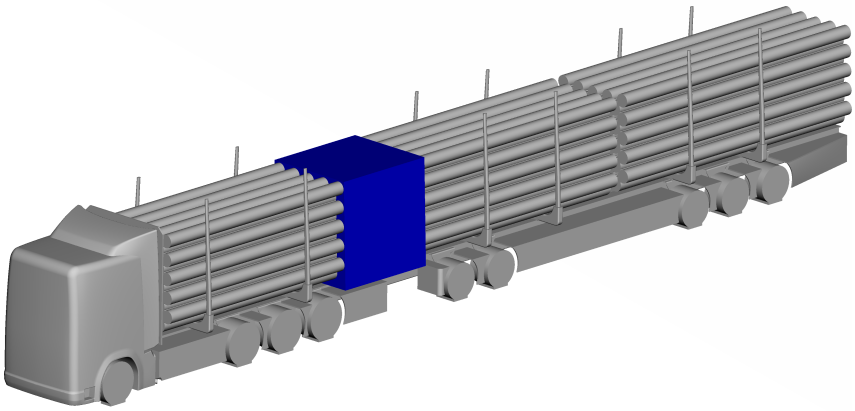

Figure 4.61: Completely closed gap aerodynamic concept added to the baseline model, together with side-skirts.

Results for this aerodynamic concept, and comparison with previous model, are shown on Table 4.12.

Table 4.12: Drag coefficient results for the closed gap aerodynamic concept compared with previous concepts, for 5 degrees yaw angle.

Model	C_D	% from baseline	% from skirts
Baseline	0.891	-	-
Side-skirts	0.830	-6.85	-
Closed gap	0.653	-26.7	-21.3

Fig. 4.62 shows that the whole high pressure region on the front face of the second stack is now removed, creating a great improvement in terms of drag reduction on that region.

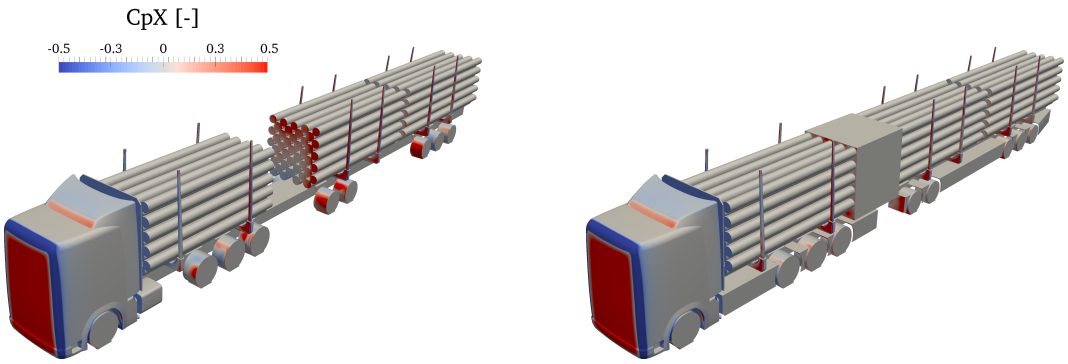

(a) **(b)**

Figure 4.62: Contour of static pressure coefficient, front view. Baseline model (a), closed gap concept (b). At 5 degree yaw angle.

However, overall the drag reduction obtained by completely closing the gap was a 26.7% with respect to the baseline model; that means that closing the gap did not show such a good performance as the addition of the gap spoiler (31.6% reduction). This difference comes again for the sensitivity to separation on the right edge of the cabin, when using the gap spoiler that separation was removed, however as seen on Fig. 4.63 the wake on the leewards side is still present, although reduced compared with the baseline, on the completely closed gap aerodynamic concept.

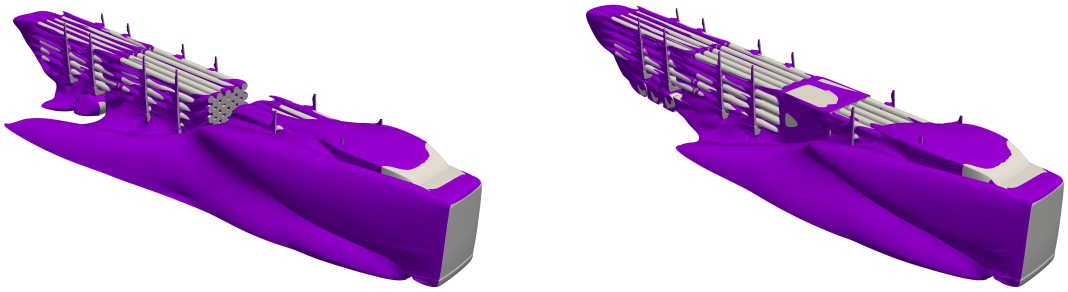

(a) **(b)**

Figure 4.63: Iso-surface of total pressure coefficient. Baseline model (a), closed gap concept (b). At 5 degree yaw angle.

From the drag coefficient build up, Fig. 4.64, it can be noted that no significant improvement is obtained by this concept before the gap region since, as said before, the separation wake on the leeward side is not removed and that is the main source on drag in the front part of the truck. However, closing the gap completely improves the performance in that region decreasing the drag in both the back of the first stack and the front of the second, compared with models without modification in the gap region.

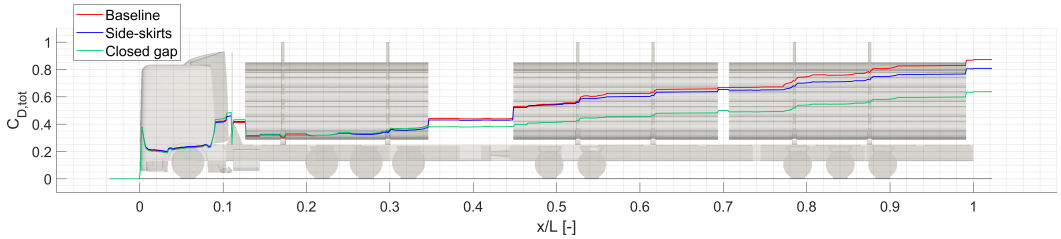

Figure 4.64: Drag coefficient build-up along the truck for closed gap concept compared with the baseline model at 5 degrees yaw angle.

4.2.11 Summary of concepts

A summary of all the drag coefficient values obtained with the concepts explained above is shown on Fig. 4.65. Table 4.13 indicates also the reduction compared with the baseline model and with the side-skirts and full lateral cover concept, for the combine concepts cases.

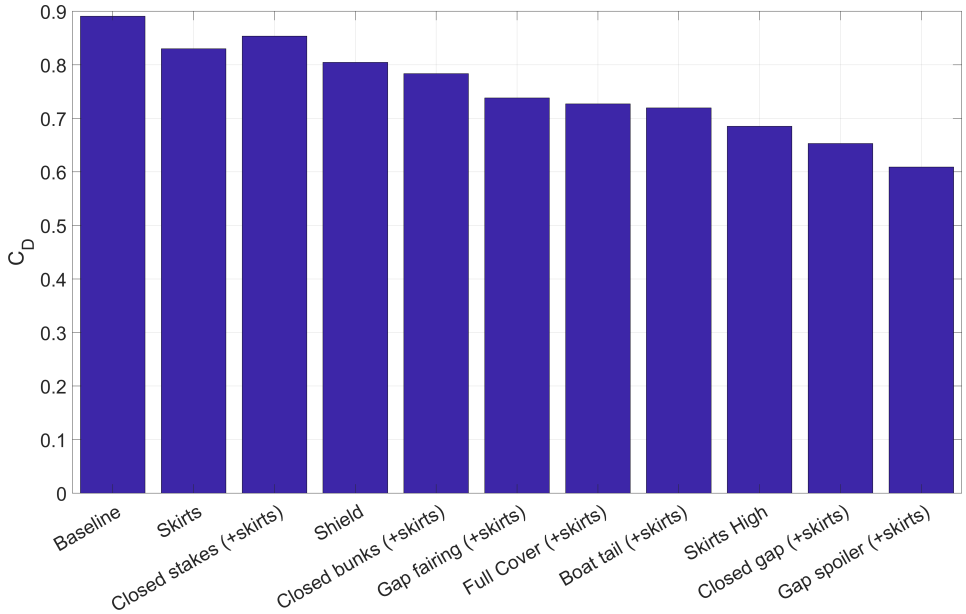

Figure 4.65: Drag coefficient value for the different concepts studied, compared with the baseline for a 5 degree yaw angle.

From the results on Fig. 4.65 and Table 4.13 it can be seen how there is at least one concept focused on each of the regions of large contribution to the total drag explained on the baseline results on Sec. 4.1.2. That is, the side-skirts reduced the drag a 6.85% by improving the flow on the underbody region and reducing the drag coming from the wheels; the increased of height of those side-skirts, to modify the flow field under the stacks, created a further drag decrease of 17.5% with respect to the original skirts thanks to the reduction of the drag generated by the bunks. The addition of the full lateral cover, enclosing the stakes inside and preventing them from facing the bulk flow directly, also led to an important drag reduction of 12.4% from the side-skirts mainly caused by the reduction of separation on the leeward side of the cabin caused by closing the outflow on the bulkhead region. Finally, all

Table 4.13: Summary of the aerodynamic concepts and comparison with baseline model and previous concepts, for a 5 degree yaw angle.

Model	C_D	% from baseline	% from skirts	% from full cover
Baseline	0.891	-	-	-
Skirts	0.830	-6.85	-	-
Closed stakes (+skirts)	0.853	-4.26	+2.77	-
Shield	0.805	-9.65	-	-
Closed bunks (+skirts)	0.784	-12	-5.54	-
Gap fairing (+skirts)	0.738	-17.2	-11.1	-
Full cover (+skirts)	0.727	-18.4	-12.4	-
Boat-tail (+skirts)	0.720	-19.2	-13.25	-0.96
Skirts high	0.685	-23.1	-17.5	-
Closed gap (+skirts)	0.653	-26.7	-21.3	-
Gap spoiler (+skirts)	0.609	-31.6	-26.6	-16.2

the concepts design with the aim of reducing the drag on the gap region gave good results, being the gap spoiler the one with the best performance with a 31.6% total reduction and a 16.2% with respect to the full cover and side-skirts aerodynamic concept.

Hence, it can be said that modifying the flow in the gap is the most effective way of reducing the total drag of the truck, however it must be taken into account that some of this reduction (for example on the gap spoiler) came from the sensitiveness of the separation behavior on the cabin and not just by a flow field change on the gap region. Moreover, as said before, there are concepts performing well in different regions of the truck, this gives the possibility of studying combinations aiming for a larger total drag reduction as shown on the following section.

4.3 Aerodynamic concepts combinations

Different combination of the concepts analyzed on the previous subsections were studied, to create these combinations the best concepts for each region of interest were chosen and combine together, for example, the skirts for the underbody, the increase height of the skirts for the bunks region or the gap spoiler to improve the flow on the gap. Hence, the following combinations were studied:

- Comb. 1: Increased height of skirts, gap spoiler, boat-tail and gap fairing.
- Comb. 2: Increased height of skirts, gap spoiler, boat-tail.

Some other combinations with the original skirts or with the bunks closed instead of the skirts with increased height were also run, but did not improve the performance more than using the gap spoiler and the original skirts alone, hence they were discarded for further analysis.

4.3.1 Combination 1

The combined use of skirts with increased height, gap spoiler, boat-tail and gap fairing, as shown on Fig. 4.66, improved the overall performance of the truck by reducing its total drag coefficient to 0.532, that is a reduction of 40.3% with respect to the baseline model, Table 4.14.

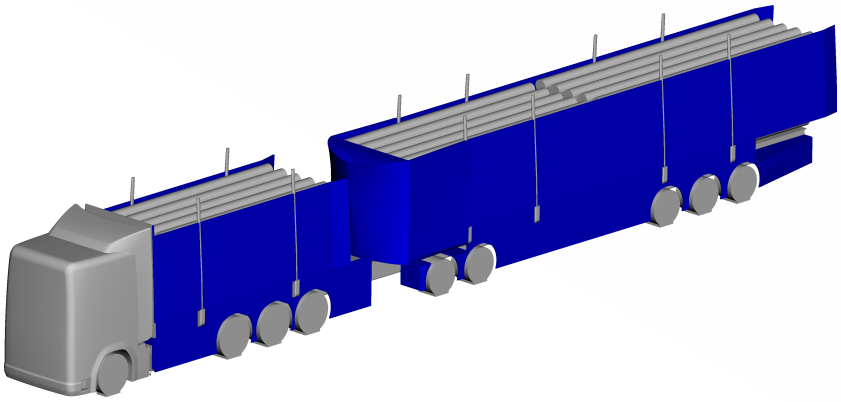

Figure 4.66: Geometry of the aerodynamic concepts combination 1.

From the iso-surfaces of total pressure coefficient it can be seen that the combinations of these concepts modify the wake on both the windward and leeward sides. On the windward side, Fig. 4.67, the spoiler and the fairing acting together on the gap prevented more flow from entering the gap, deflecting it outwards on the spoiler so it was directly to the lateral part of the fairing and then around the second stack; this clearly reduced the high pressure on the front face of the second stack, Fig.

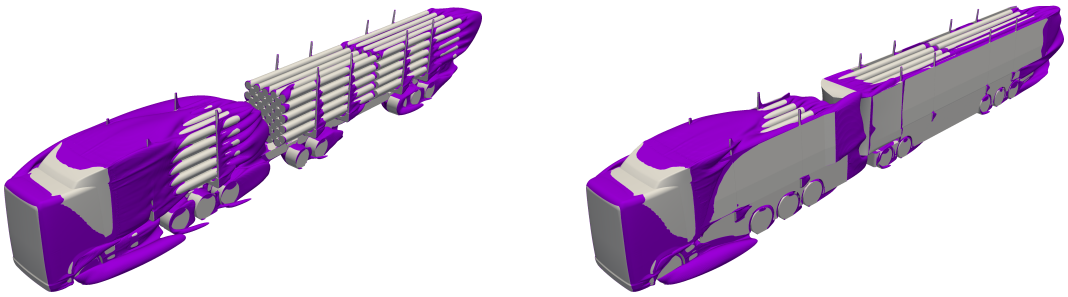

(a) (b)

Figure 4.67: Iso-surface of total pressure coefficient, windward side. Baseline model (a), combination 1 (b). At 5 degree yaw angle.

4.69, and created a suction region on the fairing surface reducing the total drag of the track.

Regarding the leeward side, Fig. 4.68, it can be noted that the wake has been reduced by the combination of the concepts; this is especially clear in the underbody region where the use of skirts reduce the drag coming from the wheels as explained in Sec. 4.2. But also the separation wake created on the cabin has been reduced by modifying the flow downstream with the concepts.

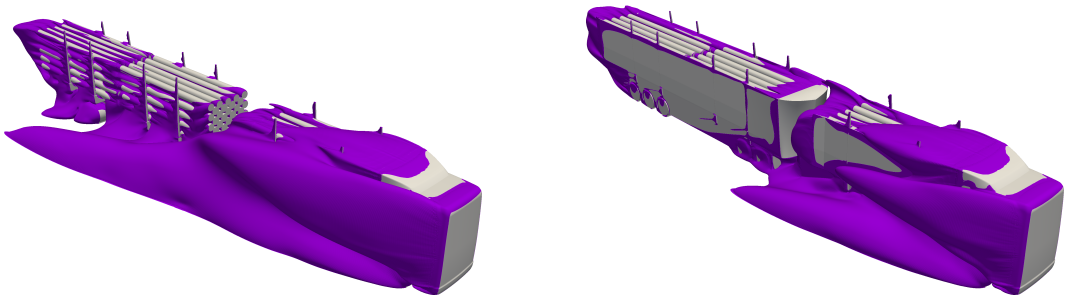

(a) (b)

Figure 4.68: Iso-surface of total pressure coefficient, leeward side. Baseline model (a), combination 1 (b). At 5 degree yaw angle.

As said before, the reduction of flow inside the gap achieved by the gap spoiler and faring removed most of the high pressure region present on the front face of the second stack, Fig. 4.69, furthermore, the lateral shielding of the flow, made together by the skirts and the lateral cover between the stakes, removed the high pressure on the stakes and the bunks also contributing to the drag reduction. The same effect is seen from the back, Fig. 4.70, in this all the suction regions downstream of each component has been removed by the lateral closing.

From the flow field on a horizontal plane place approximately at half height of the truck, Fig. 4.71, it can be noted the influence of the concepts on the different regions; mainly how the gap spoiler and fairing affect the wake on the leeward side at the gap position, whereas the boat-tail reduced the drag on the back face of the truck making the wake there shorter and narrower.

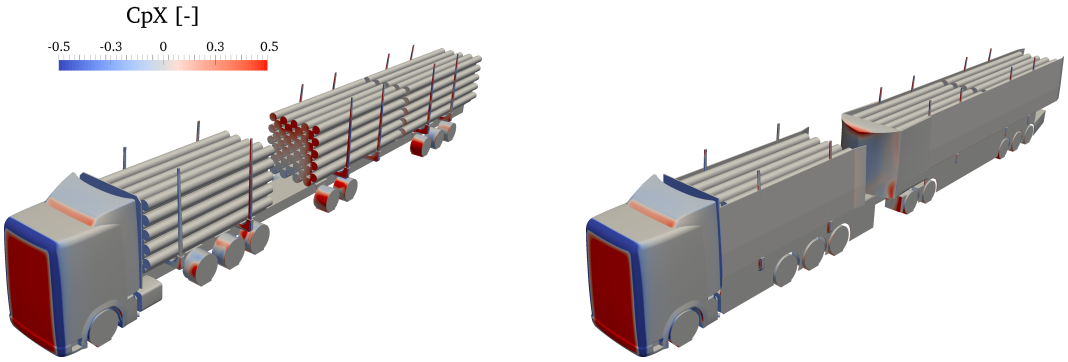

(a) (b)

Figure 4.69: Contour of static pressure coefficient, front view. Baseline model (a), combination 1 (b). At 5 degree yaw angle.

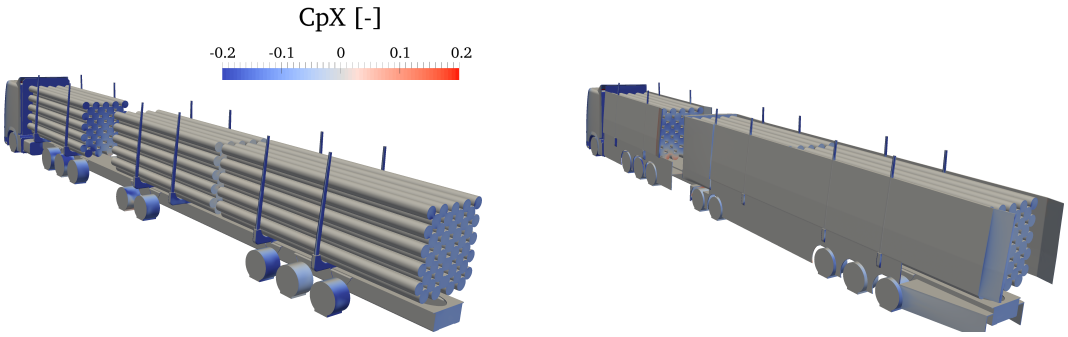

(a) (b)

Figure 4.70: Contour of static pressure coefficient, back view. Baseline model (a), combination 1 (b). At 5 degree yaw angle.

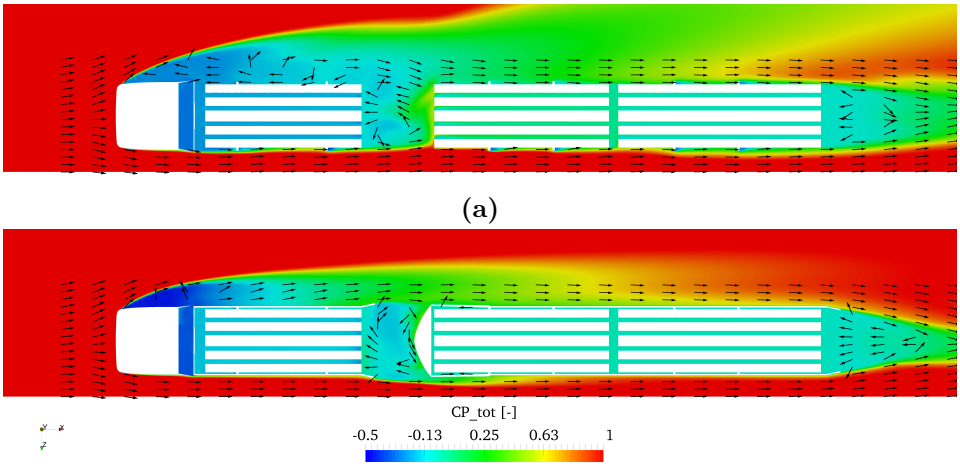

(a)

(b)

Figure 4.71: Comparison of total pressure coefficient at y= 1.25 m between the baseline model (a) and combination 1 (b). At 5 degree yaw angle.

If the flow field is analyzed on a plane cutting the domain longitudinally, Fig. 4.72, the effect of the boat-tail explained above can also be seen, with a smaller low

pressure region downstream of the truck. The reduction of high pressure inside the gap, and the modification of the flow direction created by the spoiler and fairing can also be seen on this plane. Finally, the improvement of the underbody flow is clearly visible, the shielding of the wheels with the skirts removed the high pressure regions under the frame, especially important o the front part of the wheels after the gap.

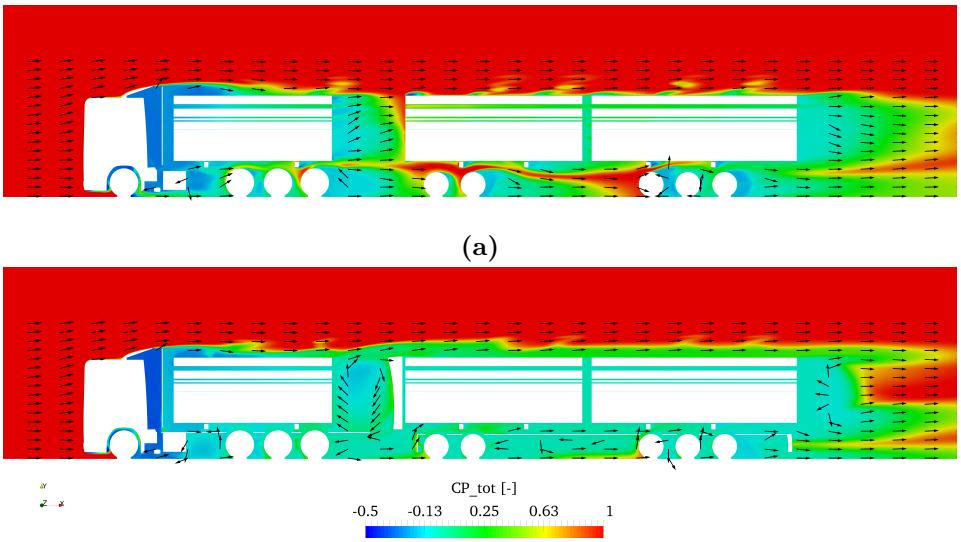

Figure 4.72: Comparison of total pressure coefficient at z=0.88 m between the baseline model (a) and combination 1 (b). At 5 degree yaw angle.

The drag coefficient build up, Fig. 4.73, shows the main regions where the drag has been reduced by the aerodyanmic concepts combinations; starting with a decrease in the bulkhead region due to the separation wake reduction achieved with the lateral cover; the gap region is also improved, in both faces, thanks to the gap spoiler and fairing; after the gap the higher side-skirts have a great effect by reducing the drag in each of the bunks positions; finally a small effect coming from the boat-tail can be seen in the back face of the truck.

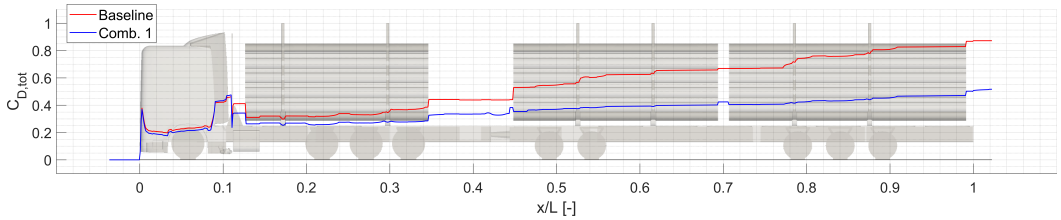

Figure 4.73: Drag coefficient build-up along the truck combination 1 compared with the baseline model at 5 degrees yaw angle.

4.3.2 Combination 2

Since the gap spoiler and the fairing aim for a similar modification of the flow field in the gap, and the gap spoiler showed a better performance when implemented alone with the original skirts than the gap fairing, a combination without the fairing, Fig. 4.74, was also studied maintaining the other concepts used on combination 1.

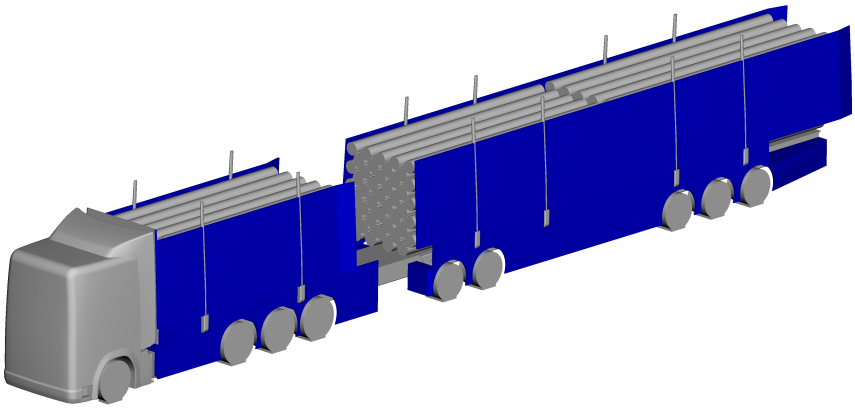

Figure 4.74: Geometry of the aerodynamic concepts combination 2.

The results for combination 2, Table 4.14, show that using only the spoiler on the gap region modified the flow field there and also around the truck, resulting in a further decrease of total drag coefficient to 0.467, a 47.6% with respect to the baseline model.

Table 4.14: Drag coefficient results for combination 2 compared with baseline and combination 1, for 5 degrees yaw angle.

Model	C_D	% from baseline	% from Comb. 1
Baseline	0.891	-	-
Comb. 1	0.532	-40.3	-
Comb. 2	0.467	-47.6	-12.2

From the wake shown on Fig. 4.75 and 4.76, it can be said that the difference on the total drag coefficient value comes mainly from the leeward side. On the windward side no big difference are found when the fairing is removed, Fig. 4.67 and 4.75, indicating that most of the influence on the wake on that side was coming from the gap spoiler.

However, removing the fairing does change the flow characteristics inside the gap; as seen on Fig. 4.77 more flow is leaving the gap region in the leeward direction on combination 1, influencing the flow upstream and modifying the separation behavior on the edge of the cabin, creating the low pressure region at medium height of the truck seen on Fig. 4.77 and 4.68.

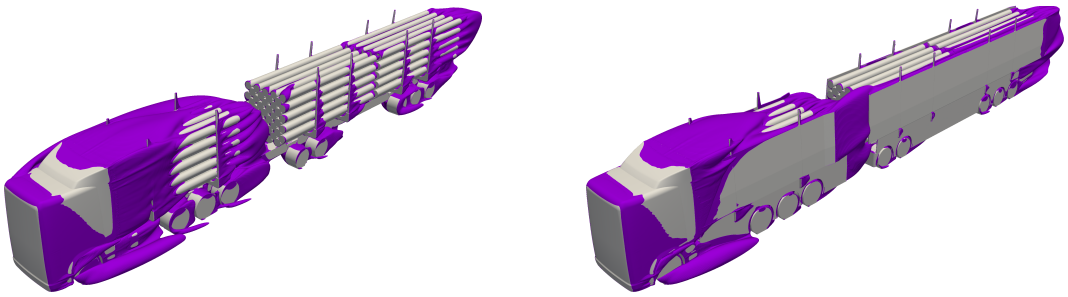

(a) (b)

Figure 4.75: Iso-surface of total pressure coefficient, windward side. Baseline model (a), combination 2 (b). At 5 degree yaw angle.

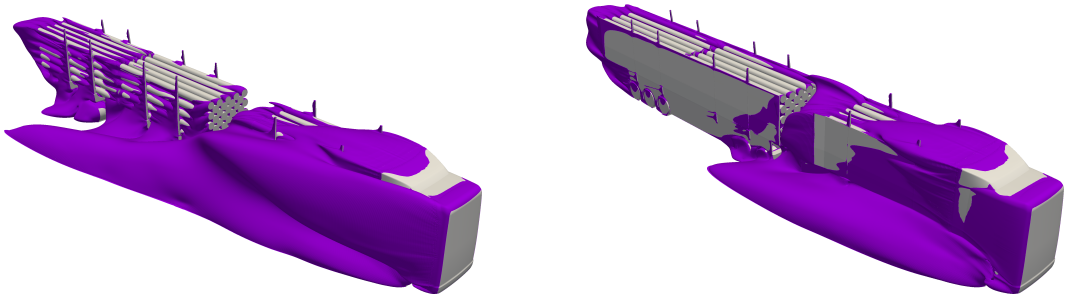

(a) (b)

Figure 4.76: Iso-surface of total pressure coefficient, leeward side. Baseline model (a), combination 2 (b). At 5 degree yaw angle.

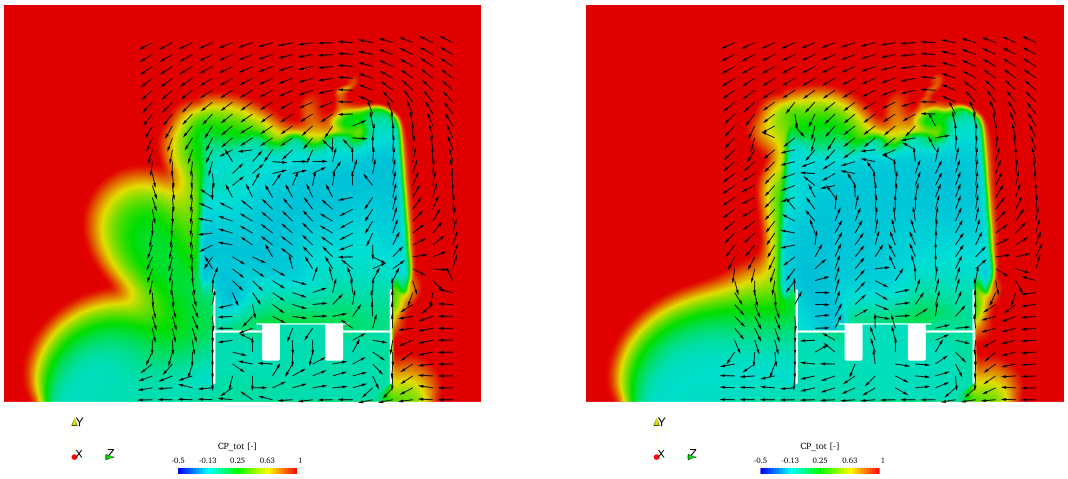

(a) (b)

Figure 4.77: Comparison of total pressure coefficient at x=0.34 m (gap region) between the combination 1 (a) and combination 2 (b). At 5 degree yaw angle.

The pressure distribution on the surfaces on Fig. 4.78 shows that the positive effect on the gap done by combination 1, Fig. 4.69, is also obtained in this case without the use of the fairing. That is, the reduction of the high pressure area and the creation

of a suction region on the front face of the second stack, is mainly generated by the deflection outwards of the flow by the gap spoiler and no by the addition of the gap fairing on the second stack. It can also be noted that, since for a timber truck only a lateral gap spoiler can be implemented, part of the high pressure region after the gap remains present since the wake leaving from the top of the first stack is not deflected by the gap spoiler as it would be if a top spoiler was added, such as the one used in common long trailer combinations.

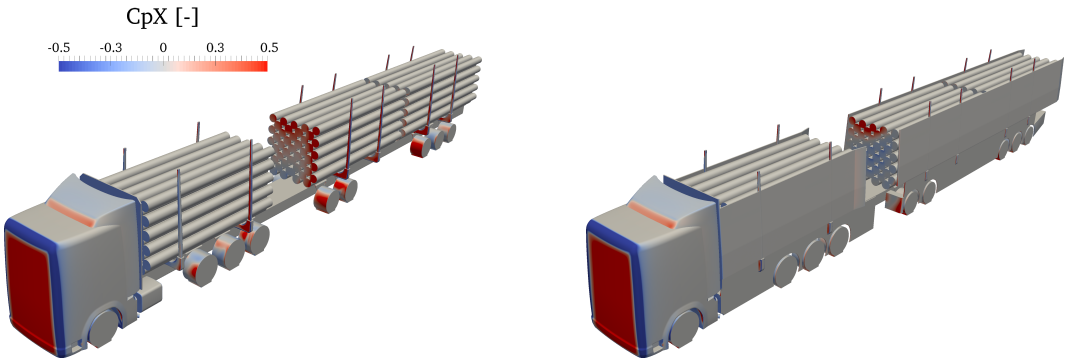

(a) (b)

Figure 4.78: Contour of static pressure coefficient, front view. Baseline model (a), combination 2 (b). At 5 degree yaw angle.

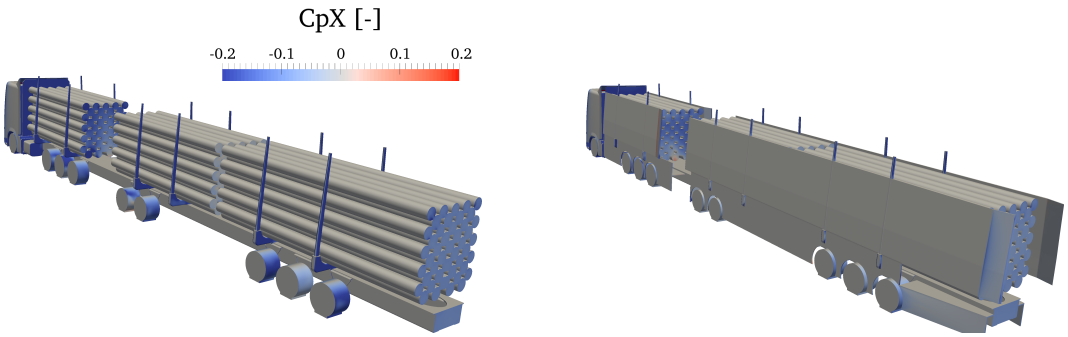

(a) (b)

Figure 4.79: Contour of static pressure coefficient, back view. Baseline model (a), combination 2 (b). At 5 degree yaw angle.

The same difference between the two combinations seen on the iso-surfaces of total pressure coefficient on the leeward side, can also be seen on a horizontal plane as shown in Fig.4.80 where the flow on that side of the track remains attached for this combination, whereas separation on the cabin edge was present when using the fairing, Fig. 4.71. Comparing the flow on the gap for the two combinations, Fig. 4.77, it can be noted that the use of the fairing causes more flow to go outside of the gap on the leeward direction, this flow can affect upstream inducing the separation on the cabin.

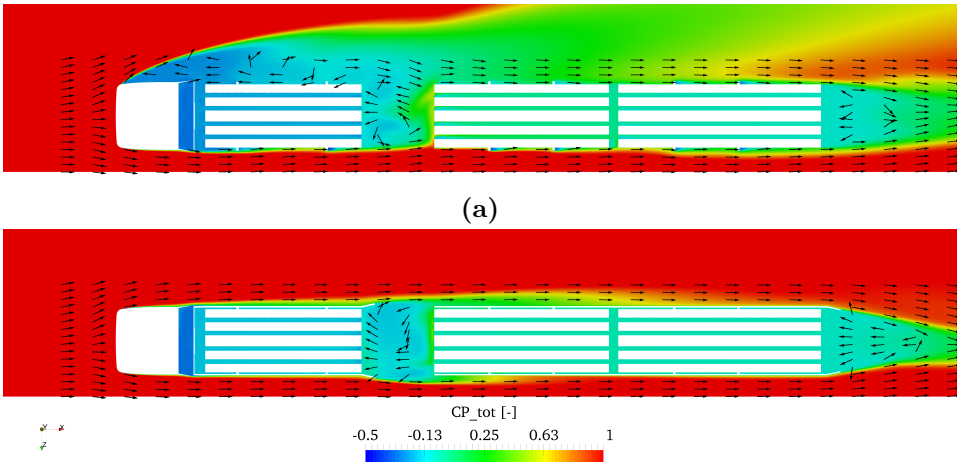

(a)

(b)

Figure 4.80: Comparison of total pressure coefficient at y= 1.25 m between the baseline model (a) and Combination 2 (b). At 5 degree yaw angle.

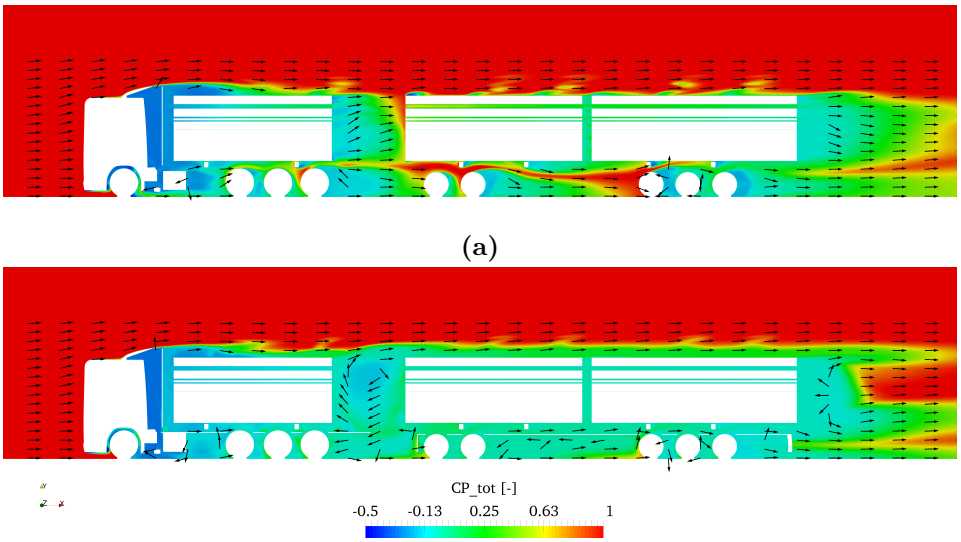

(a)

(b)

Figure 4.81: Comparison of total pressure coefficient at z=0.88 m between the baseline model (a) and Combination 2 (b). At 5 degree yaw angle.

From the drag coefficient build up comparison shown on Fig. 4.82, it can be noted that the difference in drag between the two tested combinations comes mainly from the cab region due to the separation wake explained above. After that, both combinations follow a similar tendency and the difference in drag is approximately constant between them, with a different behavior on the front face of the second stack caused by the gap faring that, as explained on Sec. 4.2, influences the flow considerably less than the gap spoiler.

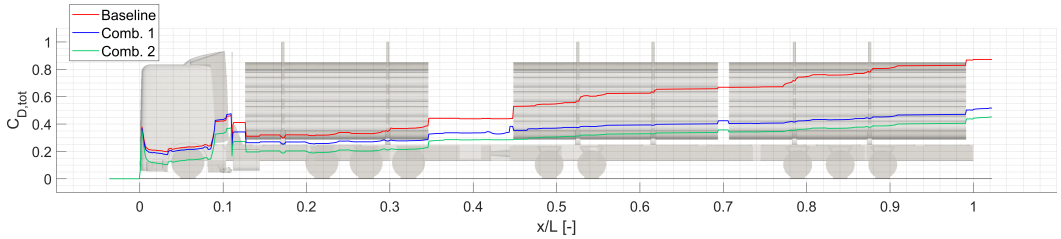

Figure 4.82: Drag coefficient build-up along the truck combination 2 compared with the baseline model at 5 degrees yaw angle.

For this last combination, which gave the best results on the 5 degrees yaw angle comparison, the whole sweep of cross wind conditions was run and it is compared with the baseline results on Fig. 4.83.

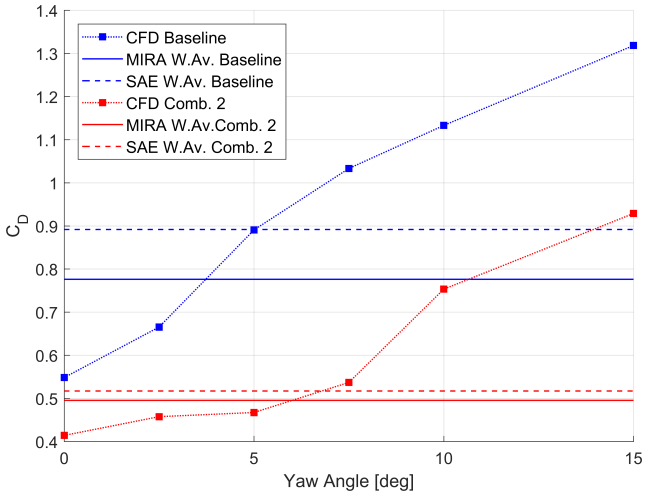

Figure 4.83: Drag coefficient comparison between Baseline and Combination 2 for different yaw angles.

As it can be noted from Table 4.15 the effects of the aerodynamic concepts combination are present in the whole angle sweep, however they seem to be more effective for the medium yaw angles (5 and 7.5 degrees), where the reduction of drag coefficient is close to a 50% with respect to the baseline, whereas for the rest of the yaw angles this reduction is around a 30%.

This difference effectiveness of the combination comes from the sensitivity to separation found on the leeward side of the cabin, Fig. 4.84; as explained before, for the baseline this separation was present starting from the 2.5 degrees yaw angle case and becoming especially important for 5 degrees and larger angles. The implementation of some of the concepts explained on Sec. 4.2 can remove this separation on the cabin by modifying the flow in the gap (mainly the gap spoiler) and in the region between the bulkhead and the first stack (done by the lateral shield), this proved to be really effective for the medium yaw angles. However, for larger yaw angles the separation is more influenced by the crosswind condition, resulting on separated flow even with the addition of the aerodynamic concepts, hence the drag is reduced but not in the same level as in the yaw angles where the separation was removed.

Table 4.15: Drag coefficient comparison between Baseline and Combination 2 for different yaw angles.

Yaw angle [deg]	C_D Baseline	C_D Comb.2	% from baseline
0	0.5482	0.4141	-24.5
2.5	0.6654	0.4576	-31.2
5	0.8916	0.4673	-47.6
7.5	1.033	0.5369	-48.0
10	1.133	0.7532	-33.5
15	1.318	0.9287	-29.5
MIRA Wind Av.	0.776	0.495	-36.2
SAE Wind Av.	0.891	0.517	-42.0

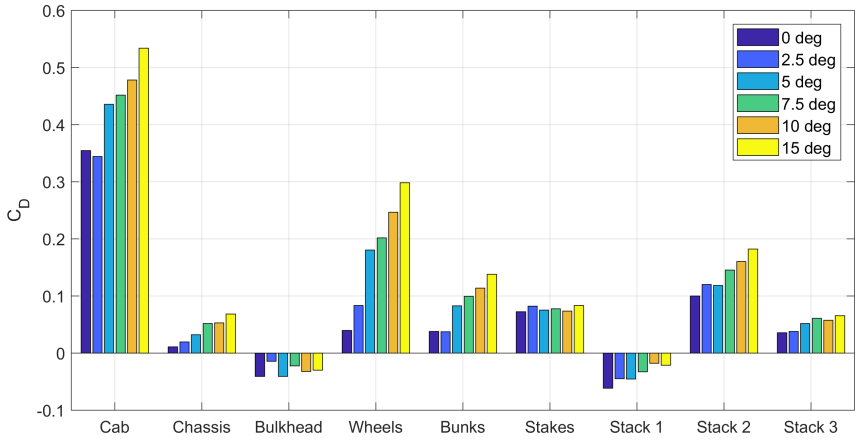

(a)

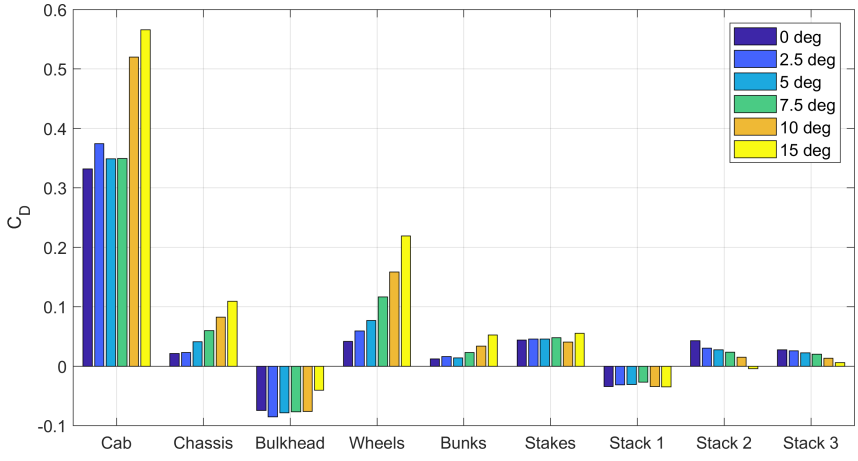

(b)

Figure 4.84: Surface breakdown of the total drag coefficient for the different yaw angles; Baseline model (a), Combination 2 (b).

The surface breakdown of the drag coefficient on Fig. 4.84 shows how the reduction with respect to the baseline model follows a similar tendency with increasing yaw angle for all the components of the truck, except from the cab. The results on the cab show a large reduction for 5 and 7.5 degrees but not significant changes for 10 or

15 degrees, cases for which the separation is still present and caused by the lateral wind.

From Fig. 4.84 it can also be noted that the main regions affected by the concepts, apart from the explained situation on the cab, are the gap (front face of the second stack), as intended by the use of the gap spoiler; and the wheels due to the positive effect of the skirts, which also reduced the drag on the bunks since the higher skirts were used for the combinations. In general all the regions are improved by the concepts, for example the third stack thanks to the boat-tail; but the gap and the wheels were the main objective due to their higher contribution to the total drag on the baseline model, hence it can be concluded that the aerodynamic concept combination performed well and in the expected regions.

4.4 Unloaded truck

A timber truck needs to travel unloaded half of the time, therefore it is important to obtain a concept combination that can perform well both in the unloaded and fully-loaded configurations. Even though on the previous section Combination 2 produced less drag coefficient on the fully-loaded configuration, the use of the fairing was considered important for the unloaded configuration since, otherwise, there would be more surface of the lateral cover exposed to the freestream flow after the gap on the leeward side of the truck. Hence, the load was removed from Combination 1, Fig. 4.85, to test its performance as an unloaded timber truck.

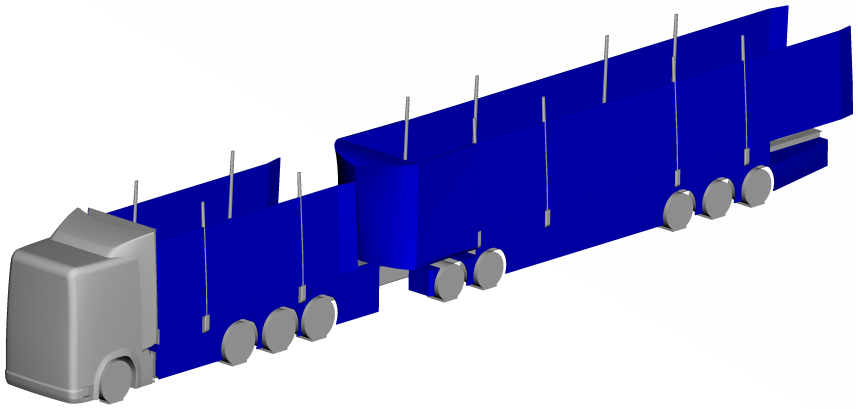

Figure 4.85: Geometry of the unloaded truck based on aerodynamic concepts Combination 1.

The results for this combination of aerodynamic concepts, both in the loaded and unloaded configurations, are presented on Table 4.16 together with the respective baseline results.

Table 4.16: Drag coefficient results for combination 1, compared with baseline model, for loaded and unloaded configurations. At 5 degree yaw angle.

Configuration	Baseline C_D	Comb. 1 C_D	% from baseline
Loaded	0.891	0.532	-40.3
Unloaded	0.696	0.639	-8.20

From these results it can be noted that the combination proved to be more effective on the loaded configuration, although a small reduction of drag coefficient was also achieved on the unloaded model. Comparing the results from the concepts combination, the drag coefficient was increased a 20.1% when removing the load with respect to the original value of Combination 1 implemented on the loaded truck.

4.5 Stack configurations

Apart from the aerodynamic concepts explained on the previous sections, three different loading configurations were also studied to see its influence on the total drag coefficient; for this two new geometries, Fig. 4.86, were compared with the baseline model without using any of the aerodynamic concepts.

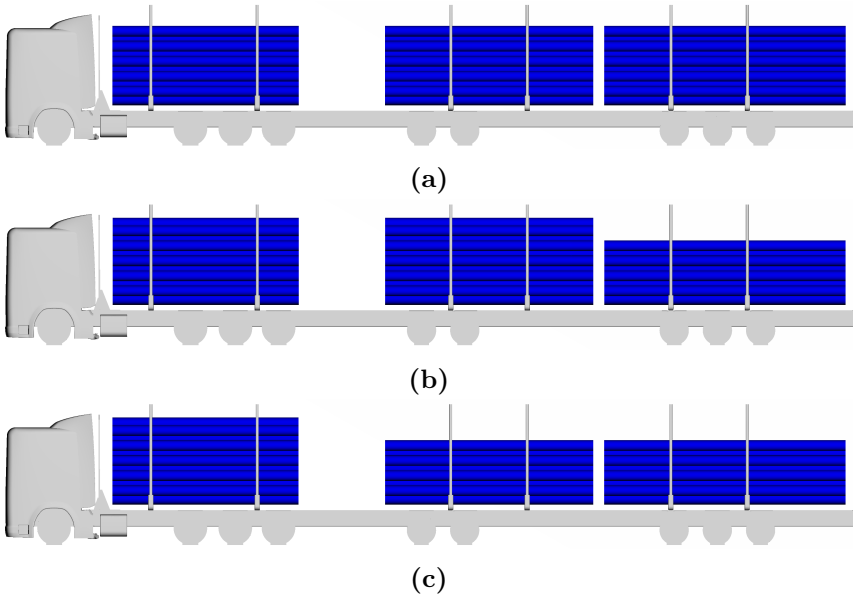

Figure 4.86: Different loading configurations: baseline (a), configuration 1 (b), configuration 2 (c).

Results shown on Table 4.17 indicate that increasing the load directly after the gap, higher second stack, gives a worse performance in terms of drag coefficient. However, if both stacks after the gap are decrease and the maximum load possible is placed behind the cabin, as seen in Configuration 2, a decrease of drag coefficient can be achieved. It can also be noted that the volume of load that could be transport in both configurations follows a similar tendency, that is, in the case in which more

drag is created the percentage of load that is added is larger that the increase of drag. And, when the possible volume of load is decrease, the gain in drag reduction is percentage-wise larger.

Table 4.17: Drag coefficient results and volume load difference for the loading configurations and comparison with baseline model. At 5 degree yaw angle.

Model	C_D	% from baseline	% Vol. load dif.
Baseline	0.891	-	-
Configuration 1	0.902	+1.23	+4.5
Configuration 2	0.760	-14.7	-8.1

The build up of the drag coefficient along the truck, Fig. 4.87, shows that increasing the load on the first stack does barely affect the drag coefficient, since the three configurations have the same value of drag until the end of the gap. Is the change of height on the second stack where the main difference between the configuration are found, getting higher drag coefficient for more load on the second stack. Moreover, the use of two difference heights after the gap is also detrimental for the performance of the truck, it can be seen on Fig. 4.87 that Configuration 1 has a larger increase on drag coefficient on the small gap between second and third stacks.

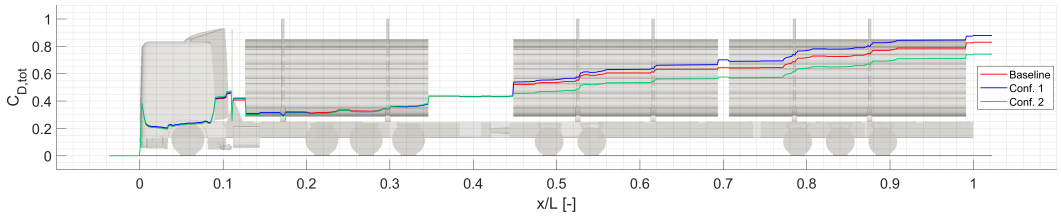

Figure 4.87: Drag coefficient build-up along the truck for three different loading configurations at 5 degrees yaw angle.

The static pressure coefficient on the truck surfaces, Fig. 4.88, shows the importance of the lower second stack for decreasing the total drag coefficient, on Configuration 2 the high pressure region on the top part of the front face of the second stack has completely disappeared since the flow leaving the first stack goes directly on top of the second. On the other hand, the higher second stack on Configuration 1 incresed that frontal area and therefore more high pressure region, and more drag.

Regarding the importance of keeping the same height on the two stacks after the gap, it can be seen on Fig. 4.89 that the change of height present on Configuration 1 creates a separation region on the small gap, this explain the larger increase of drag on that region shown on Fig. 4.87.

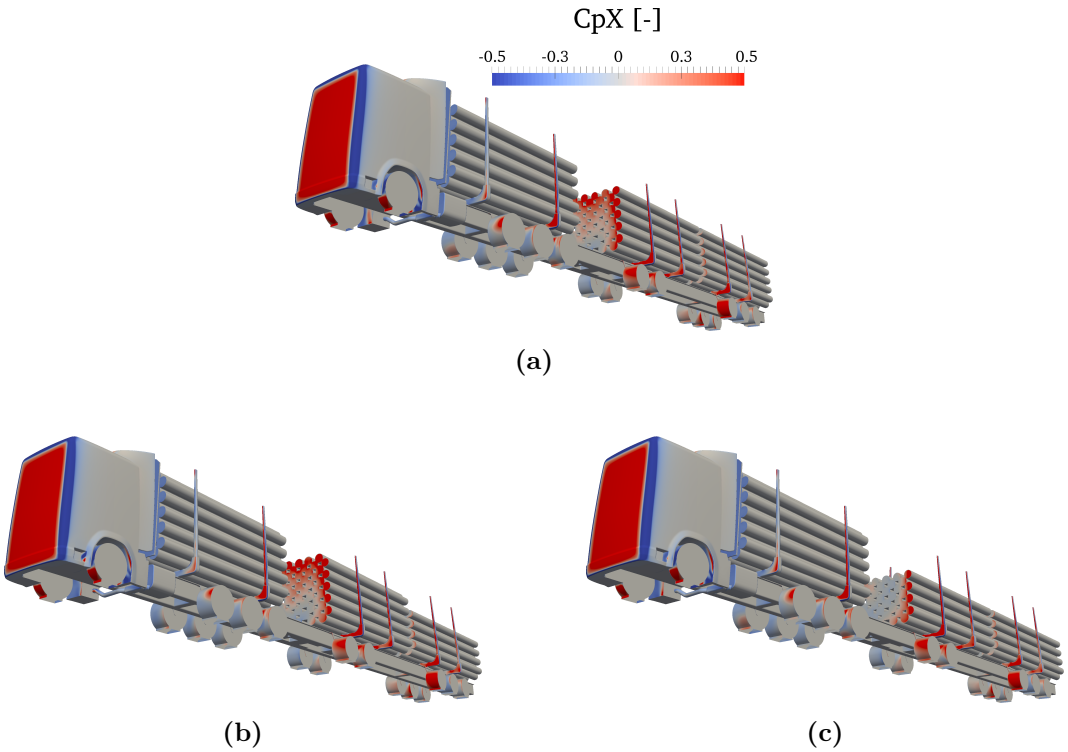

(a)

(b) (c)

Figure 4.88: Contour of static pressure coefficient, front view. Baseline model (a), Configuration 1 (b), Configuration 2 (c). At 5 degree yaw angle.

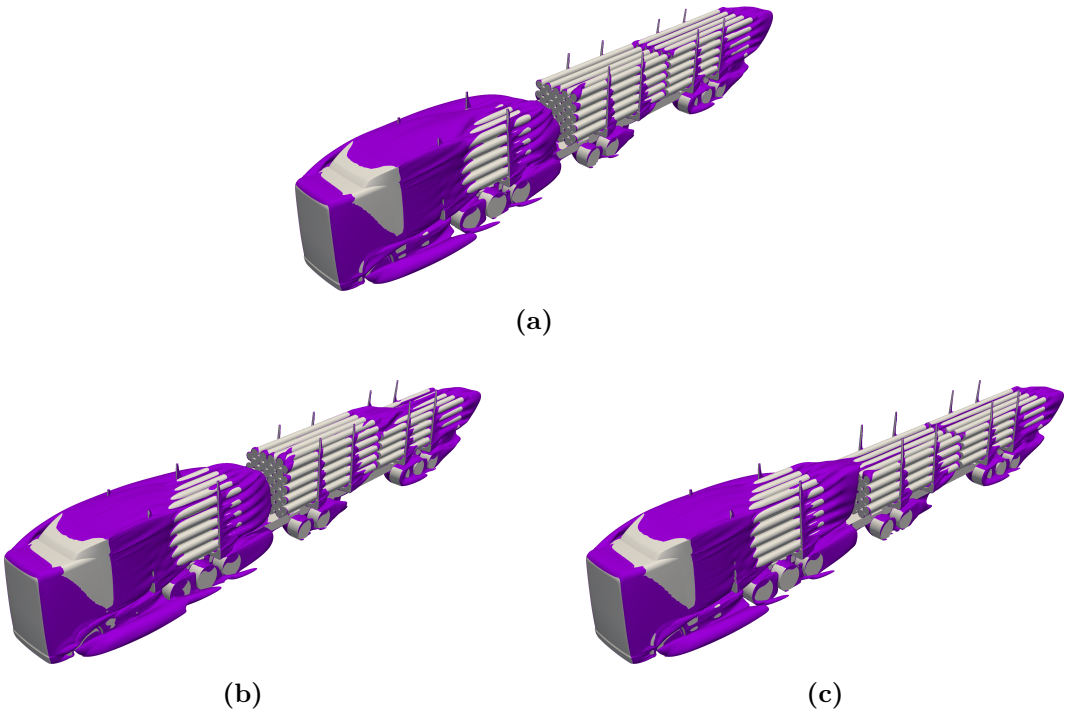

(a)

(b) (c)

Figure 4.89: Iso-surface of total pressure coefficient. Baseline model (a), Configuration 1 (b), Configuration 2 (c). At 5 degree yaw angle.

4.6 Improved simulation speed

This section presents the final results on the simulation speed methodology study obtained on the three different geometries tested.

4.6.1 Allan body

First, following the procedure explained on Sec. 3.4, the influence of different individual parameters on the convergence of the drag coefficient monitor was studied. Starting from the baseline setup of the URANS solver described on Table 3.11; the PBC-Courant number, the number of iterations per time step or the gradient discretization scheme were modified one by one and the drag coefficient convergence compared with the baseline setup result.

Fig. 4.90 shows the influence of using a larger PBC-Courant number, it can be noted that a larger value gives faster convergence removing the oscillations in a fewer number of iterations. Whereas, Fig. 4.91 shows that there is not a big influence on using one iteration more inside each time step, hence 2 iterations were used for the rest of the simulations since converging each time step is not the focus of the solver approach, but advance the solution faster to a final steady state converged solution, introducing more iterations inside each time step will just slow down the process. Hence, from this two results it was concluded that 2 iterations per time step is enough for the aim of the study and that a larger value of PBC-Courant number speeds up the convergence giving more stable values of the drag coefficient monitor.

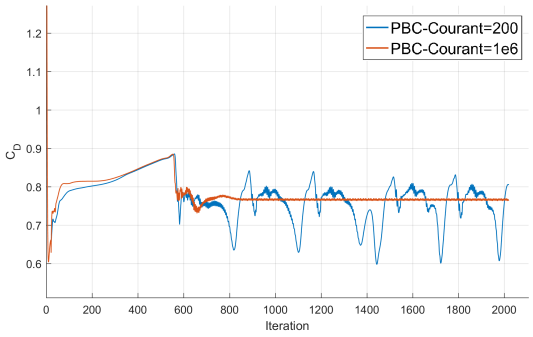

Figure 4.90: CD results for 0.1 seconds time step ($\alpha_t = 8$) with 2 iterations per time step, comparison of two different PBC-Courant flow numbers.

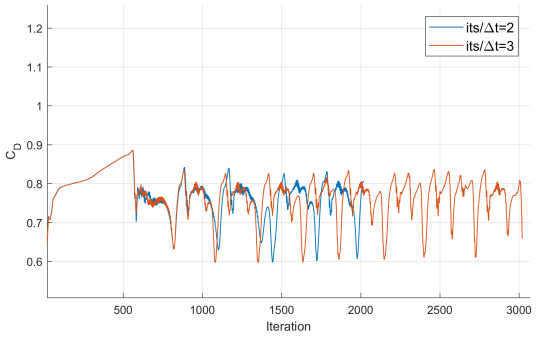

Figure 4.91: CD results for 0.1 seconds time step ($\alpha_t = 8$) with PBC-Courant flow number of 200, comparison of different number of iterations per time step.

For clarification with the results shown on Fig. 4.92, it must be said that only this first two independent studies on the PBC-Courant and the number of iterations per time step were initialized with the FMG method, as the steady RANS solutions, whereas all the the final results shown on Fig. 4.92 are initialized using standard initialization as explained on Sec. 3.4.

Final results showing the best settings in terms of drag coefficient convergence are shown on Fig. 4.92 compared with both the steady RANS solution and the URANS baseline setup solution, all the indications in the legend are the changes made with respect to the baseline setup on Table 3.11.

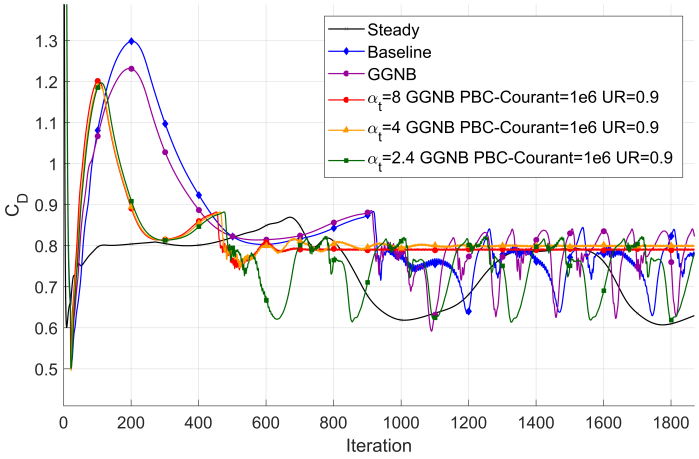

Figure 4.92: CD results for different solver settings, compared with the steady state solution and the URANS baseline setup.

First it can be seen that changing the discretization scheme for the gradients from Least Squares Cell Based to Green-Gauss Node Based improved the convergence of the simulation, purple and blue lines. Regarding the PBC-Courant number, as explained before, a larger value gave faster convergence. Moreover, adding also more under-relaxation on the turbulence model equations (k and ε equations) by increasing the implicit under-relaxation factor to 0.9, also improved the convergence. This two modifications of the settings have the same effect on different variables of the flow field, that is, introduce less information from the previous solution on the current iteration as explained on [16].

Finally, with the high values of PBC-Courant and implicit under-relaxation factor, a analysis on the time step size was done. It can be noted from the three last results shown on Fig. 4.92 that in this case decreasing the time scale factor α_t to 2.4 the oscillations in the drag coefficient monitor increased. That could be caused by the fact of been closer to the characteristic time of the problem and the turbulent structures created due to the Allan body geometry.

Furthermore, when the residuals were checked to assess the convergence of the solution it was notice that a sudden increase on them was present in all the simulations run with the URANS approach, indicating that the final result could not be trusted.

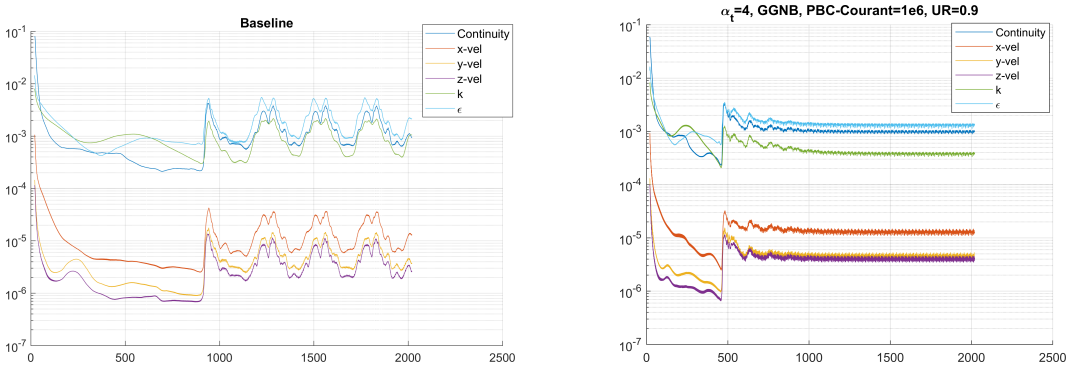

Figure 4.93: Residuals for the baseline (a) and the best solver setup (b) for the Allan body URANS simulations

The best results, in terms of faster convergence and less oscillation of the drag coefficient value, were obtained with a time scale factor of 4. Fig. 4.93(b) shows that the residuals drop relatively fast to low values until a sudden increase around iteration 450, where no modifications in the solver setup were introduced. To understand the behavior of the solution, the flow field at three different moments of the solution advancement were study, Fig. 4.94: before the sudden increase of residuals (after 450 iterations), directly after the increase of the residuals (at iteration 550), and once the residuals reached a stable value (iteration 700).

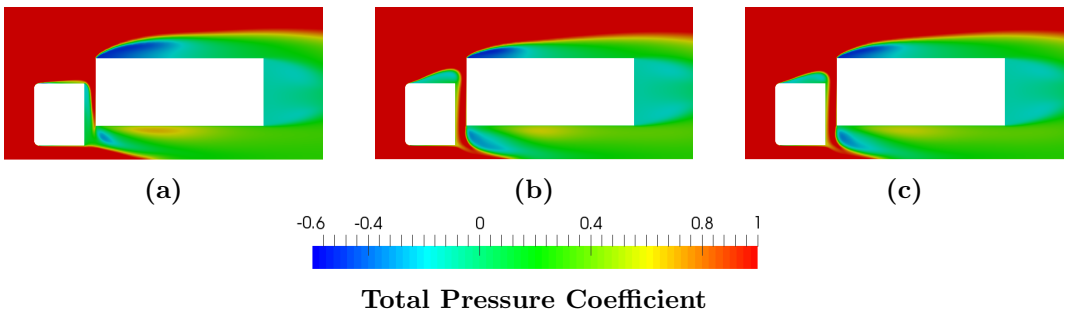

Figure 4.94: Contours of total pressure coefficient on the symmetry plane after: 450 iterations (a), 550 iterations (b) and 700 iterations (c).

It can be noted from Fig. 4.94 that the sudden increase of residuals around iteration 500 was caused by the separation of the flow on the top surface of the front box, which is not present at iteration 450, Fig. 4.94(a), but is constant after the increase

of the residuals, Fig. 4.94(b) and (c). With this results it was determined that this solution approach with the URANS solver is more sensitive to the separation induced by the geometry of the model and more demanding in terms of mesh quality to obtain good results.

It was due to this large influence of the geometry-induced separation on the URANS approach results and convergence, that the same solver settings were also tried on more simple geometries, such as a 2D NACA 0008 airfoil and a 3D GTS model.

4.6.2 NACA 0008

Following the results obtained on the Allan body and the convergence problems found due to the separation induced by the geometry in the gap; the simpler geometry of a 2D NACA 0008 symmetrical airfoil was used for the methodology study.

Same procedure followed on the Allan body was applied, that is, a steady RANS simulation was run to get a value of drag coefficient for each iteration, Fig.4.95 black line, and the residuals drop until convergence was reached, Fig. 4.96(a). This steady RANS case was used as a reference solution to compare the gain in simulation speed when using the URANS model. A baseline setup for the URANS model was set as describe for the Allan body on Table 3.11, with the only difference of the time scale factor, in this case $\alpha_t = 2.5$.

Different solver settings were tested and the most relevant results are shown on Fig. 4.95, compared with both the steady RANS solution and the URANS baseline setup. First, as seen on the previous section, the use of Green-Gauss Node Based scheme for the gradient discretization speeds up the convergence of the solution; therefore, the simulations run on the NACA 0008 model used this scheme.

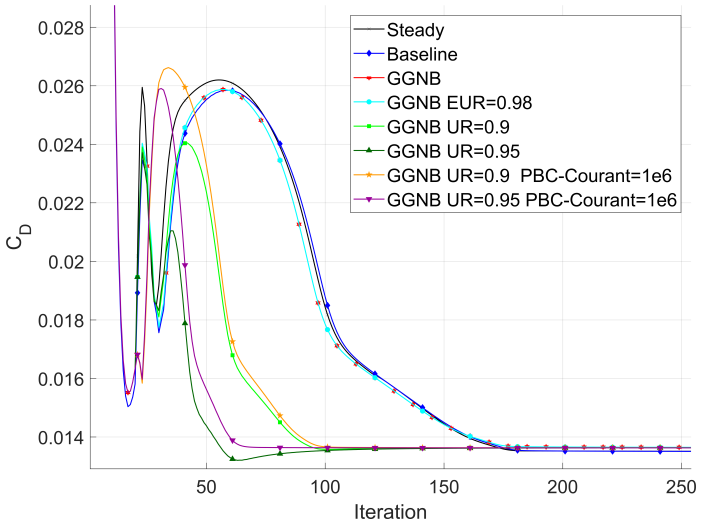

Figure 4.95: Drag coefficient results over iteration for different solver settings applied on the NACA 0008 model.

Then, with the Green-Gauss Node Based scheme set for all the cases, the under-relaxation factor and the PBC solver Courant number were tuned to see their influ-

ence on the drag coefficient monitor convergence and on the residuals drop.

From the results of drag coefficient over iteration, Fig. 4.95, it can be seen that the increase of the implicit under relaxation on the turbulence model equations from the baseline value of 0.8, clearly speeds up the convergence, reaching a stable drag coefficient in 100 iterations when using an under relaxation factor of 0.9 and around 80 iterations if the factor is increased until 0.95.

Regarding the influence of the solver Courant flow number, it can be seen when comparing the cases with same implicit under-relaxation factor (UR) on Fig. 4.95 that the increase of Courant number to 1e6 only improved the convergence speed on the case with higher under-relaxation (UR=0.95), whereas no impact was seen on the other case. No big influence was found either when changing the explicit under relaxation factor (EUR) alone, up to 0.98, in this case.

Fig. 4.96 compares the behavior of the residuals of some of the fastest solver settings tried with respect to the steady RANS simulation and the baseline setup of the URANS approach. Whereas, no big impact of the Courant flow number was found on the convergence speed of drag coefficient over iteration, Fig. 4.95; it can be noted that increasing it from 200, Fig. 4.96(e) and (g), to 1e6, Fig. 4.96(f) and (h), clearly improves the convergence of the simulation, speeding up the drop of the residuals in such a way that low enough and stable values of the residuals to consider the simulation converged are obtained after less than 100 iterations when combined with an implicit under relaxation factor of 0.95.

Hence, from the results shown on both Fig. 4.95 and 4.96, it can be said that increasing the Courant flow number on the Pressure Based Coupled solver and the implicit under relaxation factors on the turbulence model equations, k and ε in this case, speeds up the convergence of the flow field solution. It must be considered that the symmetric 2D NACA 0008 airfoil model at 0 degrees angle of attack is a very simple flow field in which the URANS approach for increasing the convergence speed seems to work fine since no big changes of geometry creating separation are present. However, when applied the same solver settings to other cases, some instabilities on the solutions could appear due to high values of under-relaxation factors and/or Courant numbers.

The solver settings leading to the best results in terms of convergence speed for the NACA 0008 airfoil are summarized on Table 4.18. This setup reached convergence in around 80 iterations, more than a 100 iterations earlier than the steady RANS simulation.

Table 4.18: Solver settings used for the best results obtained on the NACA 0008 model.

Parameter	Value
α_t	2.5
PBC-Courant	1e6
EUR	0.75
UR	0.95

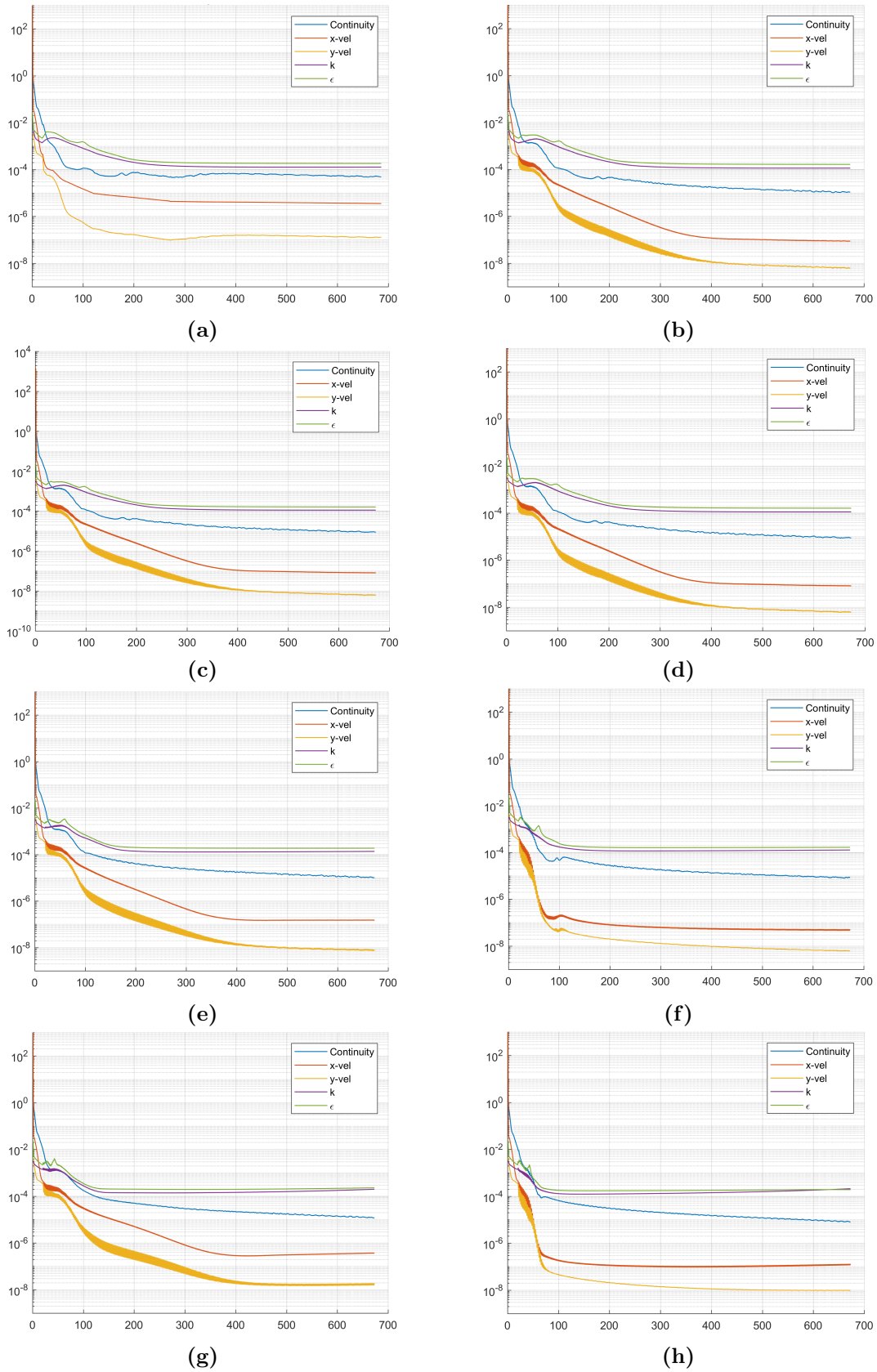

Figure 4.96: Residuals of the NACA 0008 simulations: Steady (a), baseline (b), GGNB (c), GGNB EUR=0.98 (d), GGNB UR=0.9 (e), GGNB UR=0.9 PBC-Courant=1e6 (f), GGNB UR=0.95 (g), GGNB UR=0.95 PBC-Courant=1e6 (h).

4.6.3 Ground Transportation System model

Finally, the simulation speed study was carried out on the 3D GTS model. As done on the previous cases a steady RANS simulation was run as a reference for the convergence speed. For the setup, as explained on 3.4.3, the Green-Gauss Node Based discretization scheme for the gradients was used on this model for all the simulations, including the steady RANS. The baseline setup of the solver for the URANS model is described on Table 3.14.

Fig. 4.97 shows the convergence of the total drag coefficient monitor for different solver settings, including changes on explicit under relaxation factor (EUR), implicit under relaxation factor (UR) and the Pressure Based Coupled solver Courant flow number; legend indicates changes with respect to the baseline URANS setup of Table 3.14.

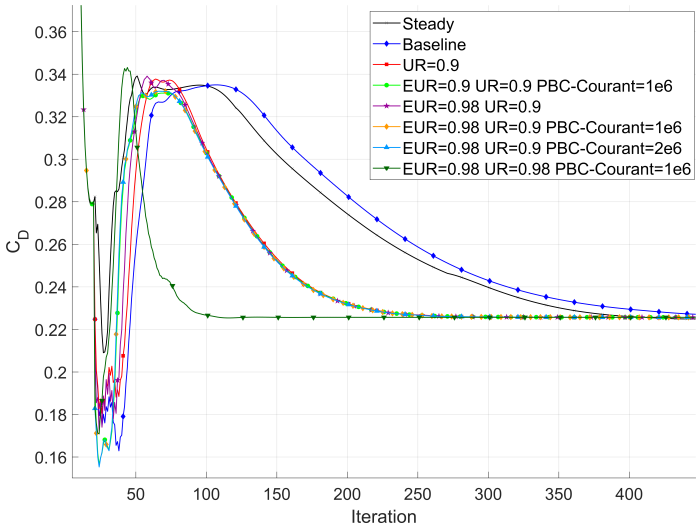

Figure 4.97: Drag coefficient results over iteration for different solver settings applied on the GTS model.

From all the results showed on Fig. 4.97 it can be noted that the main difference on the convergence speed of the drag coefficient came from the changes on the implicit under relaxation factor (UR). Whereas changes on the explicit under relaxation factor (EUR) did not influence the value of drag coefficient per iteration (comparison between light green and orange lines). Equivalently, a further increase of Courant number from 1e6 to 2e6 did not speed up the convergence anymore (comparison between orange and light blue lines). Hence, the fastest results shown on Fig. 4.97 correspond to a high value on both under relaxation factors, although the effect comes mainly from the implicit one (UR), and a Courant number of 1e6.

From the residuals' evolution shown on Fig. 4.98 for all the cases analysis on Fig. 4.97; it can be seen how the fastest convergence of drag coefficient monitor also has the fastest drop of the residuals, reaching a low and stable value in less than 200 iterations, Fig. 4.98(h). Regarding the influence of the different parameters, the same tendency explained before is also noticed on the residuals. If Fig. 4.98 (e), (f), (g) are compared, it can be noted that increasing the Courant number

from 200 to 1e6 and to 2e6 did not improve the convergence of the residuals, when keeping the under relaxation factors with the same values. However, increasing the implicit under relaxation factor on the turbulence model equation from 0.9 to 0.98 (Fig. 4.98(f), (h)) speed up the dropping of the residuals (especially on k and ε equations) significantly.

Regarding the time step, it was studied the influence on changing its size after a certain number of iterations. According to [23], it is better to start with a larger time step size and then reduce it for the last iterations of the simulation. In this study two time step sizes were applied; that is, after the first 20 iterations run with RANS for initialization of the flow field, the next 50 iterations were run with a larger time step size and then reduce until the final convergence of the solution.

The baseline time step size, 0.12 seconds, corresponded to a time scale factor of 2.5 over the problem's characteristic time, obtained as explained on Appendix A.1. For the time step size study two cases were simulated, using the baseline size as the larger or as the smaller of the two sizes used on each case; and using half of the initial size for the last part of the simulation. That is, using a scale factor of 5 on the first 50 iterations and then changing to 2.5; or using 2.5 first and finally reducing it to 1.25.

Fig. 4.99 shows the results for the time step size analyis, maintaining the same solver settings that gave the fastest convergence on Fig. 4.97. Compared with the constant time scale factor case, ($\alpha_t = 2.5$), it can be noted that using a larger time step than the baseline on the first iterations sped up the convergence; however, decreasing the time step size to levels close to the characteristic time of the problem ($\alpha_t = 1.25$), did not improve the behavior of the solution, the reason for that could be that with this smaller time step size the URANS solver could be starting to resolve part of the turbulence scales of the problem, which is not the aim for using this approach on this study.

Table 4.19: Solver settings used for the best results obtained on the GTS model.

Parameter	Value
α_t	5 (first 50 its.) and 2.5
PBC Courant	1e6
EUR	0.98
UR	0.98

This same behavior is seen on the residuals on Fig. 4.100 where more oscillations are present for the smaller time step size, whereas the fastest convergence was obtained by increasing it on the first iterations with respect to the baseline size used on the last ones, this allowed for a convergence in approximately 150 iterations. These results mean that a converged steady state solution can be reached, approximately, 450 iterations earlier than with the standard steady state solver approach when using the optimal settings shown on Table 4.19.

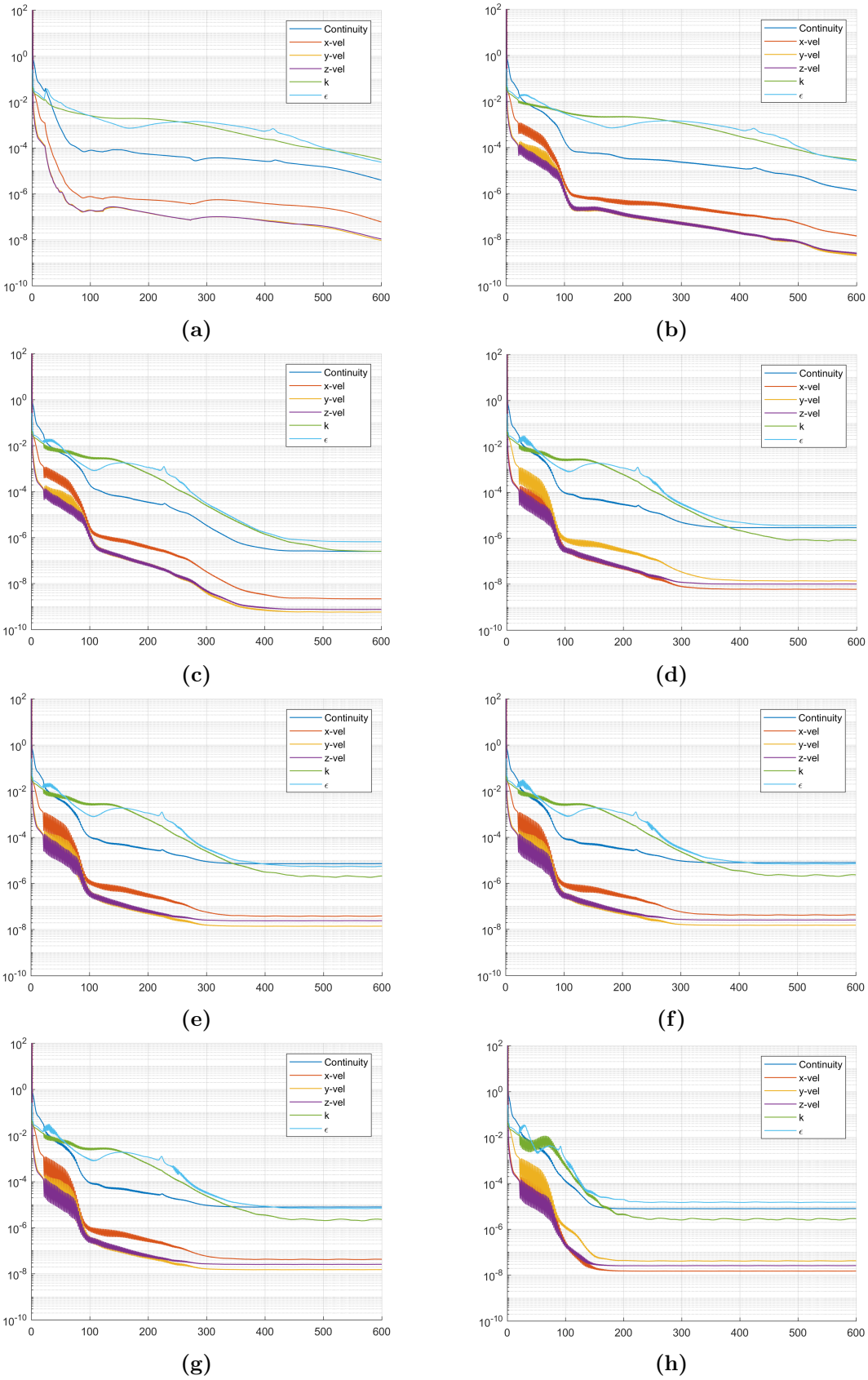

Figure 4.98: Residuals for GTS simulation with constant time step size. Steady state (a), baseline (b), UR=0.9 (c), EUR=0.9 UR=0.9 PBC Courant=1e6 (d), EUR=0.98 UR=0.9 (e), EUR=0.98 UR=0.9 PBC Courant=1e6 (f),EUR=0.98 UR=0.9 PBC Courant=2e6 (g),EUR=0.98 UR=0.98 PBC Courant=1e6 (h).

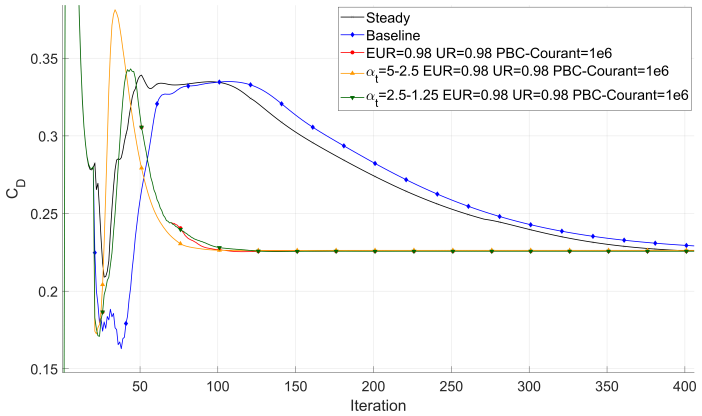

Figure 4.99: Drag coefficient results over iteration for different solver settings applied on the GTS model.

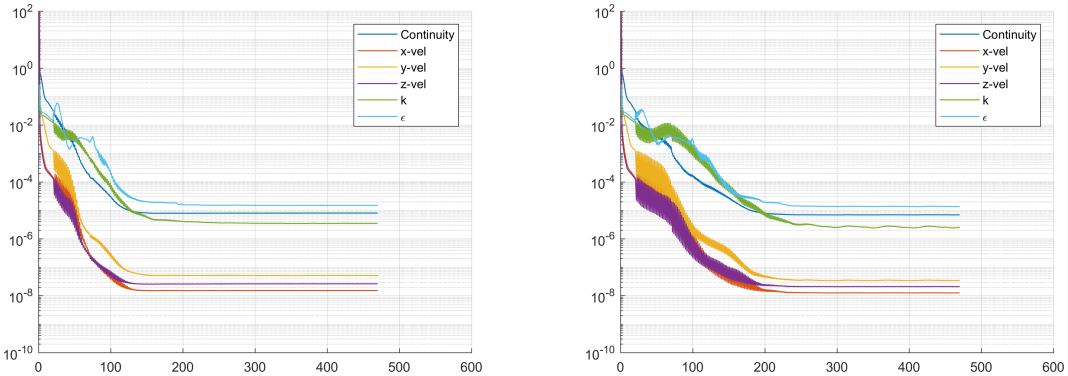

(a) **(b)**

Figure 4.100: Residuals for GTS simulations with variable time step size. $\alpha_t = 5$ and $\alpha_t = 2.5$ (a), $\alpha_t = 2.5$ and $\alpha_t = 1.25$ (b).

4.7 Methodology discussion

This section consists of a general discussion of the methods applied during the work and their influence on the results obtained.

First, the study done on the Allan body model in order to validate the recommended CFD methodology described in [19] concluded that a hexahedral mesh of $y^+ \approx 30$ together with the Realizable $k-\varepsilon$ turbulence model with Enhanced Wall Treatment was a good approach to apply on the timber truck simulations. Results obtained on the Allan body were in good agreement with both experimental wind tunnel data from [7] and CFD simulation with similar setup on [1].

The results on the baseline model of the fully loaded timber truck showed that a simplification of the stacks geometry, consisting on closing them and therefore remove all the flow going between the logs, was not acceptable since the drag coefficient values differed in more than a 14% for medium values of yaw angle, especilly 5 degrees. It was shown that this difference was given by separation on the leeward side of the cab, region that showed a great sensitivity to the amount of flow going on that direction. Regarding the results obtained for the realistic baseline model, the same tendency found on the wind tunnel results on [6] was achieved, although the values obtained on this report were lower. However, this could be expected due to the possible different loading configurations tested; as shown also in this report that can have a great impact on the drag value especially is modifications are done on the stacks placed after the main gap.

The separation on the leeward side of the cabin also showed to be very sensitive during the aerodynamic concepts study. This caused that modifications added in other regions of the truck, especially on the gap, affected the flow upstream changing the separation behavior on the leeward side of the cabin, making the global effect of each concept dependent on how that region was affected apart from its own effect on the desired region. Nevertheless, it was found that modifications on the regions with larger contribution to the total drag on the baseline were the most effective overall, that is gap spoiler for the gap region, and skirts with increased height until the bunks for the underbody and underload regions.

Finally, the methodology development study on the simulation speed using the URANS model showed a big dependency on the mesh quality, especially if separation could appear in some regions of the geometry. This could be seen on the Allan body study where the separation downstream of the front box prevent the study from reaching good conclusion. Studies on simpler geometries, NACA airfoil and GTS model, showed that a speed up of the convergence to the steady state solution can be achieved with the correct settings on the URANS solver, these settings are also really dependent on the particular case of study which make it difficult to obtain a general tuning.

5 Conclusions

A study of the aerodynamic performance of a fully-loaded timber truck has been done in this report; from a previous analysis on the Allan body model it was decided that a hexahedral mesh and the Realizable $k-\varepsilon$ turbulence model were adequate for the timber truck due to better correlation with experimental and other CFD simulations results.

First, from the baseline model analysis, it could be concluded that modeling the flow inside the timber stacks was necessary for a more realistic flow field results. The simplified model without the flow through the stacks resulted on a 14% lower drag coefficient value for the 5 degree yaw angle condition. It was shown that this difference was caused by the separation on the leeward side of the cabin, which was removed in the simplified model. It was demostrated that the separation on the realistic model was influence by the flow going upstream inside the first stack, and hence the simplified model was discarded for further studies since the results were not realistic enough.

From the results of the baseline model it was seen that the areas of the trailer which contributed more to the total drag were the gap (especially the front face of the second stack), the wheels, the bunks and the stakes. Hence, the different aerodynamic concepts were developed to affect the flow on those regions; gap, underbody and underload; in order to reduce the original 0.891 value of the drag coefficient on the baseline model.

Ten different aerodynamic concepts were explained on Sec. 4.2. The best performance was given by the gap spoiler, implemented together with the side-skirts, with a drag reduction of 31.6% with respect to the baseline and a 26.6% over the model with the side-skirts. This large effect on the total drag came from the reduction of the high pressure region on the gap and by keeping the flow attached on the leeward side of the cabin, which significantly reduced the wake on that side. Other good performance of aerodynamic concepts were found on the increased height side-skirts which, by affecting the flow on the underbody and also under the load and between the bunks, reached a drag reduction of 23.1% with respect to the baseline model. It is also worth noting the reduction of the wake on the back of the truck achieved by adding a boat-tail as a prolongation of the lateral cover, obtaining a drag reduction of 19.2% together with the side-skirts.

Analyzing the performance of the aerodynamic concepts individually it was decided to created two combinations by mixing the concepts with better results in each of the important flow field regions; that is, high skirts, gap spoiler, gap fairing and boat-tail. Since the gap spoiler and the gap fairing, aimed for drag reduction on the same region, and the spoiler performed better individually, a combination without the gap fairing was also tested.

Both combinations showed a good performance, achieving drag reduction higher than a 40% for the 5 degrees yaw angle case. However, the combination without

the fairing (Comb. 2) gave the best result (47.6%) since the flow on the right edge of the cab remained attached for this case, whereas separation was found when the gap fairing was added to the model. A sweep angle run on Comb. 2 showed that the effectiveness of these aerodynamic concepts combinations was reduced for the larger yaw angles where the separation on the cab is more influenced by the crosswind than by the flow modifications on the gap region.

Finally, from the comparison of different loading configurations it was concluded that incresing the height of the first stack did barely affect the drag value since, until the height limits of regulations, it is still inside the wake generated by the cab deflector. However, due to the great influence of the gap region on the total drag of the truck, changes of height on the second stack revealed a great importance on the total drag. In this case having a second stack lower than the first clearly reduced the drag since most of the flow goes directly on top of the second stack, reducing the high pressure on its front face. It was also noticed that having different height after the gap deteriorate the aerodynamic performance, since a separation wake appeared on the small gap between second and third stacks.

Regarding the CFD methodology study on the solver speed, it was shown that it is possible to increase the convergence speed towards a steady state solution by using the URANS model and tuning the solver control parameters. The major influence on the speed and level of convergence was given by increasing the implicit under relaxation factor on the turbulence equations, k and ε in this case, together with high Courant numbers on the Pressure Based Coupled solver; values of 0.98 and 1e6 respectively led to the best results on the 3D GTS model studied on this report. Using a larger time step size on the first iterations of the solution also proved to be an effective approach to increase the solver speed, it must be taken into account that the smaller time step size used during the solution should not be close to the characteristic time of the problem, in this case a time scale factor of 2.5 over the characteristic time gave the best results, when used as the smallest size after initiating the solution with a factor of 5.

This URANS approach seemed to be really sensitivity to the geometry and the quality of the mesh, especially if separations regions are to be found on the flow field.

6 Perspectives

This thesis was done in collaboration with the ETTaero2 project; the aim of the research is to reduce the fuel consumption and CO2 emissions generated by the trucks used on the timber transportation by improving their aerodynamic performance and therefore reduce the drag.

The studies carried out during this project are focused on the particular configuration of a fully loaded timber truck; the results have shown the possibility to reduce the drag up to a 50% when several aerodynamic concepts acting on different regions are combined together. This results will definitely help to achieve the objective of the project, allowing a more energy efficient way of timber transport.

Nevertheless, it must be considered that these vehicles will travel empty half of the time, hence the aerodynamics developments that have proved a good performance on the studies done on this report, must also be tested on the unloaded configuration in order to see if there is an overall performance improvement, even though the drag can be increased during the unloaded part of the trip. The same analysis should also be done in the fully loaded truck with the aerodynamics concepts that improved unloaded model.

The conclusion drawn on this report, together with further work done on the ETTaero2 project, could lead to a more sustainable way for timber transportation and at the same time reduce the cost of it due to the reduction of the fuel consumption and, since larger vehicles could be used, the fewer number of trucks needed to transport the same amount of load.

Regarding the methodology development study on the simulation speed, this could have a great impact on the CFD work flow in future research projects; decreasing the time needed for each simulation would reduce the required resources and therefore the cost; or it will be possible to run more simulations in the same time increasing the amount of studies and tests that can be carried out during a research project.

7 Future work

For further work on aerodynamic drag reduction on a fully loaded timber truck several studies can be done as a continuation or improvement of what has been shown on this report.

For a more realistic modeling of the timber stacks, a non-symmetric more random distribution of the logs in each stack could be studied. Furthermore, logs of different lengths inside the same stack could also influence the flow field. Regarding the simplification of each log, a further study could consist on using non-cylindrical logs for a more realistic approach, and also consider the roughness of the wood surface, which could influence the flow field in the near wall region of the logs; this could be done adding a boundary condition on the logs walls (not possible in this report due to the turbulence model used) or by creating a fictitious roughness by adding small irregularities along the logs external surfaces.

Regarding the aerodynamic results on the baseline and their improvement with the aerodynamics concepts, it was seen that the gap spoiler and the side-skirts with increased height performed well, also together, reducing the drag in the regions of greater contribution to the total drag. For a further improvement and optimization of these two concepts could be studied, that is for example finding the optimal length or angle for the spoiler or introduce some modifications in the skirts in the gap region, where improvements on the underbody flow could still be possible.

Another important finding of the aerodynamic study was the high sensitivity to separation on the leeward side of the cabin, this could also be study in a further work in order to assess how much of the drag reduction obtained with some of the concepts was really gained on the desired region and no by influencing the flow upstream. A more refined mesh or a change of geometry, larger radius, on the edges of the cabin could also be interesting to see if that behavior of the separation is realistic or induced somehow by the CFD simulations.

There is not a lot of data on loaded timber trucks currently; hence, experimental studies on the baseline and some aerodynamics concepts with good performance could be useful as a validation of the results presented on this report.

Finally, from the simulation speed methodology development, further work would be to apply some of the best performing settings found on this report on the full scale timber truck model.

References

[1] Ekman P, Gårdhagen R, Virdung T, Karlsson M. Aerodynamic Drag Reduction - from Conceptual Design on a Simplified Generic Model to Full-Scale Road Tests. SAE International Journal of Commercial Vehicles. 2015 apr;.

[2] Hucho WH. Aerodynamics of Road Vehicles: From Fluid Mechanics to Vehicle Engineering, W. SAE International, Warrendale, PA. 1998;177.

[3] Garner GJ. Wind tunnel tests on devices for reducing the aerodynamic drag of logging trucks. Technical Report Forest Engineering Research Institute of Canada (Canada) no TR-27. 1978;.

[4] Ekman P, Gardhagen R, Virdung T, Karlsson M. Aerodynamic Drag Reduction of a Light Truck - from Conceptual Design to Full Scale Road Tests. SAE International Journal of Commercial Vehicles. 2016 apr;.

[5] Ekman P, Gardhagen R, Virdung T, Karlsson M. Aerodynamics of an Unloaded Timber Truck - A CFD Investigation. SAE International Journal of Commercial Vehicles. 2016 sep;9(2):217–223.

[6] Karlsson M, Gårdhagen R, Ekman P, Söderblom D, Löfroth C. Aerodynamics of Timber Trucks - a Wind Tunnel Investigation. SAE International Journal of Commercial Vehicles. 2015 apr;.

[7] Allan J. Aerodynamic drag and pressure measurements on a simplified tractor-trailer model. Journal of Wind Engineering and Industrial Aerodynamics. 1981;9(1-2):125–136.

[8] Bertin JJ, Cummings R. Aerodynamics for Engineers. Prentice Hall, NJ; 2002.

[9] Theodore L Bergman FPIDPD Adrienne S Lavine. Fundamentals of heat and mass transfer; 2011.

[10] Wood R. Reynolds Number Impact on Commercial Vehicle Aerodynamics and Performance. SAE International Journal of Commercial Vehicles. 2015;8(2015-01-2859):590–667.

[11] Patten J, McAuliffe B, Mayda W, Tanguay B. Review of aerodynamic drag reduction devices for heavy trucks and buses. National Research Council Canada NRC Technical Report CSTT-HVC-TR. 2012;205:3.

[12] Windsor S. Real World Drag Coefficient - Is It Wind Average Drag? Jaguar Land Rover. 2014;.

[13] Davidson L. Fluid mechanics, turbulent flow and turbulence modeling. Div of Fluid Dynamics, Dep of Applied Mechanics, Chalmers University of Technology, Göteborg, Sweden. 2017;.

[14] Launder BE, Spalding DB. Lectures in Mathematical Models of Turbulence. Academic Press, London, England. 1972;.

[15] Shih TH, Liou WW, Shabbir A, Yang Z, Zhu J. A new k-e eddy viscosity model for high reynolds number turbulent flows. Computers & Fluids. 1995;24(3):227–238.

[16] ANSYS. Fluent Theory Guide. 2016;.

[17] ANSYS. Fluent User Guide. 2016;.

[18] Östh J, Krajnovic S. The flow around a simplified tractor-trailer model studied by large eddy simulation. Journal of Wind Engineering and Industrial Aerodynamics. 2012;102:36 – 47. Available from: http://www.sciencedirect.com/science/article/pii/S0167610511002522.

[19] Ekman P. LiU CFD Methodology for Road and Vehicle Aerodynamics and Version. 2017;.

[20] ANSYS Documentation, Fluent Meshing User's Guide; 2017.

[21] Storms BL. An Experimental Study of the Ground Transportation System (GTS) Model in the NASA Ames 7- by 10-Ft Wind Tunnel. National Aeronautics and Space Administration Ames Research Center. 2001;.

[22] Cooper KR. The Effect of Front-Edge Rounding and Rear-Edge Shaping on the Aerodynamic Drag of Bluff Vehicles in Ground Proximity. 1985 feb;.

[23] Wade A. Improving Convergence Series: Robustness on Poor Quality Meshes in Fluent. 2015;.

A Appendix

A URANS approach procedure

This Appendix describes the general procedure followed during the method development study on the simulation speed. For this an example case on the GTS model is shown, first the parameters needed for the solver settings and then a commented solver script where the different solver settings can be seen.

A.1 Model and flow parameters.

Fig. A.1 shows the geometry of the GTS model with the two parameters needed to obtain the time step size for the URANS simulations; in this case the height of the model (b) is used as the characteristic length (l_c) of the problem.

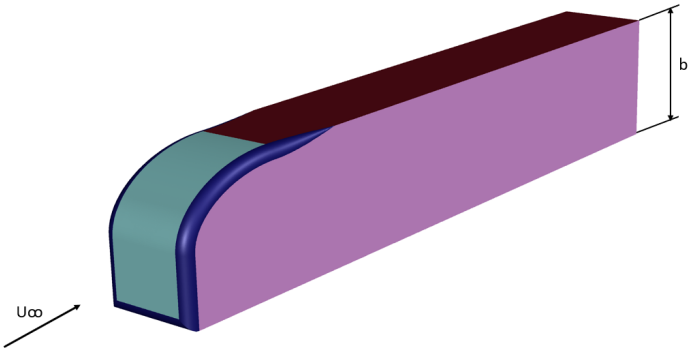

Figure A.1: Ground Transportation System (GTS) model geometry.

The time step size is calculated as a function of the characteristic time of the problem, equation (A.1), using a time scale factor (α_t), equation (A.2).

$$t_c = \frac{l_c}{u_\infty} \tag{A.1}$$

$$\Delta_t = \alpha_t \, t_c \tag{A.2}$$

A.2 Solver script

Listing 1: Example of solver script used on the GTS model simulations.

```
;;-----------------------------------------------------------------------
(define file_name "GTS_7M") ;Name of mesh file and for output files
;; FLUID AND MODEL PROPERTIES
(define X_VELOCITY 29.21469388)
(define Z_VELOCITY 0) ; 0 m/s for no crosswind conditions
(define FRONT_AREA 1.392)
;;-----------------------------------------------------------------------
;; READ MESH
(ti-menu-load-string (format #f "/file/read-case ~a \n" (string-append
    file_name "-vol.msh.gz")))
;;-----------------------------------------------------------------------
;;-----------------------------------------------------------------------
;; SCALE GRID TO METERS
(ti-menu-load-string (format #f "/mesh/scale 0.001 0.001 0.001 \n"))
;;-----------------------------------------------------------------------
;; NUMERICAL SETTIGNS
;; Turbulence model
(ti-menu-load-string (format #f "/define/models/viscous/ke-realizable?
    yes \n"))
(ti-menu-load-string (format #f "/define/models/viscous/near-wall-
    treatment/enhanced-wall-treatment? yes \n"))
;; Solver settings
;; p-v-coupling = 24 = coupled, discretization 1 = 2nd Upwind, Pressure
    10 = Std
(ti-menu-load-string (format #f "/solve/set/p-v-coupling 24 \n")) ;;
    Pressure Based Coupled Solver
(ti-menu-load-string (format #f "/solve/set/p-v-controls 20 .35 .35 \n"))
     ;Pressure Based Coupled Solver controls: 1)Courant number, 2)
    Explicit under-relaxation momentum eq 3) Explicit under-relaxation
    pressure eq.
(ti-menu-load-string (format #f "/solve/set/gradient-scheme yes \n")) ;;
    Green Gauss Node Base Gradient Scheme
(ti-menu-load-string (format #f "/solve/set/discretization-scheme k 0 \n
    ")) ;; 1st order Upwind
(ti-menu-load-string (format #f "/solve/set/discretization-scheme epsilon
     0 \n")) ;; 1st order Upwind
(ti-menu-load-string (format #f "/solve/set/discretization-scheme
    pressure 10 \n")) ;; Std pressure
(ti-menu-load-string (format #f "/solve/set/discretization-scheme mom 1 \
    n")) ;; 2nd order Upwind
(ti-menu-load-string (format #f "/solve/set/high-order-term-relaxation/
    enable yes \n"))
;;-----------------------------------------------------------------------
;; REFERENCE VALUES
(ti-menu-load-string (format #f "/report/reference-values/velocity
    X_VELOCITY \n"))
(ti-menu-load-string (format #f "/report/reference-values/area FRONT_AREA
     \n"))
;;-----------------------------------------------------------------------
;; CONVERGENCE CRITERIA
(ti-menu-load-string (format #f "/solve/monitors/residual/conv-criteria
    0.0001 0.0001 0.0001 0.0001 0.0001 0.0001 \n"))
(ti-menu-load-string (format #f "/solve/monitors/residual/check-
    convergence no no no no no no \n"))
(ti-menu-load-string (format #f "/solve/monitors/residual/plot no \n"))
;;-----------------------------------------------------------------------
;; MONITORS
(ti-menu-load-string (format #f "/solve/monitors/force/set-drag-monitor
    cd yes *gts* () no yes ~a no yes 1 0 0 \n" (string-append file_name "
    _Dt5_2-5_ER098_UR098_cfl1e6_cd")))
```

```
41 (ti-menu-load-string (format #f "/solve/monitors/force/set-drag-monitor
       cs yes *gts* () no yes ~a no yes 0 0 1 \n" (string-append file_name "
       _Dt5_2-5_ER098_UR098_cfl1e6_cs")))
42 (ti-menu-load-string (format #f "/solve/monitors/force/set-drag-monitor
       cl yes *gts* () no yes ~a no yes 0 1 0 \n" (string-append file_name "
       _Dt5_2-5_ER098_UR098_cfl1e6_cl")))
43 ; cd_residual monitor
44 (ti-menu-load-string (format #f "/solve/convergence-conditions/conv-
       reports/add cd_res report-defs cd print yes stop-criterion 1e-10\n" )
       )
45 ;;-------------------------------------------------------------------------
46 ;; GENERAL BOUNDARY CONDITIONS
47 (ti-menu-load-string (format #f "/define/boundary-conditions zone-type
       inlet velocity-inlet \n"))
48 (ti-menu-load-string (format #f "/define/boundary-conditions zone-type
       outlet pressure-outlet \n"))
49 (ti-menu-load-string (format #f "/define/boundary-conditions zone-type
       top symmetry \n"))
50 (ti-menu-load-string (format #f "/define/boundary-conditions zone-type
       left-side symmetry \n"))
51 (ti-menu-load-string (format #f "/define/boundary-conditions zone-type
       right-side symmetry \n"))
52 ;; INLET BOUNDARY CONDITION
53 (ti-menu-load-string (format #f "/define/boundary-conditions/velocity-
       inlet inlet no yes yes no 0 yes no X_VELOCITY no 0 no Z_VELOCITY no
       no yes 0.1 50 \n"))
54 ;; GROUND BOUNDARY CONDITION
55 (ti-menu-load-string (format #f "/define/boundary-conditions/wall ground
       yes motion-bc-moving no yes no no X_VELOCITY 1 0 0 no \n"))
56 ;;-------------------------------------------------------------------------
57 ; INITIALIZATION
58 (ti-menu-load-string (format #f "/solve/initialize initialize-flow \n"))
       ; Standard initialization with 0m/s
59 ;;-------------------------------------------------------------------------
60 ;;-------------------------------------------------------------------------
61 /define/custom-field-functions/define "total-pressure-coefficient" "
       total_pressure/(0.5*1.225*29.21469388^2)"
62 ;;-------------------------------------------------------------------------
63 ;; SOLVER RANS
64 (ti-menu-load-string (format #f "/solve/set/p-v-controls 20 .35 .35 \n"))
        ;Pressure Based Coupled Solver controls: 1)Courant number, 2)
       Explicit under-relaxation momentum eq 3) Explicit under-relaxation
       pressure eq.
65 (ti-menu-load-string (format #f "/solve/iterate 20 \n")) ; 20 iterations
       with RANS model to initialize the flow field with reasonable values
66 ;;-------------------------------------------------------------------------
67 ;;-------------------------------------------------------------------------
68 ;; URANS SOLVER
69 /define/models/unsteady-1st-order? yes ; Change to transient solver:
       URANS model, temporal discretization: 1st order
70 ;;-------------------------------------------------------------------------
71 ;; COUPLED SETTINGS
72 (ti-menu-load-string (format #f "/solve/set/p-v-controls 1e6 .98 .98 \n")
       ) ;Pressure Based Coupled Solver controls: 1)Courant number, 2)
       Explicit under-relaxation momentum eq 3) Explicit under-relaxation
       pressure eq.
73 (ti-menu-load-string (format #f "/solve/set/under-relaxation k 0.98 \n"))
        ; Implicit under-relaxation factor for the k-equation
74 (ti-menu-load-string (format #f "/solve/set/under-relaxation epsilon 0.98
        \n")) ; Implicit under-relaxation factor for the epsilon-equation
75 ;;-------------------------------------------------------------------------
76 (ti-menu-load-string (format #f "/solve/set/time-step 0.24 \n")) ; Time
       step size, in this case 5 times the characteristic time
77 (ti-menu-load-string (format #f "/solve/dual-time-iterate 25 2 \n")) ;
       Time steps simulated and iterations inside each time step, total 50
       iterations
```

```
78 (ti-menu-load-string (format #f "/solve/set/time-step 0.12 \n")) ; Time
       step size, in this case 2.5 times the characteristic time
79 (ti-menu-load-string (format #f "/solve/dual-time-iterate 200 2 \n")) ;
       Time steps simulated and iterations inside each time step, total 400
       iterations
80 ;;-------------------------------------------------------------------------
81 ;;-------------------------------------------------------------------------
82 ;; FILE EXPORT
83 (ti-menu-load-string (format #f "/file/write-case-data ~a \n" (string-
       append file_name "_Dt5_2-5_ER098_UR098_cfl1e6.cas.gz")))
84 (ti-menu-load-string (format #f "/file/export/ensight-gold ~a pressure-
       coefficient total-pressure-coefficient x-wall-shear y-wall-shear z-
       wall-shear viscosity-ratio () yes (*) () no \n" (string-append
       file_name "-Dt5_2-5_ER098_UR098_cfl1e6")))
85 ;;-------------------------------------------------------------------------
86 ;;-------------------------------------------------------------------------
87 (ti-menu-load-string (format #f "/parallel/timer/usage \n"))
88 yes
89 yes
90 yes
91 exit
92 yes
93 yes
94 yes
```